Study of the Photon Structure via Dijet Production at HERA

by

Dorian Kçira

Study of the Photon Structure via Dijet Production at HERA

Dissertation
zur Erlangung des Doktorgrades
des Fachbereiches Physik
der Universität Hamburg

vorgelegt von

Dorian Kçira

aus Shkodra

Hamburg
2001

Gutachter der Dissertation: Prof. Dr. R. Klanner
Prof. Dr. E. Lohrmann

Gutachter der Disputation: Prof. Dr. E. Lohrmann
Prof. Dr. B. Naroska

Datum der Disputation: 12.10.2001

Dekan des
Fachbereichs Physik und
Vorsitzender des
Promotionsausschusses: Prof. Dr. F.-W. Büßer

Abstract

The dependence of the virtual photon (γ^*) structure on the photon virtuality, Q^2, is studied in the kinematic range $0.1 < Q^2 < 10^4$ GeV^2 and $0.2 < y < 0.55$ by measuring the reaction $e^+p \to e^+ + jet + jet + X$ with the ZEUS detector at HERA using an integrated luminosity of 38.2 pb^{-1}. Events having two jets with transverse energies $E_T^{*\,jet1} > 7.5$ GeV and $E_T^{*\,jet2} > 6.5$ GeV in the final state have been selected using the longitudinally invariant k_T algorithm in the photon-proton hadronic center of mass frame of reference. The dijet cross section has been measured as a function of the fractional momentum of the photon participating in the hard scattering process, x_γ^{OBS}, and Q^2. The ratio of the dijet cross section with $x_\gamma^{OBS} < 0.75$ to that with $x_\gamma^{OBS} > 0.75$ decreases as Q^2 increases. The data are compared with the predictions of LO pQCD using different parton distribution functions of the photon. The measurements can be interpreted in terms of a resolved photon component that falls with increasing Q^2.

Zusammenfassung

Die Abhängigkeit der Struktur des virtuellen Photons (γ^*) von der Photonenvirtualität, Q^2, wurde in dem kinematischen Bereich $0.1 < Q^2 < 10^4$ GeV^2 und $0.2 < y < 0.55$ untersucht. Hierzu wurde die Reaktion $e^+p \to e^+ + jet + jet + X$ am ZEUS Detektor bei HERA, basierend auf einer integrierten Luminosität von 38.2 pb^{-1}, gemessen. Mit Hilfe des longitudinal invarianten k_T Algorithmusses wurden Ereignisse mit zwei Jets im Endzustand mit transversalen Energien von $E_T^{*\,jet1} > 7.5$ GeV und $E_T^{*\,jet2} > 6.5$ GeV im Referenzsystem des Photon-Proton Schwerpunktsystems ausgewählt. Der Zwei-Jet Wirkungsquerschnitt wurde als Funktion des Impulsanteils des Photons x_γ^{OBS}, das am harten Subprozess teilnimmt, und Q^2 gemessen. Das Verhältniss des Zwei-Jet Wirkungsquerschnittes mit $x_\gamma^{OBS} < 0.75$ zu dem mit $x_\gamma^{OBS} > 0.75$ verringert sich mit zunehmenden Q^2. Die Daten wurden verglichen mit Vorhersagen führender Ordnung der pQCD für verschiedene Partonendichtefunktionen des Photons. Die Messung kann durch ein aufgelöstes Photon interpretiert werden, dessen Anteil sich mit steigendem Q^2 verringert.

Contents

1 Introduction **16**
1.1 The Standard Model . . . 16
1.2 Deep Inelastic Scattering . . . 19
1.2.1 Kinematic Variables for Lepton Nucleon Scattering . . . 19
1.2.2 Structure Functions . . . 21
1.3 Quark Parton Model . . . 22
1.4 QCD . . . 24
1.4.1 Factorization . . . 24
1.4.2 QCD evolution equations . . . 25
1.5 Photoproduction . . . 29

2 Introduction to Photon Structure **30**
2.1 Photon Structure . . . 30
2.1.1 Hadronic Photon Structure . . . 30
2.2 Photon Structure in e^+e^- experiments - F_2^γ . . . 33
2.3 Parton Distribution Functions of the Photon . . . 39
2.3.1 The evolution of the pdfs of the photon . . . 39
2.3.2 Parametrizations of the parton distribution functions for real photons. . . . 42
2.3.3 Parametrizations of the parton distribution functions for virtual photons. . . . 42
2.4 Photon Structure at HERA . . . 44
2.4.1 Dijet Production in γP Interactions . . . 44
2.4.2 The two Scale Problem . . . 47
2.4.3 Dijet Cross Sections - The Flux of Real and Virtual Photons . . . 49
2.5 Electromagnetic Photon Structure . . . 50

3 HERA and ZEUS **52**

3.1 The Hadron Electron Ring Accelerator . . . 52
3.2 The General Purpose ZEUS Detector . . . 54
3.2.1 The Central Tracking Detector . . . 56
3.2.2 The Uranium-Scintillator Calorimeter . . . 57
3.3 Presampler . . . 59
3.4 Small Angle Rear Tracking Detector . . . 60
3.5 The Luminosity Monitor . . . 62
3.6 The Beam Pipe Calorimeter . . . 63
3.7 The ZEUS Trigger . . . 65

4 Jets **69**
4.1 Jets in QCD . . . 69
4.2 Jet Finders . . . 69
4.2.1 The Snowmass Convention . . . 70
4.2.2 Cone Algorithm . . . 71
4.2.3 Clustering Algorithms . . . 72
4.3 Jets at HERA . . . 73
4.3.1 Photon-Proton Hadronic Center of Mass Frame . . . 73
4.3.2 Effect of the boost on the jets . . . 74

5 Data Selection **76**
5.1 Online Event Selection - Trigger Logic . . . 76
5.1.1 First Level Trigger . . . 76
5.1.2 Second Level Trigger . . . 77
5.1.3 Third Level Trigger . . . 78
5.2 Offline Event Selection . . . 79
5.2.1 General Selection . . . 79
5.2.2 Photoproduction . . . 82
5.2.3 Intermediate Q^2 . . . 84
5.2.4 DIS . . . 86

6 Event and Detector Simulation **88**
6.1 Monte Carlo Models . . . 89
6.1.1 Herwig . . . 89
6.1.2 Pythia . . . 90
6.2 Multiple Parton Interactions . . . 91

6.2.1 Hadron Level Theoretical Predictions - the HzTool Package . . 92
6.3 Filters applied to Simulated Events . . . 92
6.3.1 The Jet Filter . . . 92
6.3.2 The BPC Filter . . . 93
6.4 Mixing Direct and Resolved Processes . . . 94
6.5 Description of Data by the Simulation . . . 95

7 Analysis Method **104**
7.1 Resolutions . . . 104
7.2 Data Correction . . . 105
7.3 Systematic Studies . . . 111
7.4 Photoproduction Analysis . . . 114

8 Results / Discussion **121**

9 Conclusions **125**

10 Acknowledgments **126**

A Jet Energy Correction **127**

B Triple Differential Cross Sections **134**
B.1 Conclusions . . . 135

List of Figures

1.1 Diagram for single photon exchange in ep scattering. The four momenta are given in brackets. . . . 20

1.2 Factorization: separation of the short-ranged and long-ranged physics. The parton distributions in the hadrons are not perturbatively calculable (long-ranged physics). The hard cross section $\sigma_{ij}(Q^2)$ is perturbatively calculable (short-ranged physics). . . . 26

1.3 Behaviour of the structure function F_2 with increasing scale. The two top pictures show the case of QPM. The two bottom pictures show the changes when QCD effects are included (from: [Ab98]). . . . 27

1.4 Scaling violations - the structure function F_2 versus the scale Q^2 for different values of x. The structure function F_2 is not independent of Q^2. The F_2 measurements for different x have been scaled by constant factors in order for all of them to fit on the same plot. . . . 28

2.1 A photon can be bare (pointlike) or fluctuate into a $q\bar{q}$ pair. Low virtuality fluctuations are give rise to vector meson states. From top to bottom, the three components of the photon: bare, anomalous, and VMD component. . . . 31

2.2 Measurement of photon structure in e^+e^- experiments. The $F_{2,\mathrm{eff}}^{\gamma}$ versus x. . . . 34

2.3 Kinematics of two-photon induced processes in e^+e^- collisions. k/k' and l/l' are the four-momenta of the incoming/outgoing electrons (positrons). The four momenta are written in brackets for all the components. The photon with the smallest virtuality (P^2) is the target photon while the one with the highest virtuality Q^2 is the "probe photon". . . . 35

2.4 F_2^{γ} measurements at e^+e^- experiments in different bins of x_{γ} and Q^2. Note: the variable x on the plots is denoted in the text of the thesis by x_{γ}. The Q^2 increases from left to right and from top to bottom. The vertical error bars represent the statistical + systematic errors added in quadrature. The horizontal error bars (!) represent the statistical errors only. The mean Q^2 in GeV^2 of each bin is shown also after the experiment mean. . . . 37

2.5 F_2^{γ} evolution with Q^2. The $\ln(Q^2)$ dependence over a large range of Q^2 values can be seen. Note: the variable x on the plots is denoted in the text of the thesis by x_{γ}. . . . 38

2.6 LO and NLO parametrizations of the real photon pdfs [Vo97]. In the above two plots are given the (up) quark densities. The two plots below show parametrizations of the gluon densities . . . 41

2.7 Different parametrizations of the virtual photon pfd's: quarks (left plot) and gluons (right plot) at $Q^2 = 10$ GeV^2 for two different values of P^2: $P^2 = 0.2$ GeV^2 and $P^2 = 1.$ GeV^2 . . . 43

2.8 Two example leading order diagrams for direct (left) and resolved (right) photoproduction at HERA. Note the presence of the photon remnant in the case of resolved interactions. . . . 44

2.9 LO graphs for direct and resolved photon interactions. The two graphs of the first (top) row: QCD Compton scattering and Boson-Gluon Fusion are the two (LO) direct photon interactions. The other graphs represent the 6 possible (LO) resolved photon interactions. . . . 46

2.10 The $x_{\gamma}^{\mathrm{OBS}}$ variable for dijet photoproduction events at HERA. The solid line is the Herwig5.9 simulation and the shaded area is the direct-only part from the simulation. The direct part is concentrated at higher $x_{\gamma}^{\mathrm{OBS}}$ and the resolved part at lower $x_{\gamma}^{\mathrm{OBS}}$. One can see that a rather clean separation of the resolved and direct events can be done by a cut on $x_{\gamma}^{\mathrm{OBS}} = 0.75$. . . . 47

2.11 Photon structure seen in the phase space of the two scales at HERA. In the picture also the line is drawn where $E_T^2 =$ photon virtuality. In reality the transitions between the different regions are smooth and there are no sharp limits between them. . . . 48

2.12 Summary of $F_2^{\gamma(\mathrm{QED})}$ measurements. The errors plotted are only statistical. The structure function $F_2^{\gamma(\mathrm{QED})}$ is plotted versus $x_{\gamma}^{\mathrm{OBS}}$ in different bins of the photon virtuality (given in brackets in each region). [Ni00] . . . 51

3.1 Aerial view of DESY and surroundings together with the two largest accelerators HERA and PETRA. . . . 52

3.2 The HERA accelerator and its pre-accelerator complex. . . . 53

3.3 CAD drawing of the ZEUS detector in the Y-Z plane. The arrow points to the position of the BPC and BPT inside ZEUS. . . . 54

3.4 CAD drawing of the ZEUS detector in the X-Y plane (perpendicular to the beams). . . . 55

3.5 Integrated luminosity delivered by HERA in the different running periods (left plot) and the one taken with the ZEUS detector (right plot) that is used for physics analysis. . . . 56

3.6 Schematic diagram of one octant of the CTD with the 9 superlayers. . 57

3.7 Side view of the ZEUS calorimeter with the uranium calorimeter divided into sections, modules, towers, and cells. . . . 58

3.8 View of a module of the FCAL with the EMC and HAC sections divided into cells. 59

3.9 RCAL front view. The shaded part is the area covered by the presampler. 60

3.10 Layout of the Small angle Rear Tracking Detector (SRTD). Orientation and numbering scheme of the strips. In 1995 the RCAL and SRTD modules above and below the beampipe hole have been moved closer together. The quadrants 2 and 4 are only separated by 8 cm. 61

3.11 Positioning of the SRTD inside the ZEUS detector in the zy plane. The distances are not to scale. The SRTD covers the gap between the Rear Tracking Detector (RTD) and the beam pipe. 62

3.12 The ZEUS luminosity system and different magnets in the negative Z direction. The bending magnets are marked with B and the quadrupole magnets with Q. 63

3.13 The BPC modules and ther location with respect to the beam pipe. The position of the modified beam pipe window is also shown. 64

3.14 CAD drawing of the BPC modules with details of their construction. . 65

3.15 The ZEUS trigger and data acquisition system. 66

3.16 Trigger rates of FLT, SLT, and TLT as a function of luminosity and data taking period for the years 1993-1997. 67

4.1 Schematic diagram of a typical analysis using jets [Se95]. In the upper line the partons are produced from the hard scattering process and then they radiate other partons (parton shower). Colour singlet states (hadrons) are produced through the process of hadronization. The hadrons deposit energy in the detector. At each one of these stages on can do the jet finding. From the measured data in the detector one can correct backwards in principle down to the parton level. 71

4.2 The pseudorapidity of the jets in the lab ($\eta_{\rm lab}$) versus the pseudorapidity of the jets in the photon-proton hadronic center of mass frame ($\eta_{\rm hcm}$) is plotted. In the upper plot left the scattered electron energy is larger than 5 GeV, while in the other plots different intervals of the scattered electron energy are chosen. The straight lines are drawn to help see the boost and the difference in boost between the different plots. The photon virtuality region for this plot is $0.1 < Q^2 < 0.55$ GeV^2. In this region the effect of the boost on the transverse energy of the jets is negligible. 75

5.1 The available phase space for the two highest transverse energy jets. Adding a difference δ between them helps to avoid the region of phase space where the NLO theoretical calculations are infrared sensitive. (hep-ph/9911221) 82

5.2 The Q^2 distribution of the simulation events for the case of untagged sample. The requirement applied is $Q^2 < 1$ GeV^2. But, as one can see from the plot, most of the events are concentrated at very low values of the photon virtuality: $Q^2 \ll 1$ GeV^2. 83

5.3 BPC fiducial volume. The BPC is schematically shown with the vertical and horizontal strips and the fiducial volume is drawn. BPC data events passing the trigger selection and the jet cuts are shown as dots. 85

6.1 Schematic representation of multiple parton scattering in the case of γp collisions. More than one had partonic scattering occurs in a single collision. 91

6.2 The BPC filter for simulated events at hadron level. In the $x - y$ plane the BPC surface is shown and the electron position extrapolated at this surface for Monte Carlo events which pass the filter is plotted as a scatter plot. The φ angle of all the events is contained between the lines passing through the $(0, 0)$ point and through (3.4 cm, -6.7 cm) and (3.4 cm, 6.8 cm). The angle between the lines is $\Delta\varphi_e = 2.20835$ rad. The geometrical reduction factor is: $2\pi/\Delta\varphi = 2.84519$. 93

6.3 $x_\gamma^{\rm OBS}$ - distributions for different Q^2 regions - intermediate Q^2 and DIS region. The points are the ZEUS data and the solid line is the Herwig5.9 Monte Carlo simulation with GRV as photon structure function parametrization. The shaded area is the Herwig direct events only. The $x_\gamma^{\rm OBS}$ reweighting is applied to the Monte Carlo. The description of the data by the Monte Carlo is generally good. 96

6.4 Distributions of physical quantities for the photoproduction region. The points are the ZEUS data and the solid line the Herwig5.9 Monte Carlo. The shaded area is the Herwig direct events only. The agreement is generally good. For more details see text. 98

6.5 Different distributions of important physical quantities used in the analysis. Comparison between the data (points) and the Herwig5.9 Monte Carlo simulation (solid line). The photon virtuality region is: $0.1 < Q^2 < 0.55$ GeV^2. 99

6.6 Comparison between data and MC for the photon virtuality region $1.5 < Q^2 < 4.5$ GeV^2. Distributions of the $y_{\rm JB}$, the jet quantities and the electron quantities. The points are the ZEUS data, the solid line the Herwig5.9 Monte Carlo. 100

6.7 Comparison between data and MC for the photon virtuality region $4.5 < Q^2 < 10.5$ GeV^2. Distributions of the $y_{\rm JB}$, the jet quantities and the electron quantities. The points are the ZEUS data, the solid line the Herwig5.9 Monte Carlo. 101

6.8 Comparison between data and MC for the photon virtuality region $10.5 < Q^2 < 49.$ GeV^2. Distributions of the y_{JB}, the jet quantities and the electron quantities. The points are the ZEUS data, the solid line the Herwig5.9 Monte Carlo. 102

6.9 Comparison between data and MC for the photon virtuality region $49. < Q^2 < 10^4$ GeV^2. Distributions of the y_{JB}, the jet quantities and the electron quantities. The points are the ZEUS data, the solid line the Herwig5.9 Monte Carlo. 103

7.1 Q^2 resolution in the different Q^2 bins. The resolution here is defined as $(Q^2(GEN) - Q^2(DET))/Q^2(DET)$, where GEN stays for generator level and DET for detector level. In the DIS bins ($Q^2 > 1.5$ GeV^2), the resolution gets better with increasing Q^2. The first bin has a better resolution because for that region of the photon virtuality the electron is detected in the Beam Pipe Calorimeter. 106

7.2 y resolution in the different Q^2 bins. Here the resolution is defined as the difference of $y(GEN)$ at the generator level with the y_{JB} at the detector level calculated with the Jacquet-Blondel method. 107

7.3 x_γ^{OBS} resolution in the different Q^2 bins. The resolution here is the difference of $x_\gamma^{OBS}(GEN)$ at the generator level with $x_\gamma^{OBS}(DET)$ at the detector level. 108

7.4 Correction factors C_i^{MC} versus x_γ^{OBS} for the different Q^2 regions. The plotted errors are statistical. The correction factors for the two lowest Q^2 regions (BPC and low DIS) are larger than the other ones. For the BPC this reflects its small geometrical acceptance. For the lowest DIS Q^2 region this is an effect of the box cut. 110

7.5 Correction factors on x_γ^{OBS} for Herwig (upper plot), Pythia (lower plot) for the region $0.1 < Q^2 < 0.55$. No dependence of the correction versus x_γ^{OBS} is seen. In the first bin of x_γ^{OBS} the correction factors are large but the number of events in this bins is small. 113

7.6 The ratio of the correction factors for Herwig and Pythia versus x_γ^{OBS} for $0.1 < Q^2 < 0.55$. The ratio shows no x_γ^{OBS} dependence and has a value of about 1.2. Therefore, the unceratinty coming from the hadronization corrections is evaluated to be 20%. 114

7.7 Systematic studies in the virtuality region: $0.1 < Q^2 < 0.55$ GeV^2. All uncertainties are shown in percent and a shaded band of $\pm 10\%$ is plotted to facilitate the visual evaluation of them. The upper left plot shows the correlated energy scale uncertainty. The other plots show the different uncorrelated uncertainties. Specific for this region is the uncertainty on the fiducial volume cut of the BPC detector. 115

7.8 Systematic studies in the virtuality region $1.5 < Q^2 < 4.5$ GeV^2. All uncertainties are shown in percent and a shaded band of $\pm 10\%$ is plotted to facilitate the visual evaluation of them. The box cut around the beam pipe on the position of the electron has a large uncorrelated systematic uncertainty at this lower Q^2. 116

7.9 Systematic studies in the virtuality region $4.5 < Q^2 < 10.5$ GeV^2. The ucertainty on the box cut becomes here small. The uncertainties on the y_{JB} and jet quantities cuts remain the main source of uncorrelated uncertainties. 117

7.10 Systematic studies in the virtuality region $10.5 < Q^2 < 49.0$ GeV^2. . . 118

7.11 Systematic studies in the virtuality region $4.0 < Q^2 < 10^4$ GeV^2. . . . 119

8.1 Dijet cross section in the γ^*-proton hadronic c.m. frame for different regions of photon virtuality. The points are the data with the inner bars representing the statistical errors and the outer ones the statistical and the systematic errors added in quadrature. The shaded band shows the correlated systematic errors. The solid line is the hadron level prediction from Herwig using the SaS1D pdfs for the photon normalized to the highest x_γ^{OBS} bin in the data. The broken line is the prediction using the Herwig LO direct part only. 123

8.2 Cross section ratio $R^{DATA} = \sigma(x_\gamma^{OBS} < 0.75)/\sigma(x_\gamma^{OBS} > 0.75)$ versus the photon virtuality. The points are the data with statistical errors represented from the inner error bars. The outer error bars represent the statistical and systematic errors added in quadrature. The solid line is the Herwig prediction using the SaS1D pdfs for the photon and the broken line is the prediction of Herwig using the GRV pdfs for the photon, while the inverted triangles connected by the dot-line show the prediction of Ariadne for the ratio. The data fall with increasing photon virtuality. The SaS1D prediction falls as well. The GRV prediction is flat as expected since it models real photons and lacks a photon suppresion with photon virtuality. The ratio of the data measurement with the SaS1D prediction is shown as an inset. This ratio R^{DATA}/R^{SaS} seems to be flat in Q^2. The SaS1D model appears to underestimate the resolved component by $\sim 30\%$. 124

A.1 Resolution plots in the laboratory frame: $\eta^{jet-had} - \eta^{jet-cal}$, $\phi^{jet-had} - \phi^{jet-cal}$, and $(E_T^{jet-had} - E_T^{jet-cal})/E_T^{jet-cal}$. No systematic shift is observed for the pseudorapidity and the azimuthal angle. A shift of about 20% is observed for the transverse energy of the jets. 128

A.2 Jet corrections in the laboratory frame. $E_T^{jet-had}/E_T^{jet-cal}$ vs. $E_T^{jet-cal}$ in different η^{jet} bins. Also the fit with the function $P1 + \exp(P2 + P3 * E_T^{jet-cal})$ and the values of the parameters are shown. 129

A.3 Jet corrections in the laboratory frame. $E_T^{jet-had}/E_T^{jet-cal}$ vs. $\phi^{jet-cal}$ (plot above) and $\eta^{jet-cal}$ (plot below) is shown. The correction is flat in $\phi^{jet-cal}$ as expected and shows a characteristic shape in $\eta^{jet-cal}$. This has to do with the distribution of the dead material in the detector as a function of the pseudorapidity (radial angle). 131

A.4 Resolution plots in the laboratory frame after applying the jet energy correction: $(E_T^{jet-had} - E_T^{jet-cal})/E_T^{jet-cal}$ For this plot, the analysis cuts are applied on the jets: $E_T^{jet1,2-had} \geq 7.5, 6.5$ GeV $-1. \leq \eta^{jet1,2-had} \leq 2.$ and same cuts on the calorimeter jets (here the corrections are applied on the calorimeter jet energy). 132

A.5 Jet corrections in the hadronic c.m. frame. $E_T^{*jet-had}/E_T^{*jet-cal}$ vs. $E_T^{*jet-cal}$ in different η^{*jet} bins. Also the fit with the function $P1 + \exp(P2 + P3 * E_T^{*jet-cal})$ and the values of the parameters are shown. 133

B.1 Triple differential cross section $d^3\sigma/(dx_\gamma^{OBS} dQ^2 d\overline{E}_T^2)$ as a function of x_γ^{OBS} for different regions in Q^2 and $\overline{E}_T^2$. The points represent the measured cross sections with statistical errors (inner error bars) and uncorrelated systematic errors added in quadrature to them (outer error bars). The shaded bands display the uncertainty in the plotted quantities due to that in the jet energy scale. The solid line is the Herwig MC using the SaS1D parametrization for the photon PDFs and the dashed line is the LO-direct part only from Herwig. 136

B.2 Comparison of the measured cross sections with the Herwig MC using the two resolved components from SaS1D: the perturbative (anomalous) component (upper dotted curve) and the non-perturbative (VDM) component (lower dotted curve). Herwig using the SaS1D total is also shown as a solid line. 137

B.3 Comparison of the measured cross sections with the Lepto MC (dashed line). Herwig using the SaS1D total is also shown as a solid line. Lepto is seen to act very similarly the Herwig using the LO-direct component only. 138

B.4 The ratio of cross sections $R = \sigma(x_\gamma^{OBS} < 0.75)/\sigma(x_\gamma^{OBS} > 0.75)$ as a function of Q^2 for different ranges in $\overline{E}_T^2$. The solid line is the Herwig MC using the SaS1D parametrization for the photon PDFs and the dotted horizontal line is the Herwig prediction using the GRV parametrization for the real photon PDFs. 139

Chapter 1

Introduction

1.1 The Standard Model

According to the Standard Model, the elementary constituents of matter are quarks and leptons. They are fermions, with spin $1/2$.

There are 6 (known) leptons and 6 quarks. The leptons are: electron (e), muon (μ), tau (τ), electron neutrino (ν_e), muon neutrino (ν_μ), tau neutrino (ν_τ). The quarks are: up quark (u), down quark (d), charme (c), strange quark (s), bottom quark (b), top quark (t). For each particle, there exists a corresponding anti-particle with the same mass but opposite sign charge, isospin, baryon and lepton quantum numbers (see table 1.1).

There are four known fundamental interactions/forces in nature. In quantum field theory these forces are mediated by integer spin gauge bosons. The four known interactions are:

1. the Electromagnetic Interaction
   The Electromagnetic Force is the interaction occurring between particles which carry *electrical charge*. The gauge boson that mediates the electromagnetic force is the photon γ. Photons are massless and electrically neutral (they do not carry electrical charge).

2. the Weak Interaction
   The Weak Force acts between fermions (spin $1/2$ particles) and is mediated via the $W^\pm$ and Z^0 gauge bosons. These gauge bosons are massive[1].

3. the Strong Interaction
   The Strong Force couples particles having *strong colour-charge*, or shortly *colour*. There exist three colours. In this case the gauge bosons are the *gluons*. Gluons themselves are massless but carry colour-charges and are subject to the strong interaction.

4. the Gravitational Interaction
   The Gravitational Force is the force which acts between particles with mass

[1] The W-bosons have a mass of 81 GeV and the Z^0 boson 91.2 GeV.

(m). In quantum theories of the gravity, the gravitational field is mediated by a spin two ($s = 2$) boson which is called *Graviton*.

This interaction is the weakest of the four interactions and is long-ranged. At the present energies used in High-Energy Physics, the gravitational force can be neglected.

The combination of the Electroweak Theory with QCD constitutes the *Standard Model*. In the context of this model the 12 elementary fermions (quarks and leptons) are classified in the Standard Model in three families (generations). The masses of the particles change between families but the way the particles interact remains the same (see also table 1.1).

	Families			electric charge	Forces str	em	weak	grav
Quarks	u	c	t	$2/3$	×	×	×	×
	d	s	b	$-1/3$	×	×	×	×
Leptons	ν_e	ν_μ	ν_τ	0	-	-	×	×
	e	μ	τ	-1	-	×	×	×

Masses of Quarks (MeV)					
d	u	s	c	b	t
< 100	< 100	~ 400	~ 1500	~ 5000	~ 174000

Table 1.1 - Generations of fermions in the Standard Model. The electrical charge of the particles is shown and the interaction they undergo. In the second table estimations of the masses of the quarks are given. The × in the first table mean that the particles are subject to the force and the — means tha the particles are not subject to it.

Quantum Electrodynamics (QED) is the theory of electromagnetic interactions. The results of QED can be calculated using perturbation theory since the electromagnetic coupling constant $\alpha \simeq 1/137$ is much smaller than unity. At larger distances the effective charges are less than the ones at smaller distances. This comes because of screening effects (charges emit and absorb virtual photons which, on their turn, fluctuate in electron-positron pairs - vacuum polarisation). For the present energy scales in HEP experiments α is small enough that the perturbative approach can be applied.

Strong interactions are described by Quantum Chromodynamics (QCD). The mediators of the strong interaction, the gluons, carry colour. Colour plays for the strong interaction the role of the charge in the electromagnetics interactions. In contrast to the electromagnetic interactions, the gluons, the field quanta of the strong interaction, carry colour and, therefore, interact themselves strongly. The (effective) coupling constant for the strong interactions α_s depends on the scale at which the process occurs. Calculation of results using perturbative methods in QCD is not always possible. In fact perturbative QCD (pQCD) cannot be always applied and its use depends also on the concrete experiment (process) for which the calculations

are made. Contrary to the electromagnetic coupling constant α, the strong coupling constant α_s decreases as the scale increases. Some aspects of QCD will be described in this chapter.

The electromagnetic and weak interactions are unified within the electroweak theory by Glashow, Salam and Weinberg [Gl61]. The QCD and the electroweak theory are gauge theories and can be derived from symmetry principles [Lo92]. For the strong interaction, the basic symmetry is $SU(3)$, which is connected to the three degrees of freedom given by the three colour-charges. The electroweak interaction is based on the $SU(2)xU(1)$ symmetry. $SU(2)$ is the non-abelian electroweak-isospin group. $U(1)$ is the Abelian hypercharge group[2].

Experimental evidence by a large number of high energy experiments has shown an overwhelming success of the Standard Model. Fundamental tests of its correctness have been made and precise determinations of its free parameters are done. In spite of these successes, there are open questions concerning the Standard Model.

Some of the problems and still unresolved questions are listed below:

- *Quark Confinement*, the fact that no free quarks are observed has not been demonstrated in a rigorous way from the Standard Model (in QCD).
- QCD does not predict the masses of quarks and leptons.
- The existence of exactly three families of quarks and leptons is not explained from the Standard Model.
- No combination of the General Theory of Relativity and the Quantum Mechanics exists yet. There is a large and unexplained difference between the scales of the Standard Model ($\sim$ 100 GeV) and the scale of Gravity, given by the Planck mass of 10^{19} GeV.
- The Standard Model also does not explain the fact that we observe more particles than antiparticles, although they must have been created in equal numbers.
- One of the main unresolved questions in the Standard Model is the existence of the Higgs Bosons. Its existence is related to the generation of elementary particle masses. Gauge Bosons and Fermions obtain their masses by interacting with the vacuum Higgs Field. Associated with this mechanism is the existence of massive scalar particles called Higgs bosons. A clear experimental observation of the Higgs bosons has not yet been made. The LEP experiments at CERN[3] have produced a number of collisions compatible with the production of Higgs particles with a mass of around 115 GeV. However these events were also compatible with other known processes [LE00], so the evidence was not conclusive.

[2] The hypercharge Y is connected to the isospin I_3 and the electrical charge Q by the relation: $Y = 2 \cdot (Q - I_3)$.

[3] CERN - **C**onseil **E**uropéen pour la **R**echerche **N**ucléaire - Switzerland.

- The Standard Model fails to account for the solar and atmospheric neutrino data which strongly indicate the need for neutrino conversions, as would arise from neutrino-mass-induced oscillations [Ne00].

1.2 Deep Inelastic Scattering

Many aspects of the Standard Model have an important experimental input from the Deep Inelastic Scattering (DIS) regime of high energy physics experiments. The first experimental evidence for the structure of the proton came from elastic scattering experiments performed at the High Energy Physics Laboratory at Stanford University in the early 1950s [Ho53].

In the following section the kinematics of ep scattering is described in detail.

1.2.1 Kinematic Variables for Lepton Nucleon Scattering

The scattering of positrons (electrons) off protons is described by the exchange of a gauge boson: γ^* or Z^0 in the case of neutral current interactions and $W^{\pm}$ in the case of charged current interactions. In this section the kinematic variables will be defined. The ep collision can be seen as a $\gamma^* p$ collision with the lepton emitting the photon. A Feynman diagram for the single photon exchange is depicted in figure 1.1.

The four momenta for the incoming positron and proton are:

$$\begin{aligned} k &= (E_e, 0, 0, -E_e) \\ p &= (E_p, 0, 0, E_p) \end{aligned}$$

where $E_e = 27.5$ GeV and $E_p = 820$ GeV are respectively the energy of the positron and that of the proton beam. The coordinate system is defined such that the incoming protons move in the positive z-direction. Some important (Lorentz invariant) variables for the description of the kinematics of the ep scattering are:

- the center of mass energy squared of the ep system:

$$s = (p + k)^2 \simeq 4E_e E_p \tag{1.1}$$

  where the approximation is made by neglecting the rest masses of the particles.

- the virtuality (negative of the invariant mass squared) of the exchanged boson (photon):

$$Q^2 = -q^2 = -(k - k')^2 \simeq 2E_e E_e'(1 + \cos\theta_{e'}) \tag{1.2}$$

  E_e' and $\theta_{e'}$ are the energy and the angle of the scattered positron. The upper limit of Q^2 is s: $Q^2 \leq s$.

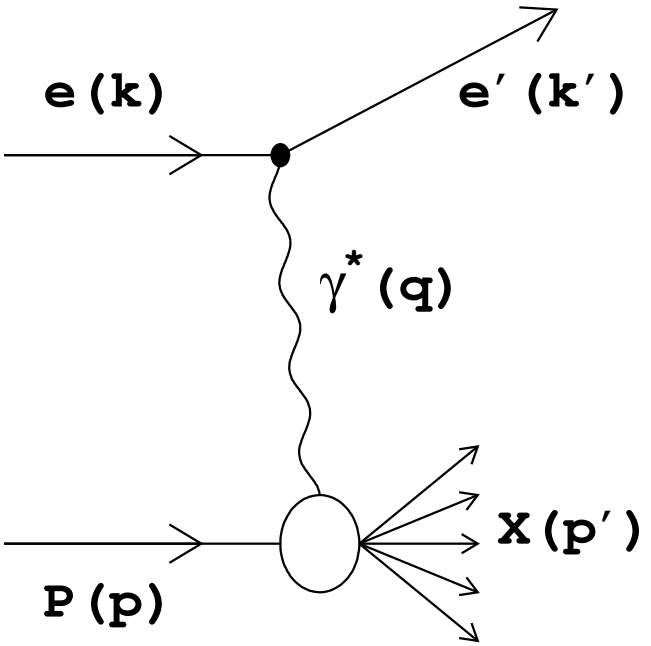

Figure 1.1 - Diagram for single photon exchange in ep scattering. The four momenta are given in brackets.

- The Bjorken variable x is (in the QPM) the fraction of the proton momentum taken by the struck quark:

$$x = \frac{Q^2}{2p \cdot q} \tag{1.3}$$

- the inelasticity y is the relative energy transfer from the positron to the proton in the proton rest frame:

$$y = \frac{p \cdot q}{p \cdot k} \simeq 1 - \frac{E_e'}{E_e}\frac{1 - \cos\theta_{e'}}{2} \tag{1.4}$$

- the center of mass energy squared of the photon-proton ($\gamma^* p$) system

$$W^2_{\gamma^* p} = (q + p)^2 \simeq sy - Q^2 \tag{1.5}$$

- the (absolute) energy transfer from the positron to the proton in the protons rest frame:

$$\nu = \frac{p \cdot q}{m_p} \simeq \frac{Q^2}{2m_p x} \tag{1.6}$$

The variables Q^2, x, and y are not all independent. They are related through the following formula:

$$Q^2 = s \cdot x \cdot y \tag{1.7}$$

1.2.2 Structure Functions

In DIS ep experiments the emitted high Q^2 virtual photons are used to probe the proton structure. The momentum transfer (squared) can be related to the wavelenth of the virtual boson through the Heisenberg uncertainty principle:

$$\lambda \simeq \frac{\hbar}{\sqrt{Q^2}} \tag{1.8}$$

The smaller λ, the higher is the resolution power of the photon. At higher Q^2 the resolution increases and $q\bar{q}$ pairs originating from gluons can be resolved. Processes like the QCD-Compton and Boson-Gluon-Fusion (BGF) become "visible".

The *Deep Inelastic Scattering* regime is the one where Q^2 is much larger than the mass squared of the proton (and $x \neq 1$). In this regime, the proton can be thought of as a group of quasi-free constituents one of which interacts with the photon while the rest (proton remnant) moves unperturbed.

The Born cross section for *Neutral Current* (NC) DIS can be written in terms of the structure functions of the proton F_i as follows [Ha84]:

$$\frac{d^2\,\sigma(e^{\pm}p)}{dx\;dQ^2} = \frac{2\pi\alpha^2}{xQ^4} \cdot \left[\, Y_+ \cdot F_2(x,Q^2) \;-\; y^2 \cdot F_L \;\mp\; Y_- \cdot xF_3(x,Q^2) \,\right] \tag{1.9}$$

where: $Y_\pm = 1 \pm (1-y)^2$ and $F_L = F_2 - 2xF_1$. The structure function $F_3(x,Q^2)$ is the parity violating term of the cross section due to the weak interaction. In the case of Z^0 exchange at high Q^2, where Z^0 exchange becomes important ($Q^2 \simeq m^2_{Z^0}$), the cross section has contributions from the photon, the Z^0, and their interference.

The structure functions F_1, F_2, and F_3 can be interpreted in terms of the parton density functions in the proton (hadron).

Within the single-photon approximation, the ep cross section can be written as a product of the photon flux with the (virtual) photon-proton scattering $\sigma^{\gamma^* p}_{tot}$, provided the photon lifetime is longer than its interaction time with the proton. Virtual photons can be transversely or longitudinally polarised. The cross section can therefore be written as a sum of two parts - the longitudinal and the transverse one:

$$\sigma^{\gamma^* p}_{tot} = \sigma_L + \sigma_T \tag{1.10}$$

The structure functions F_i can be related to these transverse and longitudinal cross sections as follows:

$$F_1 = \frac{Q^2}{8x\pi^2\alpha} \cdot \sigma_T\,; \quad F_2 = \frac{Q^2}{4\pi^2\alpha} \cdot (\sigma_T + \sigma_L)\,; \quad F_L = \frac{Q^2}{4\pi^2\alpha} \cdot \sigma_L \tag{1.11}$$

The structure functions F_i are defined with respect to the Born cross section in equation 1.9. One has to note that the measured NC cross section changes from that cross section by a factor $1 + \delta_r(y, Q^2)$. These are the QED radiative corrections and have to be taken into account if one wants to extract the structure functions from the measured cross sections.

1.3 Quark Parton Model

Models to describe the proton structure and that of other hadrons, are based on the *Parton Model* of Feynman [Fe69] and the *Quark Model* by Gell-Mann and Zweig [Ge64]. In the parton model the proton is considered to consist of (quasi) free point-like objects, called partons. Each parton i carries a fraction of the total momentum of the proton: $p_i = \xi_i \cdot p$. p is the total momentum of the proton, p_i is the momentum of parton i, and $0. \leq \xi_i \leq 1$. The inelastic ep cross section is then given as the incoherent sum of (cross sections of) elastic electron parton scatterings.

In the infinite momentum frame of the proton all the transverse momenta are negligible. In this frame the scaling variable x has received a simple interpretation, it can be interpreted as the fractional longitudinal momentum carried by the struck parton, so it is the same as ξ. Indeed, if we denote by ξ the fractional longitudinal momentum carried by the struck parton, neglecting the proton (and parton) masses, we have:

$$0 \simeq m^2 = (\xi p + q)^2 = \xi^2 p^2 + q^2 + 2\xi qp = \xi^2 p^2 - Q^2 + 2\xi qp \Rightarrow$$

$$\xi = \frac{Q^2}{2pq} = x \tag{1.12}$$

Bjoerken and Paschos suggested (1969) that the fermions which made up the proton according to the two models (partons and quarks) were one and the same thing. Thus the model is called the *Quark Parton Model*.

Since in the Quark Parton model the partons are pointlike, an increase in the momentum transfer Q^2 will not make any new details visible. So one would expect the structure functions to be independent of Q^2. This effect is called *scale invariance*, or shortly *scaling*. Scaling was predicted (1968) by Bjorken. In the high energy limit $Q^2 \to \infty$ but $x = Q^2/2pq$ finite, the structure functions depend only on the dimensionless (scaling) variable x:

$$\begin{aligned} F_1(x,Q^2) &\longrightarrow F_1(x) \\ F_2(x,Q^2) &\longrightarrow F_2(x) \end{aligned} \tag{1.13}$$

The scaling behaviour was confirmed by the SLAC measurements[Bl69].

In the infinite momentum frame, due to Lorentz contraction and relativistic time dilatation, the rate at which partons interact with one another is slowed down. During the time the (virtual) photon interacts with the quark, the quark itself is essentially a free particle, not interacting with the other quarks in the proton. In other words, the parton distributions during the ep collision are effectively "frozen", so that only one parton takes part in the interaction. The probability for an additional parton to take part in the interaction is suppressed as $1/(\pi r_p^2 Q^2)$, where r_p is the radius of the proton. Therefore the ep interaction can be seen as an incoherent sum of scatterings of the electron with the quasi-free quarks in the proton.

In the QPM the structure functions F_1 and F_2 are related to the parton distributions functions of the proton. The structure function F_2 is the charge square weighted sum of the first momenta (momenta densities) in x of the parton distribution functions:

$$F_2(x) = \sum_i e_i^2 x f_i(x) \tag{1.14}$$

where the contributions of $q\bar{q}$ pairs from the sea are neglected. The charges e_i are given in units of the proton charge e. The QPM relates also the structure functions F_1 and F_2 to one another:

$$F_1(x) = \frac{1}{2x} F_2(x) \tag{1.15}$$

The above relation is known as the Callan-Gross relation [Ca69]. It implies that the structure function F_L is zero. This can also be proven using general considerations. By applying the helicity conservation in the Breit frame [Ha84] one can prove that the quarks in the QPM can only couple to transversely polarised photons. Therefore, $\sigma_L^{\gamma^* p} = 0$ is zero $\Rightarrow F_L = 0$.

The QPM was very succesful in explaining many results obtained in the ep experiments. This model is though not perfect and some problems became apparent. One of them is the prediction that all the proton momentum is carried by quarks. The experimental data proved this prediction to be wrong. In fact, from measurements:

$$\sum_i \int_0^1 dx\ x f_i(x) \simeq 0.5 \tag{1.16}$$

The surprise was that less than 50% of the proton's momentum is carried by the quarks. That is most of it is carried by neutral particles. Also the fact that no free quarks can be observed experimentally could not be explained by the QPM. In the not so naive parton model Z^0-boson exchange and QCD gluon radiation are considered. In this improved approximation the quark density functions become a function of Q^2 and x, partially losing its intiutive meaning. The structure function F_2 becomes too a function of Q^2 and x and in the sum over quarks the sea quarks and antiquarks are included.

The problem is treated more rigorously in the Quantum Chromodynamics (QCD), the field theory of strong interactions. In the limit $Q^2 \to \infty$ QCD reproduces the QPM.

1.4 QCD

Quantum Chromodynamics (QCD) is the gauge theory of strong interactions of quarks and gluons. QCD is a non-Abelian gauge theory based on the SU(3) colour symmetry group. Colour in QCD is the equivalent of charge in the electromagnetic interactions. The quarks can have one of three colours. They interact by the exchange of gluons, which are electrically neutral but form a colour charge octet. Gluons were experimentally observed through three-jet events at the PETRA collider at DESY in 1979. The gluons themselves interact strongly since they are not colour neutral. A consequence of this property is the *asymptotic freedom*, which states that the interaction strength of two coloured objects decreases as the distance becomes shorter (see 1.17).

Another property of QCD is *confinement*, which keeps quarks bound into colourless hadrons. This prevents the observation of free quarks. The colour degree of freedom and confinement explain why observed hadrons are made either of $q\bar{q}$ or of triple-quark states. These combinations ensure that the hadrons are colourless and have integer electrical charge. In the presence of QCD, the naive QPM picture of hadrons has to be altered to take into account the radiation and absorption of gluons by quarks as well as the radiation of $q\bar{q}$ pairs by gluons.

QCD has properties which make it much more difficult to work with theoretically than electroweak theory. The strong coupling constant α_s is large. This makes the use of perturbation theory very difficult. The effective (strong) coupling constant α_s depends on the scale at which the QCD process occurs, on the number of quark flavours, and on a free scale parameter:

$$\alpha_s(Q^2) = \frac{4\pi}{(11 - 2n_f/3)\ln(\frac{Q^2}{\Lambda^2})} \tag{1.17}$$

Q^2 is the scale at which α_s is probed. Λ is a QCD cut-off parameter. Measurements show that $\Lambda \simeq 200$ MeV (Particle Data Group: [Gr00]). The (known) number of flavours n_f is 6, so $(11 - 2n_f/3)$ is positive. At large scale Q^2, α_s is small and the quarks are quasi-free. In this region of asymptotic freedom perturbative QCD (pQCD) is applicable and predictions on the properties of strong interactions can be made.

1.4.1 Factorization

Hadron-Hadron and Lepton-Hadron interactions are described in QCD as an incoherent sum of the interaction of the constituents/partons (quarks, gluons) from one hadron with those of the other hadron or with the lepton[4]. The distributions of partons bound in hadrons cannot be calculated from first principles.

A separation of the short-ranged (hard processes) and long-ranged (soft-processes) physics is introduced. This separation is called *factorization*. The QCD factorization

[4]The total cross section of the interaction is an incoherent sum of the cross sections of the interactions of the constituents.

theorem [Co85] states that for hard scattering reactions the cross section can be decomposed into the parton densities of incoming particles and the cross section for the hard process (see figure 1.2). In a simplified form, this can be written:

$$\sigma = f_{i/1}(x_1, \mu_F) \otimes \sigma_{i,j}(q, \mu_F, \alpha_s) \otimes f_{j/2}(x_2, \mu_F) \tag{1.18}$$

$f_{i/1}(x_1, \mu_F)$ and $f_{j/2}(x_2, \mu_F)$ are the parton densities of the incoming particles, while $\sigma_{i,j}(q, \mu_F, \alpha_s)$ is the cross section (matrix element) for the hard scattering of the two partons i and j. The convolutions $\otimes$ imply implicit integration over the fractions x_1 and x_2 of the momentum of the colliding particles carried by the partons i and j.

The parton distribution functions are the probability to find a particular quark having a momentum fraction in the range $(x, x + dx)$. So $f_{i/1}(x_1, \mu_F) \cdot dx_1$ is the probability to find the parton i in the first hadron carrying a fraction x_1 of its momentum.

Generally, parton distribution functions give the probability to find partons (quarks and gluons) in a hadron as a function of the fraction x of the hadron's momentum they carry.

In order to use the factorization, a hard scale μ_F - the factorization scale - has to be introduced for separating the short-ranged from the long-ranged physics. The long-ranged (non perturbative) processes are absorbed in the parton distribution functions. The parton distribution functions are assumed to be universal, process independent. Perturbative QCD does not predict them and their values are fixed from experimental results.

On the other hand, the cross section for the hard process is a short-ranged process and can be perturbatively calculated.

Apart from this, pQCD introduces another scale μ_R - the renormalization scale. By introducing the renormalization scale the divergences coming from the calculation of self-energy diagrams (which yield divergent integrals) are absorbed into the definition of long-ranged parton distribution functions (pdfs). Several renormalization schemes are used, the most importants being the *minimal subtraction scheme* - $\overline{MS}$ and the *deep inelastic scattering scheme* - DIS.

1.4.2 QCD evolution equations

The Q^2 dependence of the parton distribution functions can be calculated within pQCD. The main origin of this dependence is that a quark seen at a certain scale Q_0^2 as carrying a certain fractional momentum of the hadron x_0 can be resolved into more quarks and gluons if we probe it at a higher scale Q^2. The resolved quarks and gluons carry a smaller fractional momentum of the hadron ($x < x_0$). The change of the structure function F_2 with increasing scale is schematically shown in figure 1.3. Thus, if the whole QCD dynamics is included, the structure function F_2 is expected to rise at low x. This is because the low x region is populated by gluons and sea quarks and the quark density is large. The resulting logarithmic dependence of F_2 on Q^2 at fixed x is known as *scaling violation*. At HERA, the structure function F_2 has been measured in a very wide range of Q^2 and x and the scaling violation for low x has been demonstrated. This is shown in figure 1.4.

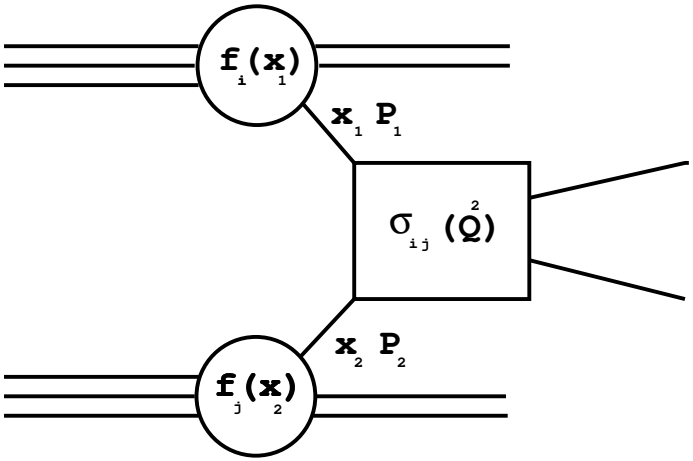

Figure 1.2 - Factorization: separation of the short-ranged and long-ranged physics. The parton distributions in the hadrons are not perturbatively calculable (long-ranged physics). The hard cross section $\sigma_{ij}(Q^2)$ is perturbatively calculable (short-ranged physics).

The DGLAP equations (DGLAP:Dokshitzer - Gribov - Lipatov - Altarelli - Parisi [Al77]) are a set of $(2n_f + 1)$ coupled integro-differential equations. They can be used to determine the quark and gluon distribution functions for any value of Q^2 if one knows them at one particular value Q_0^2 within the range of applicability of perturbative QCD. These equations are derived by requiring that the structure functions F_1 and F_2 be independent of the choice of the factorization scale μ_F. This condition can be written: $\mu_F^2(dF_i(x, Q^2)/d\mu_F^2) = 0$, where $i = 1, 2$. The DGLAP equations were derived in the *leading log approximation* - LLA. The terms which give the dominant contributions at large x and Q^2 were summed to all orders. All other terms were neglected.

In a compact form the DGLAP equations can be written as:

$$\frac{\partial}{\partial \ln Q^2} \begin{pmatrix} q \\ g \end{pmatrix} = \frac{\alpha_s(Q^2)}{2\pi} \begin{bmatrix} P_{qq} & P_{qg} \\ P_{gq} & P_{gg} \end{bmatrix} \otimes \begin{pmatrix} q \\ g \end{pmatrix}, \tag{1.19}$$

$q(x, Q^2)$ and $g(x, Q^2)$ are the quark and gluon distributions. The convolution $\otimes$ denotes an integration. The parameters $P_{ij}(x)$ are called splitting functions. They describe the probability to find a parton of type i with given fractional momentum originating from the parton of type j (i, j can be q, g). Given a specific factorization and renormalization scheme, the splitting functions are obtained in pQCD as an expansion series in α_s:

$$\frac{\alpha_s}{2\pi} P_{ij}(x, Q^2) = \frac{\alpha_s}{2\pi} P_{ij}^{(1)}(x) + (\frac{\alpha_s}{2\pi})^2 P_{ij}^{(2)}(x) + ... \tag{1.20}$$

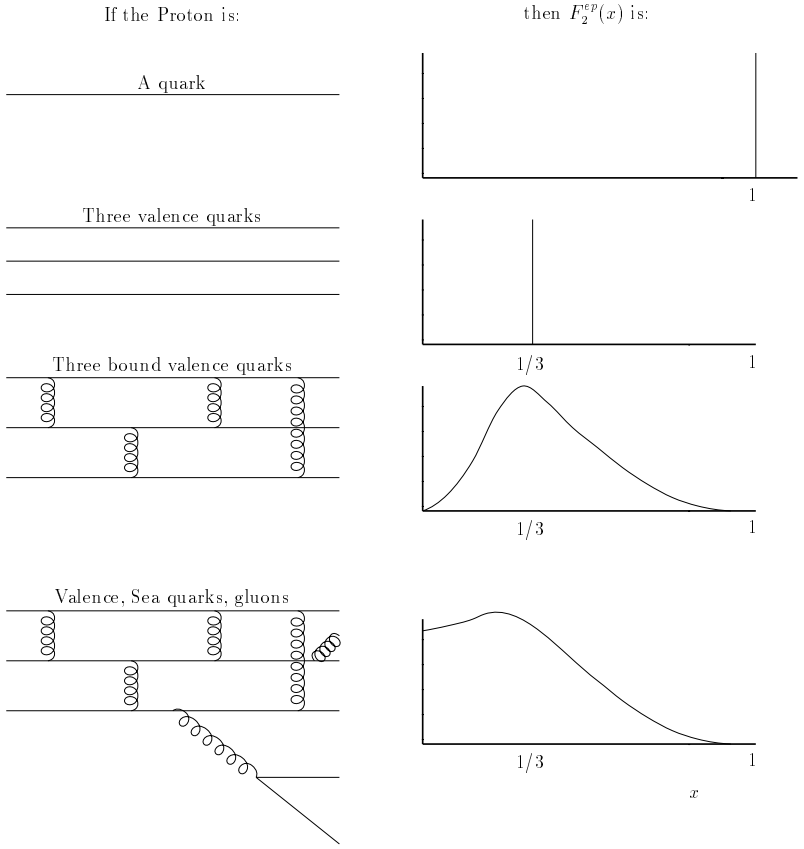

Figure 1.3 - Behaviour of the structure function F_2 with increasing scale. The two top pictures show the case of QPM. The two bottom pictures show the changes when QCD effects are included (from: [Ab98]).

The truncation after the first two terms in the series defines the next to leading order (NLO) DGLAP evolution.

The DGLAP equations are valid as long as the impact of the neglected terms is small. At very low x this is not true any more. At this region another approach is used and the calculations lead to the BFKL (Balitsky - Fadin - Kuraev - Lipatov: [Ku76]) equations. DGLAP deals with the Q^2 evolution and is inadequate at very low x. BFKL deals with the $\frac{1}{x}$ evolution and is inadequate at large Q^2.

The inclusive measurement of F_2 at HERA has shown that the evolution of structure functions through the DGLAP equations is in good agreement with the experimental results (figure 1.4). Until now it has not been possible to discriminate between

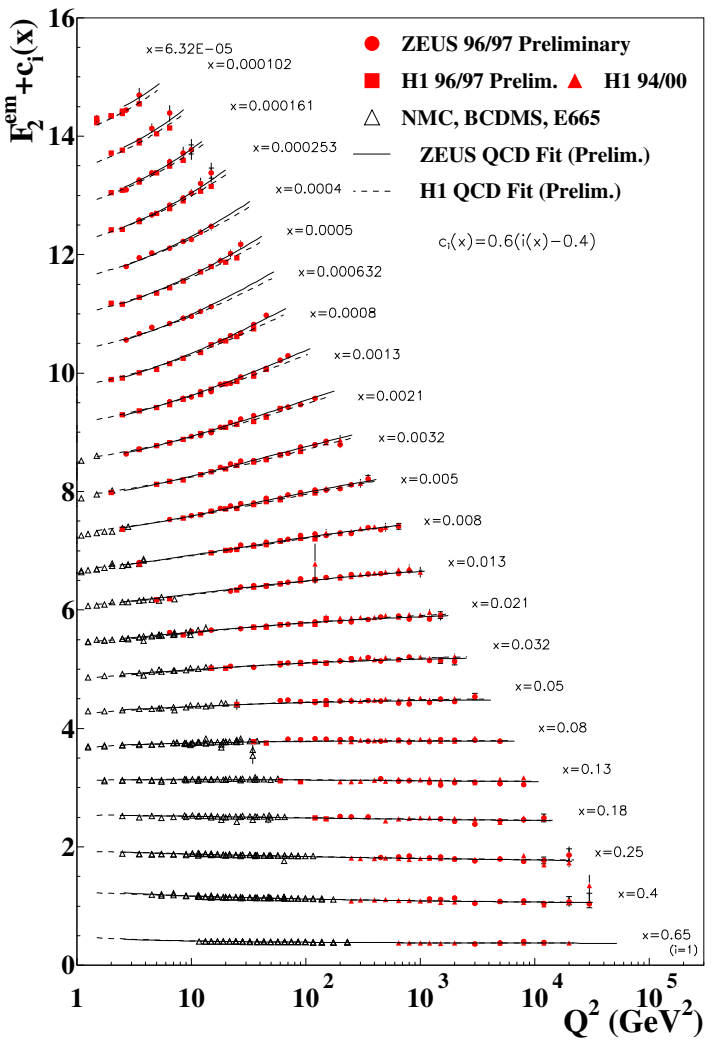

Figure 1.4 - Scaling violations - the structure function F_2 versus the scale Q^2 for different values of x. The structure function F_2 is not independent of Q^2. The F_2 measurements for different x have been scaled by constant factors in order for all of them to fit on the same plot.

DGLAP and BFKL equations. The differences could show up in the exclusive measurements such as high p_T forward jets and in the forward energy flow.

Attempts have been made to achieve a unified DGLAP / BFKL description. Evolution equations which allow an evolution in Q^2 as well as in x are considered in the CCFM evolution equations.

1.5 Photoproduction

In contrast with the high Q^2 regime which has been defined as DIS, the kinematical regime where Q^2 is very small ($Q^2 \simeq 0$) is called *Photoproduction*. In the photoproduction events the scattered electron has a very small angle with respect to the incoming one. Therefore, most of the time it goes undetected in the beam pipe[5]. The exchanged photons in photoproduction are quasi real.

In photoproduction the hard scale of the interactions is not given by Q^2 since Q^2 is very small. In this case the hard scale is given by the transverse energy of the (hard) outgoing partons. The situation now is reversed and the proton is not anymore being probed by the photon. In fact, the photon is being probed by the hard partons from the proton.

This will be discused in more detail in the section 2.4.1.

[5] At HERA, in some cases the scattered electron can be detected in the luminosity detector (Lumi-Electron)

Chapter 2

Introduction to Photon Structure

2.1 Photon Structure

In the context of the Standard Model, the photon is a fundamental, spin one, gauge boson which mediates the electromagnetic interaction. Photons have no mass, no intrinsic structure and no self couplings. Therefore, the concept of the photon structure seems at first paradoxical.

It is well known that the photons couple to particles that carry charge. Hence, photons can fluctuate to fermion-antifermion pairs. These fluctuations, at high photon energies, can live long enough so that the photon interactions with matter can proceed via the interactions of the fermion-antifermion pairs with matter. In such cases the photon interactions can be conveniently described using the concept of photon structure which is similar to (and borrowed from) the concept of the proton structure.

Fundamental differences between photon and proton structures arise from the fact that the photon structure is completely driven from the quantum fluctuations of the photon to fermion-antifermion pairs whereas a considerable part of the proton structure arises from the contributions of the valence quarks which are absent in the case of the photon structure. Therefore, the photon structure functions, unlike those of the proton, exhibit scaling violations already at the quark-parton-model (QPM) level without any need for gluon emission or absorption diagrams.

Measurements of the photon structure allow tests of QED and QCD (depending if the photon fluctuates to charged leptons or quarks). One can therefore speak of "electromagnetic" and "hadronic" structure of the photon.

2.1.1 Hadronic Photon Structure

Photon fluctuations to $q\bar{q}$ pairs are described by QCD [Sc93]. According to QCD, the final state $q\bar{q}$ can radiate gluons, which can further produce quarks. The collection of all final state quarks and gluons, the "quark-gluon cloud", represent the photon structure.

In this picture, the physical photon can be seen as a superposition of a bare (point-

like) photon (γ_B), refering to the case where the photon does not fluctuate but remains a pointlike photon, and a resolved component (R), where the photon fluctuates:

$$|\gamma> = Z_3^{1/2}\,|\gamma_B> + c\cdot\alpha^{1/2}\,|R> \tag{2.1}$$

Z_3 and $c\cdot\alpha$ are normalization constants. The state $|R>$ must have the same quantum numbers as the photon.

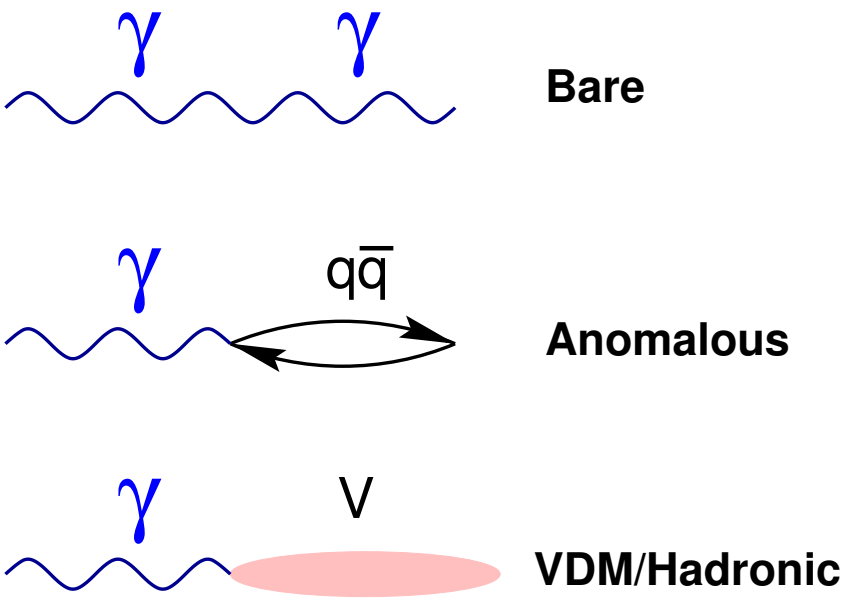

Figure 2.1 - A photon can be bare (pointlike) or fluctuate into a $q\bar{q}$ pair. Low virtuality fluctuations are give rise to vector meson states. From top to bottom, the three components of the photon: bare, anomalous, and VMD component.

The lifetime of the fluctuation $\gamma \to q\bar{q}$ pair is given by the Heisenberg uncertainty principle as:

$$\Delta t \leq \frac{\hbar}{\Delta E} \tag{2.2}$$

where $\Delta E = E_\gamma - E_{q\bar{q}}$ is the energy difference of the photon and the quark-antiquark pair. The virtuality of the $\gamma \to q\bar{q}$ is characterized by the common p_T^2 of the quark and antiquark with respect to the photon direction. Depending on the lifetime of the fluctuations of the photon in $q\bar{q}$, one can distinguish two components of $|R>$. When the virtuality of the photon is small ($\Rightarrow \Delta E$ small) the fluctuation is long-lived. There is then time for a cloud of soft gluons to develop around the $q\bar{q}$ pair, which

forms in this case a bound state with the same quantum numbers as the photon. This process is non-perturbative and the description of this component is based on phenomenology. The vector meson dominance model (VMD) [Sa69] is usually used to describe the non-perturbative component of the hadronic fluctuations of the photon.

In the vector meson dominance model the photon fluctuates into a vector meson: $\gamma \leftrightarrow V$. The lifetime of such a fluctuation is given by:

$$\tau_\gamma^V \simeq \frac{2\hbar\cdot E_\gamma}{m_V^2 + Q^2} \tag{2.3}$$

where E_γ is the energy of the photon, m_V is the mass of the vector meson, and Q^2 is the photon virtuality [1]. The lifetime of the vector meson state becomes shorter with increasing photon virtuality and dies out as $\frac{1}{m_V^2+Q^2}$ with Q^2.

Since the vector meson must have the same quantum numbers as the photon, it has to be a flavour-diagonal vector meson[2]. In the simplest formulation, the VMD asserts that the sole hadronic components of the photon are the three light vector mesons ρ^0, ω, and ϕ. For the VMD component of the photon we could then write:

$$|\gamma_{VDM}> = \sum_{\rho^0,\,\omega,\,\phi} \frac{e}{f_V}\,|V> \tag{2.4}$$

Here $(\frac{e}{f_V})^2$ are the probabilities for the transition of the photon into the respective vector meson. These coefficients are based on low-energy fits and are assumed to be energy independent. Numerically: $f_V^2/4\pi = 2.20,\ 2.36,\ 18.4$ respectively for $\rho^0,\ \omega,\ \phi$. In the generalized vector meson dominance model (GVD) also vector mesons with higher masses are included in the above sum.

When the virtuality is large ($\Rightarrow \Delta E$ large), the fluctuation is short-lived and no bound hadronic state can develop. In this case, a perturbative description is possible. This is the so called anomalous photon component ("pointlike" photon structure), which originates from the perturbative splitting $\gamma \to q\bar{q}$ and the subsequent QCD evolution. This component can be written as:

$$|\gamma_{perturbative}> = \frac{e}{f_{q\bar{q}}}\,|q\bar{q}> \tag{2.5}$$

[1] Lets denote by $q = (E_\gamma, \vec{q})$ the four-momentum of the photon and by $V = (E_V, \vec{p}_V)$ that of the vector meson. Because of momentum conservation $\vec{q} = \vec{p}_V$. The virtuality is $Q^2 = -q^2 = \vec{q}^2 - E_\gamma^2 = \vec{p}_V^2 - E_\gamma^2$. Therefore $\vec{p}_V^2 = Q^2 + E_\gamma^2$.

From the Heisenberg Principle: $\Delta E\cdot\tau_\gamma^V \simeq \hbar$, where τ_γ^V is the lifetime of the fluctuation of the photon in a vector meson and ΔE is energy difference between the two states: $\Delta E = E_V - E_\gamma = \sqrt{\vec{p}_V^2 + m_V^2} - E_\gamma$

$\Rightarrow \Delta E = \sqrt{E_\gamma + Q^2 + m_V^2} - E_\gamma$. The vector meson model is valid for photons of small virtualities (Q^2 small). On the other hand, the mass of the vector meson is much smaller than its energy. So $E_\gamma \gg Q^2 + m_V^2$. With this assumption: $\Delta E \simeq \frac{Q^2+m_V^2}{2E_\gamma} \Rightarrow \tau_\gamma^V \simeq \frac{2\hbar\cdot E_\gamma}{m_V^2+Q^2}$.

[2] As the spin has to be unity and the charge 0

Here $(\frac{e}{f_{q\bar{q}}})^2$ is the probability of the transition of the photon in the quark-antiquark pair.

In total, the photon has three possible states: bare (pointlike), Vector-Meson, and perturbative (anomalous). In general one can finally write:

$$|\gamma> = Z_3^{1/2}\,|\gamma_B> + \frac{e}{f_{q\bar{q}}}\,|q\bar{q}> + \sum_{\rho^0,\,\omega,\,\phi}\frac{e}{f_V}\,|V> \tag{2.6}$$

where, for a proper normalization, $Z_3 + (\frac{e}{f_{q\bar{q}}})^2 + \sum_{\rho^0,\,\omega,\,\phi}(\frac{e}{f_V})^2 = 1$. These three components of the photon are represented schematically in figure 2.1.

Most of the time, the photon is a pointlike particle ($Z_3 \simeq 1$). But since the hadronic cross section are very large the (γ^* - hadron) cross sections are dominated by the VMD and anomalous components.

2.2 Photon Structure in e^+e^- experiments - F_2^γ

Originally the photon structure has been studied in e^+e^- experiments. In e^+e^- scattering two photons are emitted from the positron and the electron which interact with one another so that the process can be seen as $\gamma\gamma^{(*)}$ scattering. The process is therefore sensitive to the structure of the photon. The first measurements of the photon structure function were made at PETRA / DESY in Hamburg [PL84]. One of these measurements from the PLUTO collaboration is shown in figure 2.2.

The underlying kinematics in e^+e^- interactions is shown in figure 2.3. The initial state consists of the incoming electron and positron. Each of them emitts a (virtual) photon. The following invariants can be constructed:

- the virtualities of the photons calculated as (minus) squared momenta of them:

$$\begin{aligned} Q^2 &= -q^2 = -(k-k')^2 &&= 4E_0E_1'\sin^2(\theta_1'/2) \\ P^2 &= -p^2 = -(l-l')^2 &&= 4E_0E_2'\sin^2(\theta_2'/2) \end{aligned} \tag{2.7}$$

  What is called P^2 and Q^2 is a matter convention. Usually Q^2 is the highest virtuality and P^2 the smallest. The photon with the highest virtuality is called the “probe photon” while the photon with the smallest virtuality is called the “target photon”.

- The center of mass energy squared of the $\gamma\gamma$ system:

$$W_{\gamma\gamma}^2 = (p+q)^2 \tag{2.8}$$

- The Bjorken variable is denoted here with x_γ. It is the fractional momentum of the photon taking part in the hard interaction:

$$x_\gamma = \frac{Q^2}{2p\cdot q} = \frac{Q^2}{Q^2 + W_{\gamma\gamma}^2 + P^2} \tag{2.9}$$

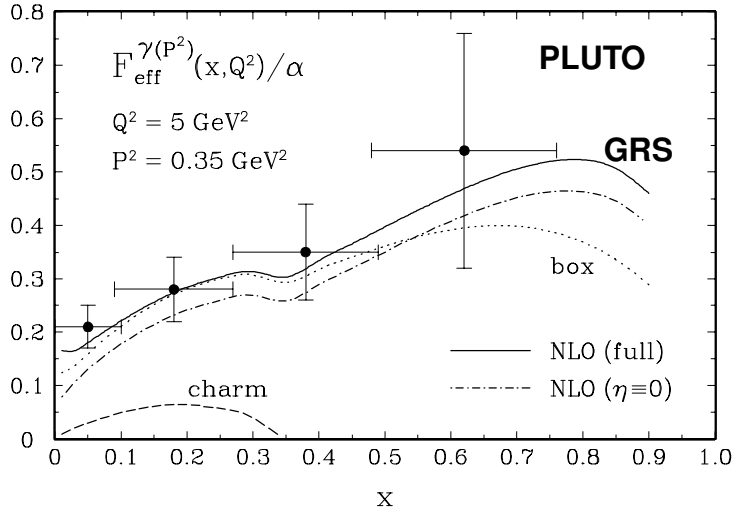

Figure 2.2 - Measurement of photon structure in e^+e^- experiments. The $F_{2,\mathrm{eff}}^\gamma$ versus x.

- $$y = \frac{p\cdot q}{p\cdot k} \tag{2.10}$$

Three event classes can be distinguished depending on whether the final state electron is tagged or not.

1. If both electrons are not tagged - *anti-tagged / untagged* events - both virtualities Q^2 and P^2 are small and the two photons are considered to be quasi-real. The smallness of the virtualities depends on the detector acceptance.
2. One of the electrons is tagged - *single-tagged* events. In this case, the process of figure 2.3 can be considered as scattering of an electron off a quasi real photon. The quasi real photon has a virtuality $P^2 \simeq 0$ and the hard scale is the virtuality of the tagged photon $Q^2 > 0$. In this case, the structure of the quasi real photon can be probed from the virtual photon in a similar way to the ep scattering (HERA) where the proton structure is probed using a virtual photon.
3. Both electrons are tagged - *double-tagged* events. In this case both virtualities can be measured and a study of the photon structure for different virtualities P^2 is possible. Given the difficulty of doing double-tagged measurements, the statistics for this class of events is poor in comparison to the other two classes above.

The cross section for the reaction $ee \longrightarrow eeX$ can be written:

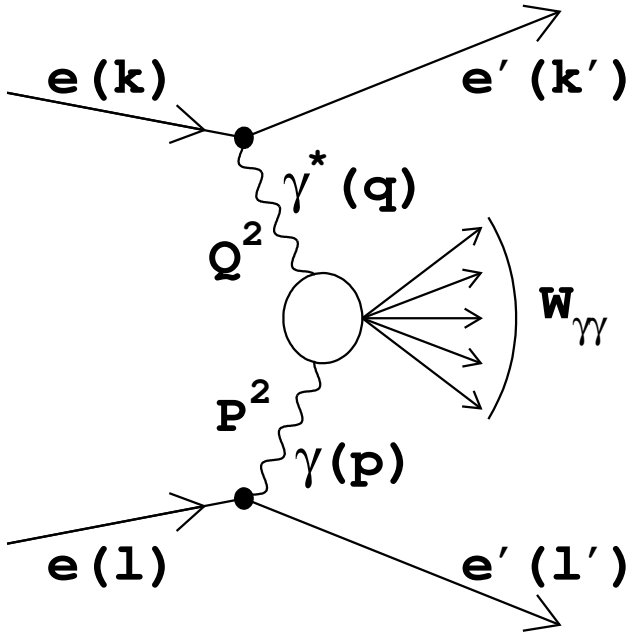

Figure 2.3 - Kinematics of two-photon induced processes in e^+e^- collisions. k/k' and l/l' are the four-momenta of the incoming/outgoing electrons (positrons). The four momenta are written in brackets for all the components. The photon with the smallest virtuality (P^2) is the target photon while the one with the highest virtuality Q^2 is the "probe photon".

$$\sigma_{ee\to eeX} = \sigma_{e\gamma\to eX} \cdot f^e_\gamma \tag{2.11}$$

The flux factor f^e_γ denotes the flux of the target photon from the incoming electron. This flux takes into account the momentum spread of the target (quasi-real) photon. The calculation of this flux is carried out using the Equivalent Photon Approximation - EPA (see also section 2.4.3).

Since the target photon is almost real ($P^2 \simeq 0$), in most cases it has (almost) only transverse polarization. The $e\gamma \longrightarrow eX$ cross section has only two components:

$$\frac{d^2\sigma(e\gamma \to eX)}{dx_\gamma\, dQ^2} = \sigma_{TT} + \sigma_{LT} \tag{2.12}$$

The first index of the cross sections on the right side of the above relation refers to the polarization of the probing photon. This can be either transverse or longitudinal (T or L) since this photon is virtual. The second index refers to the polarization of the

target (quasi-real) photon and can be only transverse (T). Similarly to the relations (1.11), one can define the photon structure functions using the definitions:

$$\begin{aligned} F_1^\gamma(x_\gamma, Q^2) &= \frac{Q^2}{4\pi^2\alpha}\,\frac{1}{2x_\gamma}\cdot\sigma_{TT} \\ F_2^\gamma(x_\gamma, Q^2) &= \frac{Q^2}{4\pi^2\alpha}\cdot(\sigma_{TT}+\sigma_{LT}) \\ F_L^\gamma(x_\gamma, Q^2) &= F_2^\gamma(x_\gamma, Q^2) - 2x_\gamma F_1^\gamma(x_\gamma, Q^2) \end{aligned} \tag{2.13}$$

The function F_L^γ is the longitudinal structure function. With these definitions, the $e\gamma$ cross section can be rewritten:

$$\frac{d^2\sigma(e\gamma\to eX)}{dx_\gamma\, dQ^2} = \frac{2\pi\alpha^2}{x_\gamma Q^4}\cdot\left[\left(1+(1-y)^2\right)\cdot F_2^\gamma(x_\gamma,Q^2) - y^2\cdot F_L^\gamma(x_\gamma,Q^2)\right] \tag{2.14}$$

Note the similarity with the relation (1.9) for the ep cross section. Here there is no F_3-part since we only have a photon exchange and have ignored the Z^0 exchange.

The inelasticity y can be reconstructed from the tagged electron as follows: $y = 1-(E_{tag}/E_0)\cdot\cos^2(\theta_{tag}/2)$, where E_0 is the energy of the incoming electron (the beam energy). E_{tag} and θ_{tag} correspond to the above E_1' and θ_1'. Usually the energy of the tagged electron is large enough so that y is much less than unity (a cut $E_{tag} > E_0/2$ is often applied to reject beam-gas events). Therefore, the y^2F_L term of the $e\gamma$ cross-section can be neglected. In this approximation, the $\frac{d^2\sigma(e\gamma\to eX)}{dx_\gamma\, dQ^2}$ is directly proportional to $F_2^\gamma(x_\gamma, Q^2)$.

In the case of double-tagged events, the target photon is not quasi-real and can have also transverse polarization. In this case additional terms should be considered in the expression (2.12) for the $e\gamma$ cross-section (σ_{TL}, σ_{LL}, cross terms). The simplifications made above do not hold anymore for this class of events and the F_2^γ contribution to the cross section changes. In measuring $F_2^\gamma(x_\gamma, Q^2)$ one has to correct for the fact that P^2 is not zero.

In leading order (LO) the photon structure function F_2^γ can be expressed as a sum over the charge weighted quark densities of the photon:

$$F_2^\gamma(x_\gamma, Q^2) = \sum_i e_i^2 x_\gamma f_i^\gamma(x_\gamma) \tag{2.15}$$

This concept of the structure function F_2^γ has been developed in analogy with the structure function F_2 of the proton (nucleon), although there are some differences between the two:

* The photon has no valence quarks.
* $F_2^\gamma(x_\gamma, Q^2)$ increases with Q^2 for all x_γ. This scaling violation is expected already within the parton model and it comes from the pointlike anomalous contribution even without introducing gluon radiation.

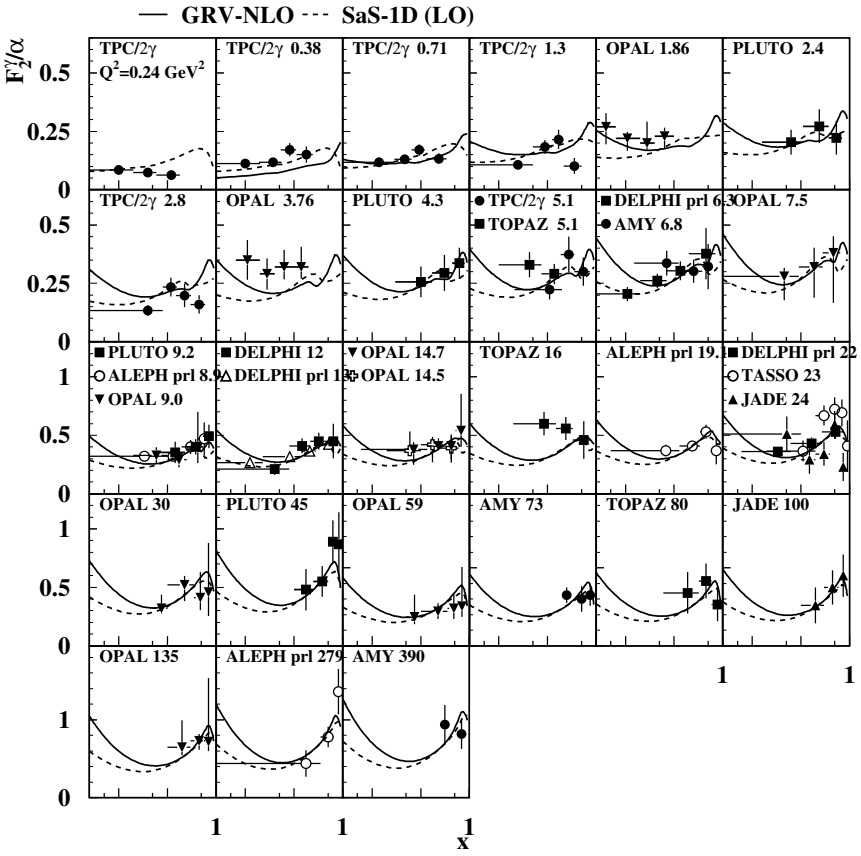

Figure 2.4 - F_2^γ measurements at e^+e^- experiments in different bins of x_γ and Q^2. Note: the variable x on the plots is denoted in the text of the thesis by x_γ. The Q^2 increases from left to right and from top to bottom. The vertical error bars represent the statistical + systematic errors added in quadrature. The horizontal error bars (!) represent the statistical errors only. The mean Q^2 in GeV^2 of each bin is shown also after the experiment mean.

* $F_2^\gamma(x_\gamma, Q^2)$ increases towards $x_\gamma = 1$ while $F_2^{proton}(x, Q^2)$ decreases at large x.

Measurements of F_2^γ versus x_γ (in the plots, this is denoted simply by x) for Q^2 bins in the range $0.2-400$ GeV^2 from different experiments are shown in figure 2.4. If the photon were purely hadronic-like, a steep rise of F_2^γ at low x_γ would be observed, similarly to what HERA has observed for the proton-F_2 at low x. The systematics dominated errors of these measurements are too large to draw exact conclusions. The main systematic problem in extracting F_2^γ is the final-state modeling. A rise at

small x_γ cannot be excluded.

The photon structure function can be written as a sum of two parts:

$$F_2^\gamma = F_2^{\gamma,pointlike} + F_2^{\gamma,hadronic} \tag{2.16}$$

$F_2^{\gamma,hadronic}$ takes into account the vector meson and anomalous contributions. At large x_γ and asymptotically large Q^2, the $F_2^{\gamma,hadronic}$ can be calculated perturbatively (the vector meson part dies out, the anomalous - perturbative contribution remains). In this region one can parametrize this function as [Wi77]:

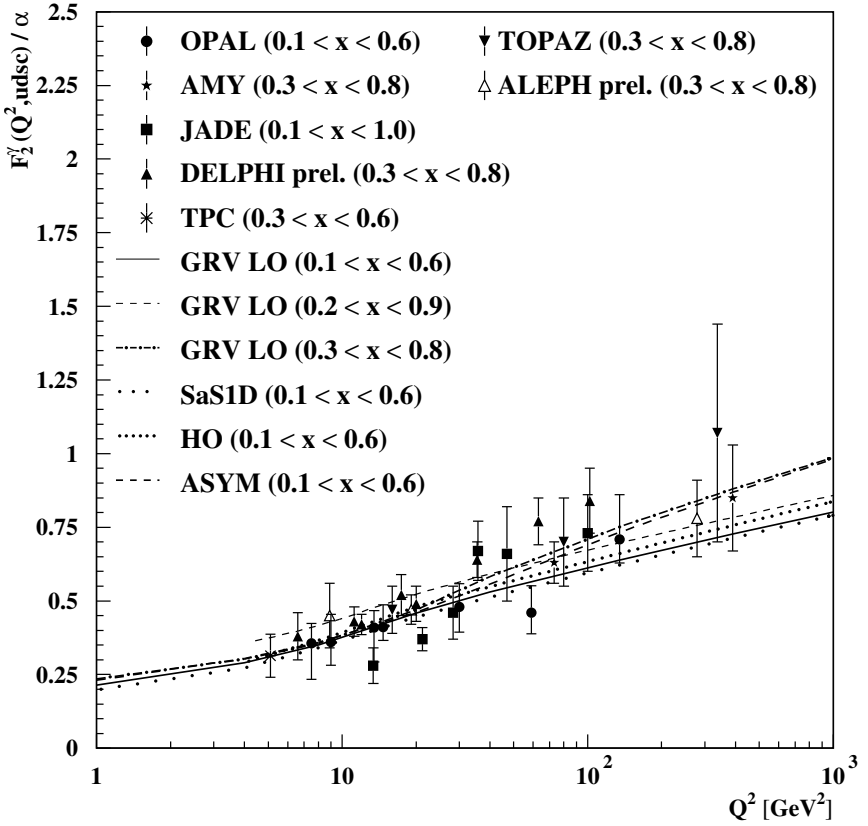

Figure 2.5 - F_2^γ evolution with Q^2. The $\ln(Q^2)$ dependence over a large range of Q^2 values can be seen. Note: the variable x on the plots is denoted in the text of the thesis by x_γ.

$$F_2^\gamma \sim \frac{\alpha(x_\gamma)}{\alpha_s(Q^2)} + b(x_\gamma) \sim a_1(x_\gamma) \cdot \ln(\frac{Q^2}{\Lambda^2}) + b_1(x_\gamma) \tag{2.17}$$

See also the relation (1.17). a, b, a_1, b_1 are functions of x_γ independent of Q^2. The above relation could be used to extract the QCD scale Λ. At $P^2 \simeq 0$ where the contribution from the non perturbative VDM component is expected to be significant, this is no longer possible.

The Q^2 dependence of F_2^γ is shown in figure 2.5. As can be seen, the results are in agreement with the expected $\ln(Q^2)$ behaviour over two orders of magnitude in Q^2. While the Q^2 dependence is predicted in QCD, the x-dependence is much less well constrained.

The class of anti-tagged events is somehow similar to photoproduction at HERA. Jet production (jet cross sections, jet shapes, etc.) is studied in this regime.

2.3 Parton Distribution Functions of the Photon

Similarly to the case of the proton, parton distribution functions (pdfs) are defined also for the photon. A factorization scale μ_F is introduced and all the long range QCD effects which take part below this scale are absorbed in the parton distribution functions of the photon. The short range processes are calculable in QCD (pQCD).

The parton distribution functions are considered to be universal and are determined from the experiment. The Q^2 dependence of the evolution of the parton distribution functions is however predicted by pQCD.

2.3.1 The evolution of the pdfs of the photon

The evolution equations for the parton densities can be written [Vo97]:

$$\begin{aligned}
\frac{dq_i^\gamma}{d\ln Q^2} &= \frac{\alpha}{2\pi}\overline{P}_{q_i\gamma}\otimes\Gamma^\gamma + \frac{\alpha_s}{2\pi}\Big\{2\sum_{k=1}^{n_f}\overline{P}_{q_iq_k}\otimes q_k^\gamma + \overline{P}_{q_ig}\otimes g^\gamma\Big\} \\
\frac{dg^\gamma}{d\ln Q^2} &= \frac{\alpha}{2\pi}\overline{P}_{g\gamma}\otimes\Gamma^\gamma + \frac{\alpha_s}{2\pi}\Big\{2\sum_{k=1}^{n_f}\overline{P}_{gq_k}\otimes q_k^\gamma + \overline{P}_{gg}\otimes g^\gamma\Big\} \qquad (2.18)\\
\frac{d\Gamma^\gamma}{d\ln Q^2} &= \frac{\alpha}{2\pi}\overline{P}_{\gamma\gamma}\otimes\Gamma^\gamma + \frac{\alpha}{2\pi}\Big\{2\sum_{k=1}^{n_f}\overline{P}_{\gamma q_k}\otimes q_k^\gamma + \overline{P}_{\gamma g}\otimes g^\gamma\Big\}.
\end{aligned}$$

where $q^\gamma(x_\gamma, Q^2)$ and $g^\gamma(x_\gamma, Q^2)$ are the quark and gluon distributions in the photon and n_f is the number of active flavours. $\overline{P_{ij}}$ are some generalized splitting functions. The difference between the above equations and the DGLAP equations (1.19) is the presence of the inhomogenous terms connected to the pointlike component of the photon $\Gamma^\gamma(x, Q^2)$. This part does not exist in the case of the proton.

Due to charge conjugation invariance and charge conservation, the antiquark distributions are the same as the quark ones: $\bar{q}_i^\gamma(x_\gamma, Q^2) = q_i^\gamma(x_\gamma, Q^2)$ The singlet quark distributions are then $\Sigma^\gamma = 2\cdot\sum_i^{n_f} q_i^\gamma$. The parton densities are subject to the energy-momentum sum rule:

$$\int_0^1 dx_\gamma\, x_\gamma\Big[\Sigma^\gamma(x_\gamma, Q^2) + g^\gamma(x_\gamma, Q^2) + \Gamma^\gamma(x, Q^2)\Big] = 1 \qquad (2.19)$$

If the calculations are restricted to the first order of the QED coupling constant α ($\alpha \ll 1$), the generalized splitting functions reduce to the usual QCD ones $P_{ij}(x, \alpha_s)$. In this case $P_{\gamma q_i}$ and $P_{\gamma g}$ drop out completely. The third row of the equations (2.18) is in this case very simple and can be immediately integrated. Since the $P_{\gamma\gamma} \sim \delta(1-x_\gamma)$ (the density of the photon in the photon), then the LO expression for Γ^γ will be

$$\Gamma^\gamma_{LO}(x_\gamma, Q^2) = \delta(1-x_\gamma)\Big[1 - \frac{\alpha}{\pi}\Big(\sum_q e_q^2 \ln\frac{Q^2}{Q_0^2} + c_1\Big)\Big] \qquad (2.20)$$

c_1 is a constant. The momentum sum rule holds order by order in α. Using the above expression, the momentum sum rule becomes:

$$\int_0^1 dx_\gamma\, x_\gamma\Big[\Sigma^\gamma_{LO}(x_\gamma, Q^2) + g^\gamma_{LO}(x_\gamma, Q^2)\Big] = \frac{\alpha}{\pi}\Big(\sum_q e_q^2 \ln\frac{Q^2}{Q_0^2} + c_1\Big) \qquad (2.21)$$

The integrated quark and gluon densities do not sum to unity. Instead they logarithmically increase with Q^2. This comes from the presence of the pointlike contribution. Therefore, unlike with the proton case, an important constraint on the parton densities is missing. This constitutes another difference of the photon pdfs with those of the proton.

The general solution of the evolution equations (2.18) has an inhomogenous and a homogenous part:

$$\vec{q}^\gamma = \begin{pmatrix}\Sigma^\gamma \\ g^\gamma\end{pmatrix} = \vec{q}^\gamma_{PL} + \vec{q}^\gamma_{had} \qquad (2.22)$$

The homogenous/hadronic part of the solution $\vec{q}^\gamma_{had}(x_\gamma, Q^2)$ contains a perturbatively uncalculable boundary condition $\vec{q}^\gamma_{had}(x_\gamma, Q_0^2)$. On the other hand, given a Q_0^2, the inhomogenous/pointlike component is completely perturbatively calculable. The quark densities are:

$$q_i^\gamma \sim \frac{1}{\alpha_s(Q^2)} \qquad (2.23)$$

This anomalous $1/\alpha_s(Q^2)$ behaviour of the photon pdfs arises because of the inhomogenous terms coming from the direct coupling $\gamma \to q\bar{q}$.

Because of the perturbatively uncalculable part of the quark (gluon) densities, different parametrisations are used for describing the parton distribution functions in the photon.

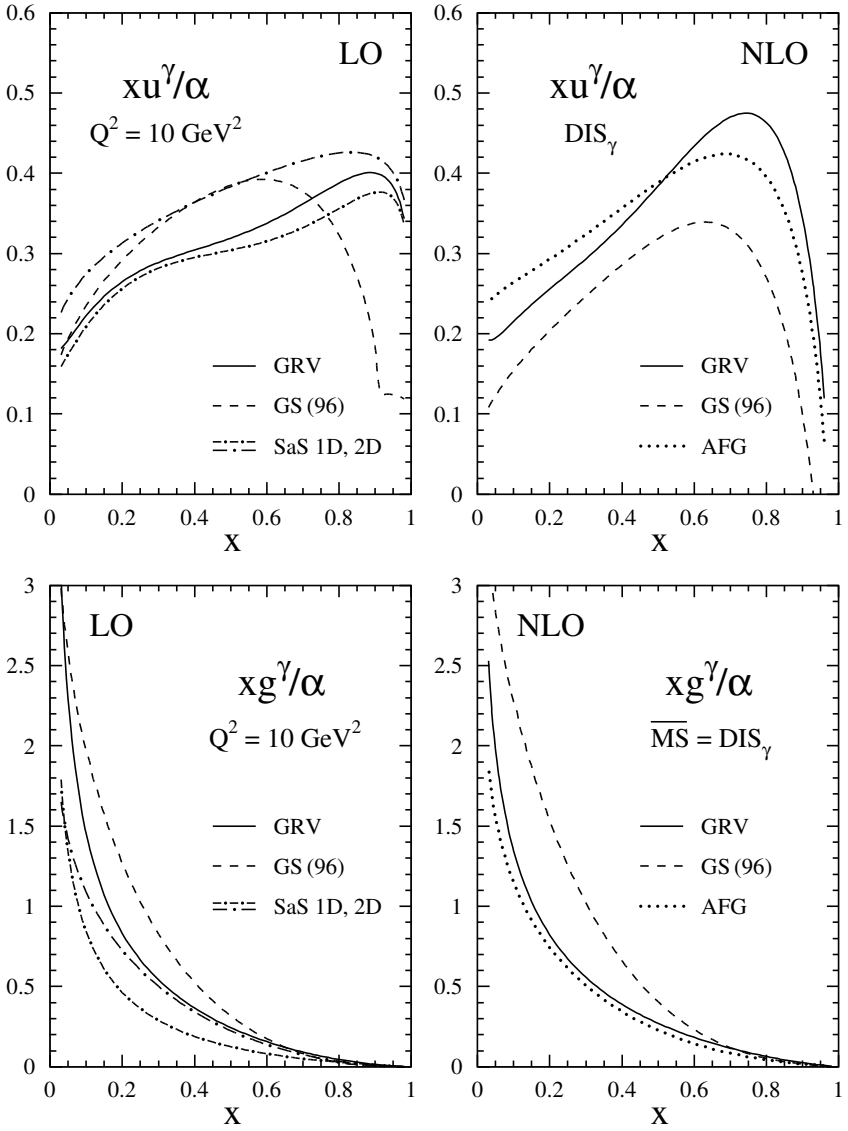

Figure 2.6 - LO and NLO parametrizations of the real photon pdfs [Vo97]. In the above two plots are given the (up) quark densities. The two plots below show parametrizations of the gluon densities

2.3.2 Parametrizations of the parton distribution functions for real photons.

In order to calculate the photon pdfs at all scales Q^2, one needs to choose a reference scale Q_0^2 and use some Ansatz for parametrizing the pdfs at this scale. Usually a vector meson dominance (VMD) Ansatz is used for $q_i^\gamma(x_\gamma, Q_0^2)$. Then fits to the F_2^γ data are used to fix free parameters. Since F_2^γ is a sum of the quark/antiquark distributions weighted with the squared charges (see 2.15), the quark/antiquark distributions can be well determined using this method. Fixing the gluon distributions is not so easy and dependent on the Ansatz used for the initial pdfs. In lack of a momentum sum rule as for the proton, the gluon distributions cannot be directly related to the quark ones.

We know that for $Q_0^2 \geq 1$ GeV^2, a pure VMD input is insufficient for fitting the data at higher scales. Usually two methods are used to solve this insufficiency:

1. Pure VMD valence like input distributions are used and a very low scale is chosen $Q_0^2 < 1$ GeV^2 for starting the evolution (for the VMD, the valence quark distributions of the pion are used). At such a low scale the input distributions should require only a VMD component and the anomalous component can be generated dynamically from the evolution equations. The problem with this method is that we do not know whether pQCD still works at such small scales.

2. A VMD + anomalous input is used selecting a starting scale $Q_0^2 \geq 1$ GeV^2. The quark densities are fitted to the F_2^γ. A guess must be made about the gluon densities.

Different parametrizations in leading (LO) and next-to-leading order (NLO) of the quark and gluon distributions are shown in figure 2.6. More about parametrizations can be found in: SaS1D/SaS2D - [Sj95], GRV - [Gl92], GS - [Go92], AFG (NLO) - [Au94]. The (simplified) main characteristics of the LO parametrizations are summarized in the following table.

LO parametrization	Q_0^2 (GeV^2)	input	factorization scheme
GRV	0.25	purely VMD	DIS_γ
SaS1D	0.36	purely VMD	DIS_γ
GS	3.0	VMD + perturbative	$\overline{MS}$
SaS2D	4.0	VMD + perturbative	DIS_γ

The ”D” of SaS1D and SaS2D parametrizations refers to the factorization scheme used - DIS_γ.

2.3.3 Parametrizations of the parton distribution functions for virtual photons.

Also for virtual photons different ansätze are used for parametrizing the pdfs. The hadronic (non-perturbative) VMD component is generally expected to diminish as

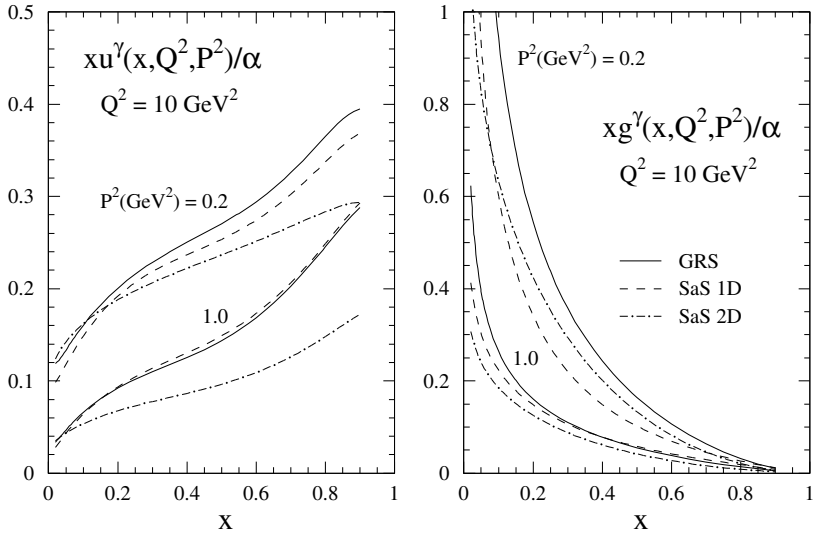

Figure 2.7 - Different parametrizations of the virtual photon pfd's: quarks (left plot) and gluons (right plot) at $Q^2 = 10$ GeV^2 for two different values of P^2: $P^2 = 0.2$ GeV^2 and $P^2 = 1.$ GeV^2

the virtuality (P^2) of the photon increases. Here we will explain the Ansatz used by Schuler and Sjöstrand for the pdfs of virtual photons.

For the real photon, Schuler and Sjöstrand see the pdfs as decomposed in a VMD and an anomalous component:

$$f_i^{\gamma}(x, Q^2) = \sum_{V}^{\rho^0,\omega,\phi,J/\psi} \frac{4\pi\alpha}{f_V^2} \cdot f_i^{\gamma,V}(x, Q^2, Q_0^2) \; + \; \int_{Q_0^2}^{Q^2} \frac{dk^2}{k^2} \frac{\alpha}{2\pi} \sum_{q} 2e_q \cdot f_i^{\gamma,q\bar{q}}(x, Q^2, k^2) \tag{2.24}$$

The VMD distributions and the anomalous distributions are parametrized separately and added to give the full result. The transition region from real to virtual photons is described introducing a dipole dampening factor for each component separately:

VMD	$1/(1 + P^2/m_V^2)^2$
anomalous	$1/(1 + P^2/k^2)^2$

Additionally the lower input scale for the VMD states is shifted from Q_0^2 to $P_0^2 \approx max(P^2, Q_0^2)$.

The resulting quark and gluon densities for the SaS1D, SaS2D (and GRS which we

did not discuss here) are shown in figure 2.7 for two different values of the virtuality P^2.

A lot of measurements performed in e^+e^- experiments have helped to constrain the pdfs of the real photons by using fits to the data. Contrary to this, few experimental data exist from e^+e^- experiments to constrain the pdfs of the virtual photons. These comes mainly from the fact that double-tagged events have a very poor statistics. As we shall see in the next sections, HERA is in a better position of studying the structure of virtual photons.

2.4 Photon Structure at HERA

At HERA, protons collide with electrons (positrons). The high flux of almost on-shell photons which accompany the electron (positron) beam provides a unique opportunity to study the nature of the photon and its interactions.

2.4.1 Dijet Production in γP Interactions

The photon may interact directly with a parton from the proton or it may first fluctuate into a hadronic state. In direct interactions the photon takes part as a whole in the interaction, therefore the fraction of photon's momentum entering the hard scattering is one ($x_\gamma = 1$). In the case of as resolved interactions the photon acts as a source of partons which scatter off the partons from the proton. The quantity x_γ is now less than unity since only a fraction of the photon's momentum enters into the hard interaction. An example of two leading order pQCD diagrams of these interactions are shown in figure 2.8.

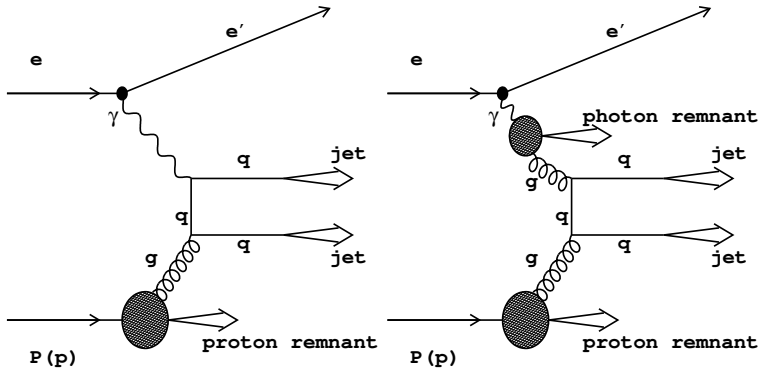

Figure 2.8 - Two example leading order diagrams for direct (left) and resolved (right) photoproduction at HERA. Note the presence of the photon remnant in the case of resolved interactions.

In both cases the final state consists of two (or more) hadron jets, the proton remnant and the scattered electron. In the case of resolved interactions, in addition to the above, the final state includes also the photon remnant produced by the spectator partons in the photon which do not contribute to the hard interaction. The photon remnant is moving in the direction of the incoming photon. The LO graphs for the direct and resolved interactions at HERA are shown in figure 2.9.

The two hard (i.e. large transverse energy) jets in the final state are related to the underlying parton dynamics. They can be used to measure the structure of the proton and the photon. Experimentally x_γ cannot be measured directly. In order to separate the resolved and direct interactions, the following observable is defined:

$$x_\gamma^{OBS} = \sum_{jets} \frac{E_T^{jet} \cdot e^{-\eta^{jet}}}{2yE_e} \tag{2.25}$$

E_T^{jet} is the transverse energy of the jet and η^{jet} is the pseudorapidity defined as:

$$\eta^{jet} = -\ln\left[\tan\left(\frac{\theta^{jet}}{2}\right)\right] \tag{2.26}$$

The sum in 2.25 runs over the two highest transverse energy jets

In the formulas (2.25,2.26) the positive z-direction is in the direction of the incoming protons. θ^{jet} is the polar angle of the jet with respect to the positive z-direction (for a more detailled definition of this angle see section on jets). Bearing in mind the correlation of the jets with the underlying partons, at LO the quantity x_γ^{OBS} is the fraction of the photon's momentum entering the hard interaction.

In figure 2.10 the variable x_γ^{OBS} is plotted. The solid line is the Herwig5.9 MC and the shaded area is the direct-only part from the simulation. One can see that a rather clean separation between the resolved and direct classes of events can be done by cutting at $x_\gamma^{OBS} = 0.75$.

At HERA there is only one photon as opposed to two photons in the case of e^+e^- experiments. By Q^2 here one denotes the virtuality of the (target) photon[3].

For high enough virtualities of the photon, the photon structure should be completely suppressed and the photon will act as a pointlike particle which probes the proton. But at smaller virtualities the photon itself will show a structure.

At HERA the photon structure is probed by a parton from the proton, i.e. by a strongly interacting object. Both quarks and gluons contribute to the interactions in ep collisions (in e^+e^- gluons do not contribute at leading order). Therefore, at HERA we are sensitive to the gluon content of the photon. Due to the absence of a simple momentum sum rule, the gluon densities cannot be extracted from the F_2^γ measurements. In jet photoproduction there is a direct sensitivity to the gluon density in the photon. This sensitivity is concentrated in the low x_γ (x_γ^{OBS}) region.

HERA is in a unique position of studying the virtual photons and the photon structure as the virtuality of the photon increases. As we have already described, such

[3]As a reminder: in e^+e^- experiments the virtuality of the target photon was denoted by P^2.

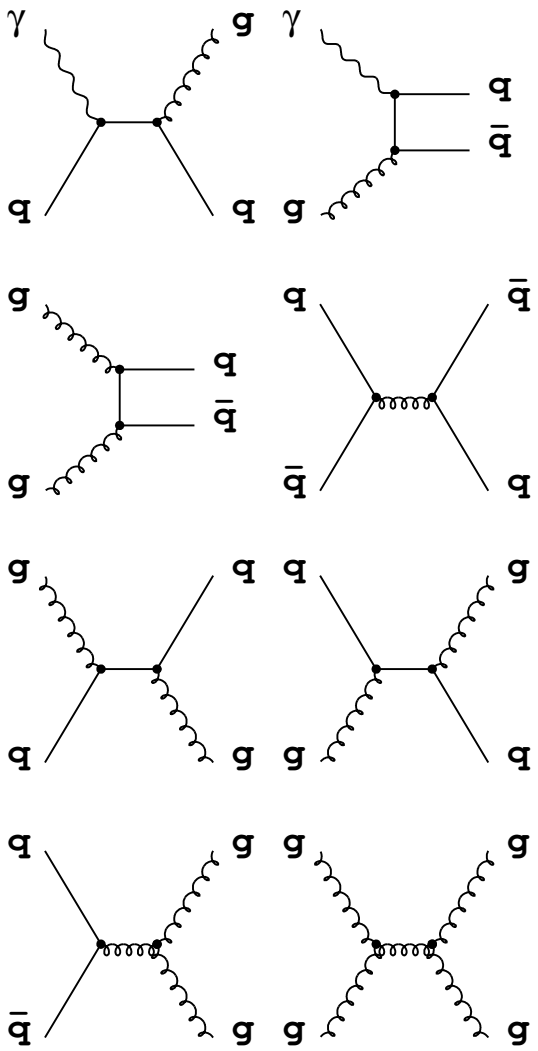

Figure 2.9 - LO graphs for direct and resolved photon interactions. The two graphs of the first (top) row: QCD Compton scattering and Boson-Gluon Fusion are the two (LO) direct photon interactions. The other graphs represent the 6 possible (LO) resolved photon interactions.

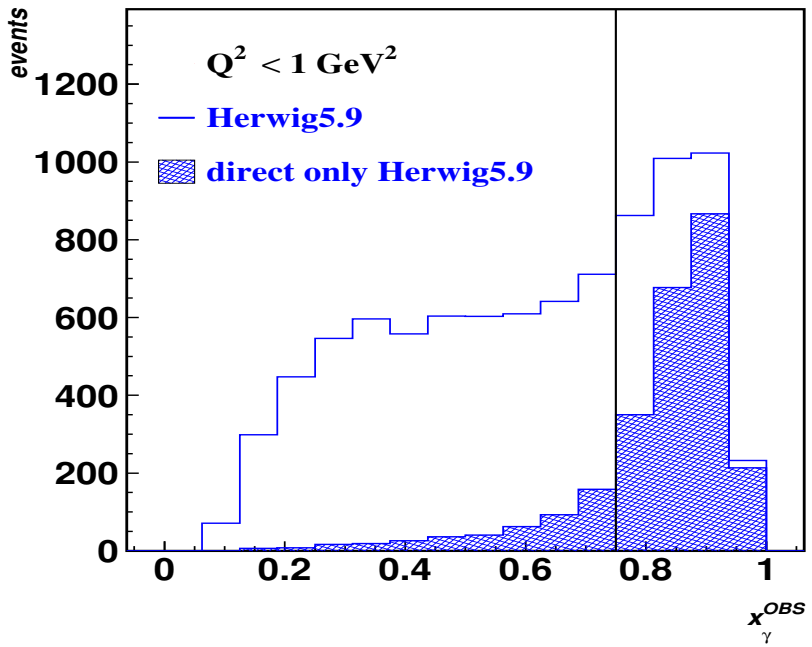

Figure 2.10 - The x_γ^{OBS} variable for dijet photoproduction events at HERA. The solid line is the Herwig5.9 simulation and the shaded area is the direct-only part from the simulation. The direct part is concentrated at higher x_γ^{OBS} and the resolved part at lower x_γ^{OBS}. One can see that a rather clean separation of the resolved and direct events can be done by a cut on $x_\gamma^{OBS} = 0.75$.

measurements in e^+e^- are difficult and suffer from poor statistics. Moreover, the photon can be probed at higher scales than in the e^+e^- experiments due to the high center-of-mass energy at HERA.

General descriptions on the photon structure at HERA can be found in [Ab98], [Ca95], and [Bu95].

The ZEUS and H1 collaborations have studied the structure of real and virtual photons. More on these studies can be found in [H1r], [H1v], [ZEr], [ZEv].

2.4.2 The two Scale Problem

In the case of $\gamma^{(*)}P$ interactions we must take into account two hard scales: the virtuality of the photon (Q^2) and the scale of the hard scattering leading to the production of jets. This second hard scale can be evaluated by the transverse energy of the jets (E_T^2).

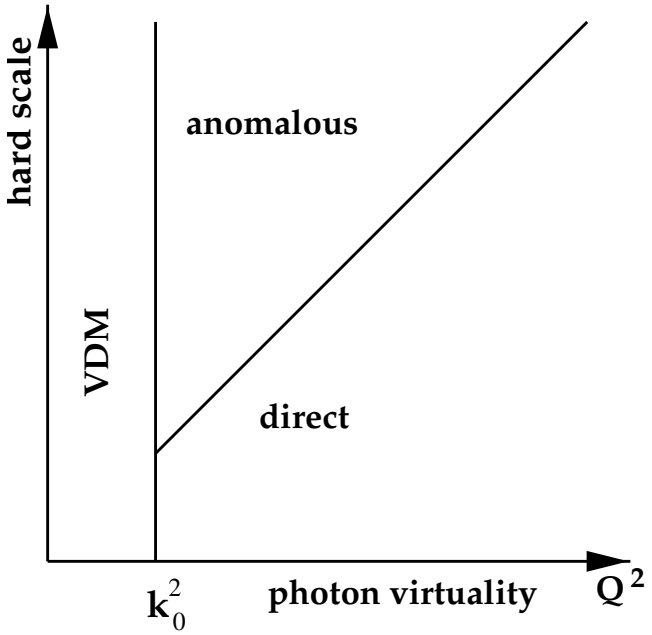

Figure 2.11 - Photon structure seen in the phase space of the two scales at HERA. In the picture also the line is drawn where E_T^2 = photon virtuality. In reality the transitions between the different regions are smooth and there are no sharp limits between them.

If the virtuality of the photon is smaller than a certain scale k_0^2, then the photon can be seen as a hadron and (as we have seen above) a VMD description of it is appropriate. The $\gamma^{(*)}P$ interaction can be seen as an VP interaction of the vector meson V with the proton P. At higher Q^2, if the photon virtuality Q^2 is smaller than the scale E_T^2, the photon will still develop a partonic structure [Fi93] coming from the anomalous photon structure. If the virtuality of the photon is larger than k_0^2 and larger than the other hard scale (E_T^2), than the photon cannot be resolved and will act as a pointlike particle. In reality there is no clear cut between the VMD-direct and direct-anomalous and the transitions between the different classes of interactions are smooth. A schematic view in the phase space of the two hard scales is given in figure 2.11. The anomalous and the VMD classes together form the class of resolved photon interactions.

2.4.3 Dijet Cross Sections - The Flux of Real and Virtual Photons

The ep interaction can be seen as two subsequent processes: emission of a photon by the electron and photon-proton interaction. If one denotes by μ the hard scale of the interaction, then according to the factorization theorem, the ep dijet cross section at HERA can be written as:

$$d\sigma(ep \to 2J + e + X) = \left[f_{i/\gamma}(x_\gamma, \mu) \otimes M_{i,j}(\mu, \hat{s}) \otimes f_{j/p}(x_p, \mu) \right] \cdot f_{\gamma/e}(y, Q^2) \quad (2.27)$$

$\hat{s}$ is the c.m. energy of the particles i, j. $f_{i/\gamma}$ is the density of the parton (quark, gluon, photon) i in the photon. $f_{j/p}(x_p, \mu)$ is the density of the parton j in the proton. $M_{i,j}$ is the cross section for the $2 \to 2$ parton-parton hard scattering. $f_{\gamma/e}(y, Q^2)$ is the flux of photons from the electron.

The flux of the (almost) real photons from unpolarized electrons (positrons) is given by the *Weizsäcker Williams Approximation* (or EPA - *Equivalent Photon Approximation*) [We34]. According to this approximation, the probability that an electron radiates a photon with given virtuality Q^2 and fractional energy z (in the rest frame of the proton this is the same as the inelasticity y) is given as:

$$f_{\gamma/e}(z, Q^2) = \frac{\alpha}{2\pi Q^2} \left[\frac{1 + (1-z)^2}{z} - 2\frac{1-z}{z} \cdot \frac{Q^2_{min}}{Q^2} \right] \quad (2.28)$$

where Q^2_{min} is the lowest virtuality that can be obtained. This lowest virtuality is determined from the mass of the electron m_e:

$$Q^2_{min} = m_e^2 \frac{z^2}{1-z} \quad (2.29)$$

For photoproduction events (quasi-real photons) the photon spectrum can be derived by integrating the EPA from Q^2_{min} to Q^2_{max}, where Q^2_{max} is the maximal value of the photon virtuality achievable:

$$f_{\gamma/e}(z) = \frac{\alpha}{2\pi} \left[\frac{1 + (1-z)^2}{z} \cdot \ln \frac{Q^2_{max}}{Q^2_{min}} - 2\frac{1-z}{z} \cdot \left(1 - \frac{Q^2_{min}}{Q^2_{max}} \right) \right] \quad (2.30)$$

The above formula gives a typical soft Bremsstrahlung spectrum.

The flux of the transversely polarized virtual photons emitted from the electron is [Ha84]:

$$f^T_{\gamma^*/e}(y, Q^2) = \frac{\alpha}{2\pi Q^2} \left[\frac{1 + (1-y)^2}{y} - 2\frac{1-y}{y} \cdot \frac{Q^2_{min}}{Q^2} \right] \quad (2.31)$$

and for longitudinal virtual photons:

$$f^L_{\gamma^*/e}(y, Q^2) = \frac{\alpha}{2\pi Q^2} \left[2\frac{1-y}{y} \right] \quad (2.32)$$

The above flux of longitudinally polarized photons is expected to be small.

2.5 Electromagnetic Photon Structure

The electromagnetic (or QED) photon structure is related to lepton pair production in the $\gamma^*\gamma$ scattering. The investigation of the QED photon structure is of interest because of two reasons [Ni00]:

1. it is a test of QED of the order $O(\alpha^4)$.
2. these measurements done in a clean experimental situation are used to refine the experimentalist's tools and investigate the possibilities of extracting similar information in the case of a much more complex hadronic final state.

In contrast to the hadronic structure functions discussed above, the QED structure functions $F_2^{\gamma(QED)}$, $F_1^{\gamma(QED)}$, $F_L^{\gamma(QED)}$ can be calculated in QED and all the particles in the final state can, in principle, be observed. The structure function $F_L^{\gamma(QED)}$ is, similarly to F_L^γ, negligible because of the factor y^2 in its contribution to the cross-section. Only a muonic final state allows for the extraction of the structure functions from the data. In the case of muons, the invariant mass of the $\mu^+\mu^-$ pair can be determined accurately, and hence x_{BJ}.

A summary of the $F_2^{\gamma(QED)}$ measurements can be seen in figure 2.12. These measurements are another proof of the correctness of QED.

A more detailed description of the electromagnetic structure functions can be found in [Ni00] and [Kr00].

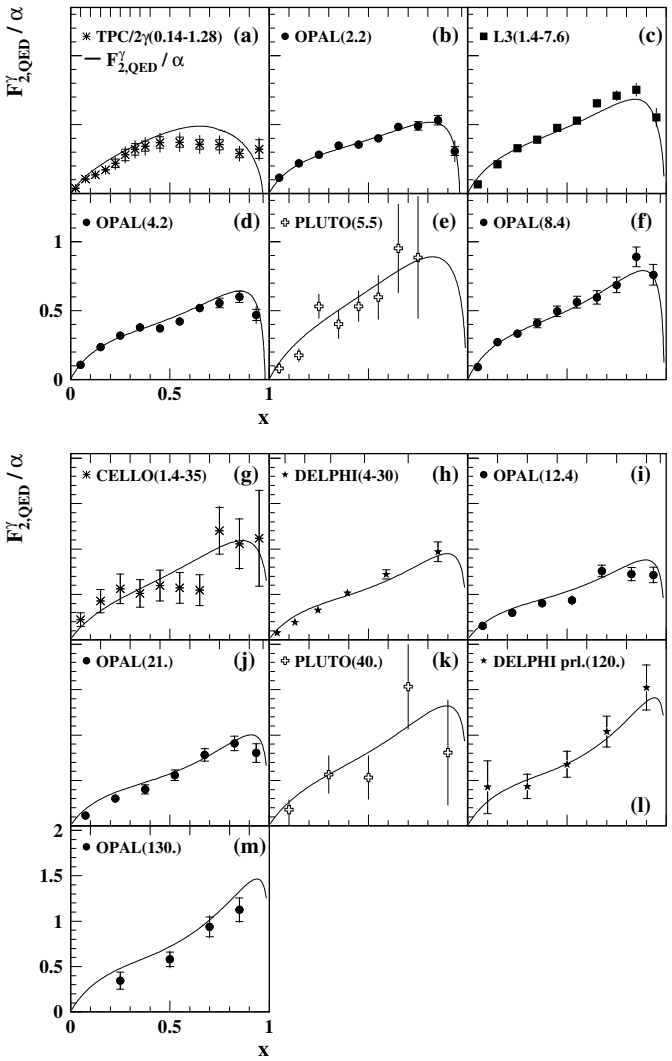

Figure 2.12 - Summary of $F_2^{\gamma(QED)}$ measurements. The errors plotted are only statistical. The structure function $F_2^{\gamma(QED)}$ is plotted versus x_{γ}^{OBS} in different bins of the photon virtuality (given in brackets in each region). [Ni00]

Chapter 3

HERA and ZEUS

3.1 The Hadron Electron Ring Accelerator

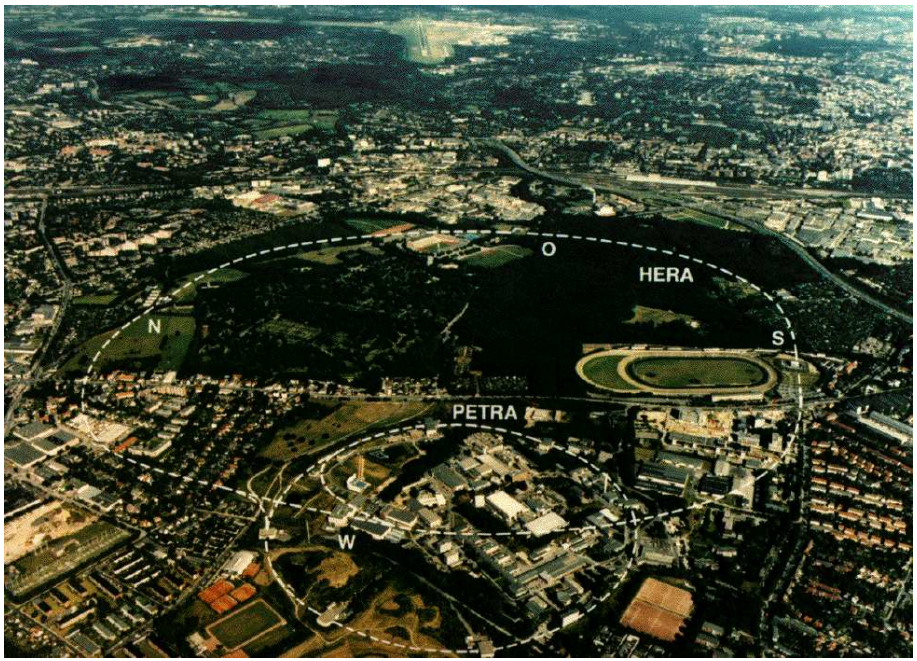

Figure 3.1 - Aerial view of DESY and surroundings together with the two largest accelerators HERA and PETRA.

The Hadron Electron Ring Anlage (HERA) is a lepton proton collider located at DESY in Hamburg, Germany. It offers unique opportunities to explore the ep interactions as the only ep collider in the world. HERA was built during the late 80's and

Figure 3.2 - The HERA accelerator and its pre-accelerator complex.

the first collisions were observed in 1991, while the operations for physics started in 1992. At HERA protons with an energy of 820 GeV [1] collide with electrons [2] of 27.5 GeV, yielding a center-of-mass energy of $\sqrt{s} \simeq 300$ GeV. HERA consists of two separate storage rings for electrons and protons. Both rings are placed in a tunnel of 6.3 km circumference, 10-30 m underground. Each storage ring consists of four 90° arcs connected by 360 m long straight sections. Superconducting magnets are used for the proton storage ring.

The HERA beams collide head-on (almost zero crossing angle) in two interaction regions occupied by the ZEUS and H1 experiments in the middle of two of the straight sections (south and north experimental hall respectively). Two fixed target experiments, HERMES and HERA-B, are situated in the middle of the two other straight sections (east and west south hall respectively).

HERMES [HE93] is investigating the spin structure of the nucleon using the scattering of longitudinally polarized photons off polarized gas targets.

HERA-B [HB94] aims to study the $\mathcal{CP}$-violation in the $B^0\overline{B^0}$-system. A wire target is used to produce B-mesons in the proton beam halo.

An aerial view of DESY and the surroundings together with the two largest accelerators HERA and PETRA is shown in 3.1. Several HERA design parameters and the corresponding machine performance during 1997 are given in table 3.1.

Hydrogen ions serve as the proton source. In the first acceleration step electrons and protons are accelerated using linear accelerators ('Electronen-Linac', 'Positronen-Linac', 'H^--Linac'). Electrons are accumulated in the small storage ring PIA (Positron-Intensity-Accumulator) between the Linac and DESY II until sufficient intensity is reached. The particles are then injected into DESY II (electrons) and DESY III (protons). After injection into PETRA and further acceleration electrons and protons are injected into HERA. Figure 3.2 shows schematically the layout of the HERA accelerator complex.

[1] In the 1998/1999 running period the proton energy was increased to 920 GeV

[2] HERA has run both with positrons and electrons in the different running periods. The term electron is here generically used for both electrons and positrons.

HERA parameters	Design Values		Values of 1997	
	$e^{\pm}$	p	e^+	p
Circumference (m)	6336			
Energy (GeV)	30	820	27.6	821.2
Center-of-mass energy (GeV)	314		301	
Injection energy (GeV)	14	40	12	40
Current (mA)	58	160	36	78
Magnetic field (T)	0.165	4.65	0.165	4.65
Number of bunches	210	210	174+15	174+6
Bunch crossing time (ns)	96			
Horizontal beam size (mm)	0.301	0.276	0.200	0.200
Vertical beam size (mm)	0.067	0.087	0.054	0.054
Longitudinal beam size (mm)	0.8	11	0.8	11
Specific luminosity ($cm^{-2}s^{-1}mA^{-2}$)	$3.6 \cdot 10^{29}$		$5.0 \cdot 10^{29}$	
Instantaneous luminosity ($cm^{-2}s^{-1}$)	$1.6 \cdot 10^{31}$		$1.45 \cdot 10^{31}$	
Integrated luminosity per year (pb^{-1}/a)	35		36.5	

Table 3.1 - HERA parameters. In 1997 HERA operated with 174 colliding bunches, 15 positron-pilot bunches and 6 proton-pilot bunches.

3.2 The General Purpose ZEUS Detector

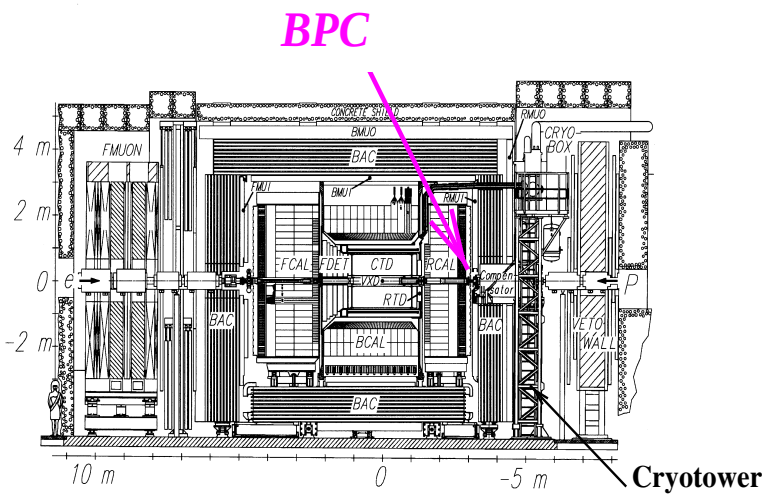

Figure 3.3 - CAD drawing of the ZEUS detector in the Y-Z plane. The arrow points to the position of the BPC and BPT inside ZEUS.

The ZEUS detector is a general purpose, almost hermetic, magnetic detector, de-

signed to study ep scattering. The tracking detectors surround the interaction point tracing the charged particles bend from magnetic fields. In the outer layers, the energy of charged and neutral particles is measured by measuring the total energy they deposit. The detector is almost hermetic, it covers nearly the entire 4π solid angle, allowing only for small apertures for the beam pipe. The ZEUS detector characterizes the ep final state in terms of energy, direction, and type of particle produced.

ZEUS has a Cartesian right-handed coordinate system with origin $((X, Y, Z) = (0, 0, 0))$ at the nominal interaction point (IP). The Z-axis is defined by the incoming proton beam direction, the X-axis points towards the center of the HERA ring, the Y-axis points vertically upwards. With this definition of the axes, the incoming electrons move in the direction of $-Z$.

The main detector is shown in figure 3.3 and 3.4 along and perpendicular to the beam direction, respectively. The design takes into account the forward-backward assymetry of the ep final state resulting from the large difference of the momenta (energies) of the incoming protons and electrons. The center-of-mass system is moving (is boosted) in the laboratory frame in the direction of the proton beam.

Figure 3.4 - CAD drawing of the ZEUS detector in the X-Y plane (perpendicular to the beams).

The figure 3.5 shows the luminosity delivered by HERA (left plot) and the one collected with ZEUS (right plot) for the years 1994-2000. The performance improvement of both HERA and ZEUS is seen.

In the remaining part of this section an overview will be given of the major dector

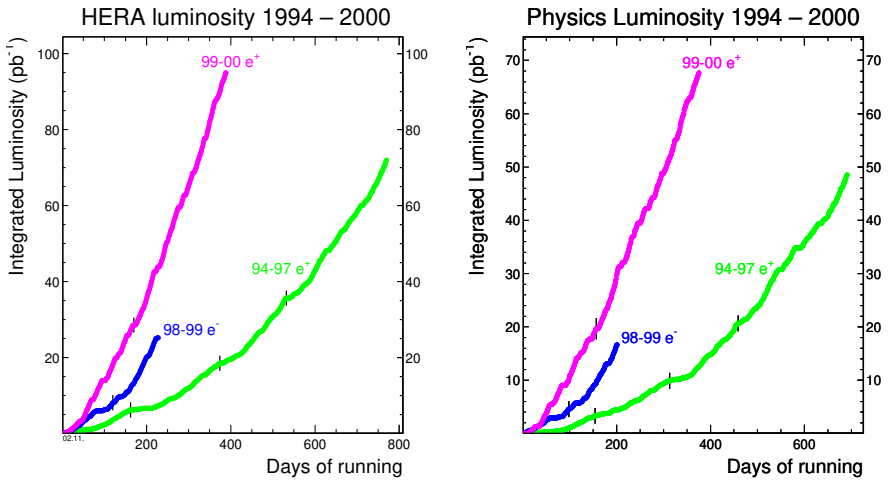

Figure 3.5 - Integrated luminosity delivered by HERA in the different running periods (left plot) and the one taken with the ZEUS detector (right plot) that is used for physics analysis.

components relevant to the analysis.

3.2.1 The Central Tracking Detector

The main ZEUS tracking device is the *Central Tracking Detector* (CTD) [Fo93]. It is used to measure precisely the direction and the (transverse) momentum of the particles as well as the vertex (the coordinates of the interaction point - IP) of the event.

The CTD is a cylindrical multi-cell stereo superlayer wire chamber. It is subdivided into 8 sections and has 72 layers, organized in 9 superlayers. The CTD consists of 576 cells with eight sense wires per cell and a total of 24192 field wires. There are 32 cells in the innermost superlayer and 96 in the outermost one. The inner radius of the CTD is 18.2 cm and the outer radius 79.4 cm. The active volume has a length in Z of 205 cm and the polar angle coverage is $15° < \theta < 164°$, corresponding in pseudorapidity to $2.04 > \eta > -1.96$ [3]. Of the 9 superlayers 5 (the odd-numbered axial layers) have their sense wires parallel to the Z-axis and the other four have sense wires rotated by a $\simeq \pm 5°$ stereo angle, providing information on the z position of the tracks. The electronics of the wires in the superlayers 1, 3, and 5 makes possible to determine the Z vertex (interaction point) coordinate by measuring the time arrival of the signals at the ends of the wires. One of the CTD octants with the

[3] The pseudorapidity is defined as a function of the angle θ: $\eta = -\ln\left[\tan\left(\frac{\theta}{2}\right)\right]$

superlayers and their angles is shown in figure 3.6.

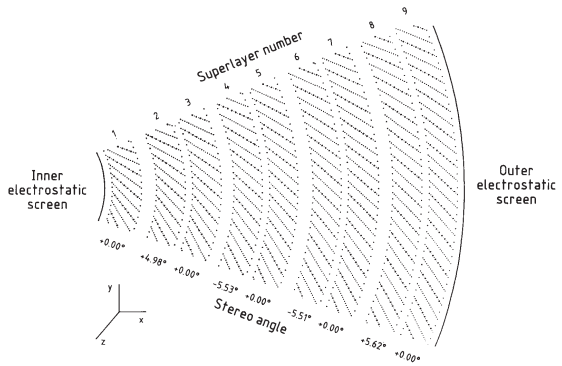

Figure 3.6 - Schematic diagram of one octant of the CTD with the 9 superlayers.

The CTD is filled with a mixture of argon, CO_2, and ethane. Particle identification is done through measurements of the mean energy loss dE/dx of charged particles within the CTD. The spatial resolution of CTD in the $r-\phi$ plane is 190 μm and in the Z direction about 1 mm. The momentum resolution is $\sigma(p_t)/p_t = 0.005 \cdot p_t/(\mathrm{GeV/c}) \oplus 0.0016$. The event interaction point is measured with a resolution of 0.4 cm in the Z direction and 0.1 cm in the X and Y directions.

3.2.2 The Uranium-Scintillator Calorimeter

The ZEUS uranium-scintillator calorimeter (UCAL) is a high resolution compensating uranium scintillator sandwich calorimeter. The depleted uranium plates of 3.3 mm thickness enclosed in thin stainless sheets serve as the absorber. The plastic scintillator (SCSN38) plates have a thickness of 2.6 mm. They serve for detecting the signal. The widths of the absorber and scintillator are chosen such that, for a signal integration time of 100 ns, equal signal is provided for hadrons and electromagnetic particles of the same initial energy (sampling calorimeter). The natural radioactivity of the uranium (U^{238}) is used as a stable reference signal. The accuracy of the channel-to-channel calibration of the calorimeter is better than 1%. The energy resolution for electrons and hadrons is determined to be:

$$\frac{\sigma_e(E)}{E} \simeq \frac{18\%}{\sqrt{E}} \quad \leftrightarrow \frac{\sigma_h(E)}{E} \simeq \frac{35\%}{\sqrt{E}} \tag{3.1}$$

where the energy E is measured in GeV.

The UCAL is divided into three main parts (sections), the forward (FCAL), barrel (BCAL) and read calorimeter (RCAL). Each of these parts covers a different polar angle [De91]: FCAL $2.2^\circ < \theta < 39.9^\circ$, BCAL $36.7^\circ < \theta < 128.1^\circ$, and RCAL

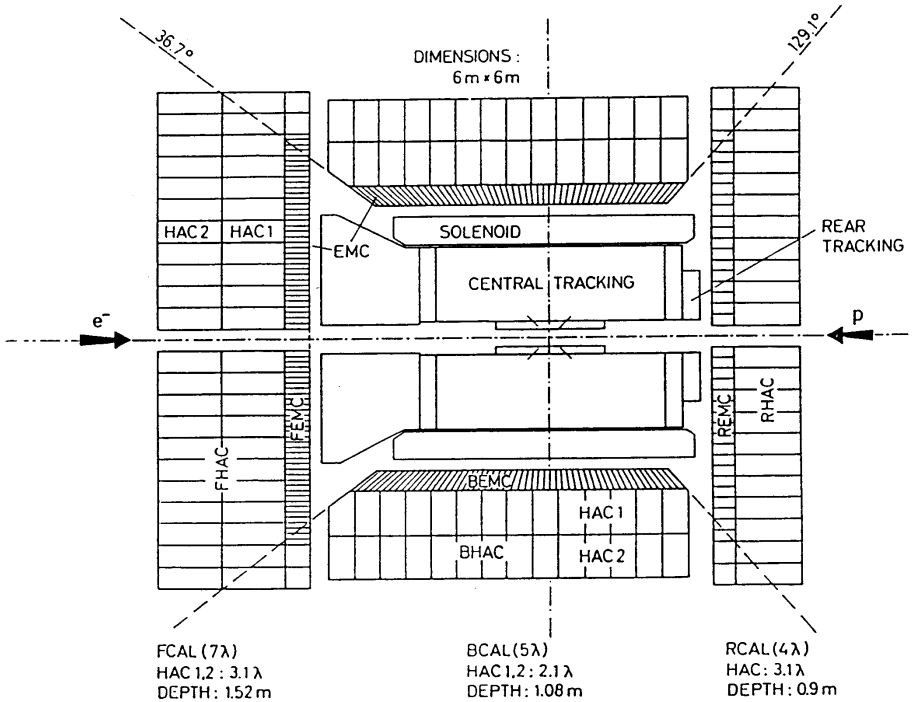

Figure 3.7 - Side view of the ZEUS calorimeter with the uranium calorimeter divided into sections, modules, towers, and cells.

$128.1^\circ < \theta < 176.5^\circ$. As a whole, UCAL covers 99.6% of the solid angle around the interaction point. The calorimeter sections are built in modules, that run vertically for FCAL and RCAL and longitudinally for BCAL. Each module is segmented into towers, that on their turn are subdivided in cells. A side view of the ZEUS detector with the calorimeter sections, modules, towers and cells can be seen in figure 3.7. There are four different types of cells: one electromagnetic (EMC) and three hadronic (HAC0, HAC1, HAC2). The first interaction length of all sections is electromagnetic (EMC) cells. The BCAL EMC cells are projective, while the cells of the other modules are not. The cells near the edges of FCAL and RCAL which are shadowed from the interaction point by BCAL EMC cells are of type HAC0. The subsequent 3 interaction lengths in FCAL and RCAL and in BCAL are cells of type HAC1 and the last 1.5-3 interaction lengths in FCAL and BCAL are HAC2. In RCAL there is only one hadronic section because the hadronic energies in the backward direction are limited. Every cell is read out by two photomultiplier tubes, coupled to the scintillators through wavelengthshifters. The photomultipliers are read out separately and this information is used for reconstructing the total energy and an approximate position of the particle. One FCAL module with the EMC and HAC

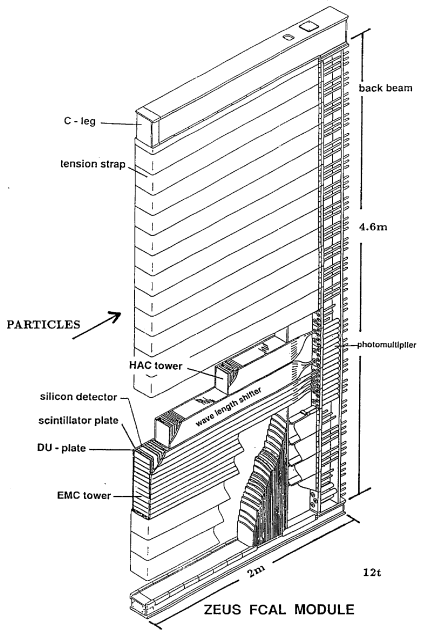

Figure 3.8 - View of a module of the FCAL with the EMC and HAC sections divided into cells.

sections and their cells is shown in 3.8.

3.3 Presampler

The presampler is used to measure on an event by event basis the energy loss of particles reaching the main calorimeter. The loss of energy is primarily caused by preshowering in the dead material.

The presampler consists of scintillator tiles mounted in front of the CAL modules which are read out with wavelength-shifters. Since 1995 the FCAL and RCAL modules are equiped with the presampler tiles. They cover a large fraction of the RCAL surface and match the HAC segmentation of 20 cm $\times$ 20 cm. A front view of the RCAL is shown in figure 3.9. The area covered by the presampler is shaded.

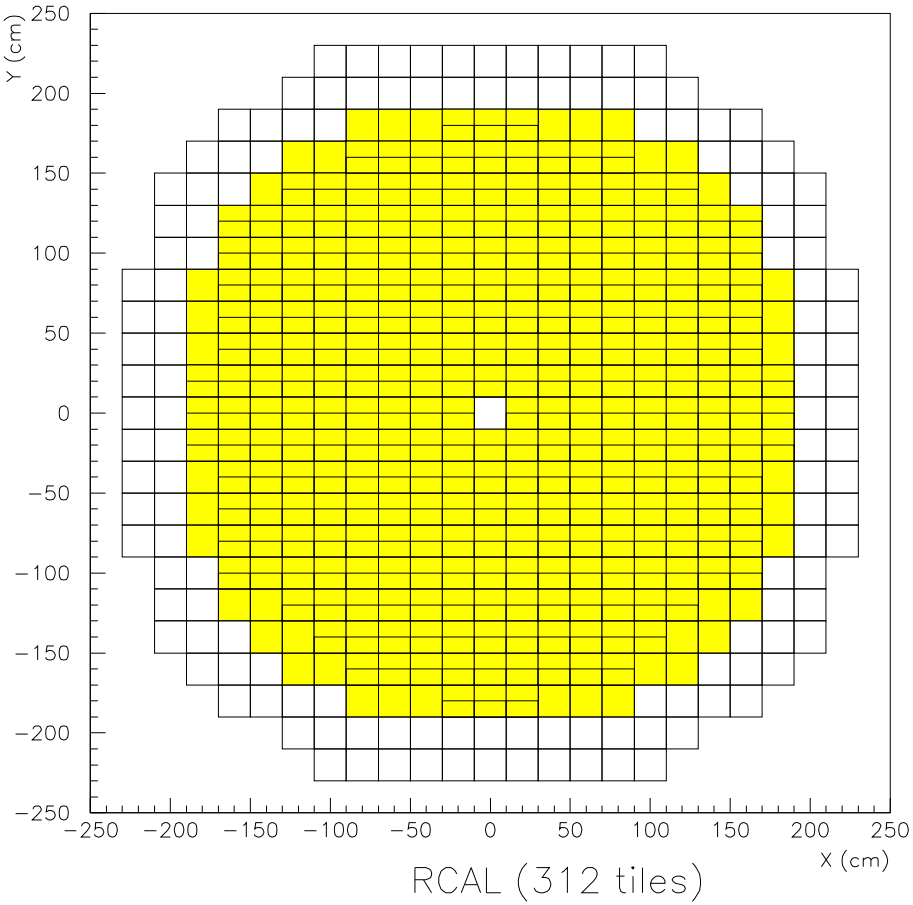

Figure 3.9 - RCAL front view. The shaded part is the area covered by the presampler.

3.4 Small Angle Rear Tracking Detector

Electrons which are scattered through small angles loose a significant amount of their energy in the dead material in front of the beam pipe. This showering makes it more difficult to use the energy measurement in the kinematic calculations. The Small Angle Rear Tracking Detector (SRTD) was built to overcome this and other difficulties. Its main benefits are [Ba95], [Ba97]:

- Recognition of preshowering electrons with the possibility to correct for energy loss in the inactive material. The amount of energy lost of the electrons is

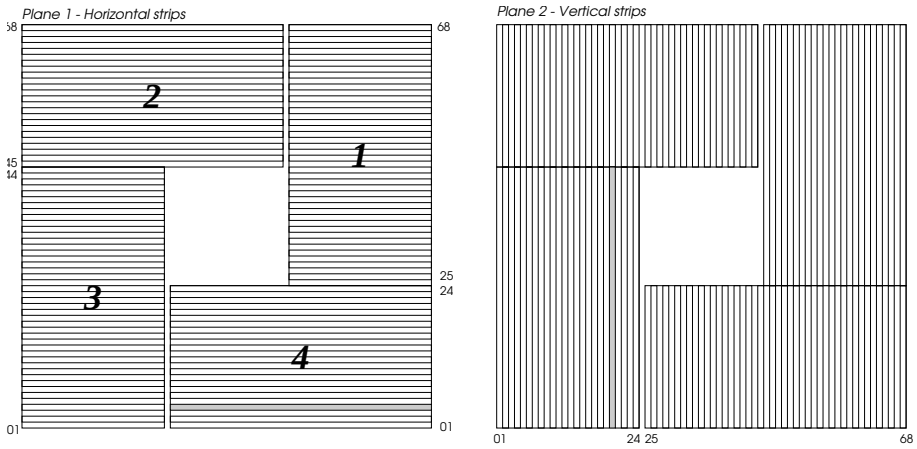

Figure 3.10 - Layout of the Small angle Rear Tracking Detector (SRTD). Orientation and numbering scheme of the strips. In 1995 the RCAL and SRTD modules above and below the beampipe hole have been moved closer together. The quadrants 2 and 4 are only separated by 8 cm.

proportional to the number of particles created in the shower. By measuring this number of particles, a correction function is derived for the energy loss. The energy correction has been determined using kinematic peak events, QED Compton and DIS ρ^0 events since in all these cases the energy of the scattered positron can be calculated without using calorimeter information.

The kinematic peak events are at low y (and low Q^2). In this region of phase space the energy transferred from the electron to the final hadronic state is low. The energy of the scattered positron becomes approximately independent of the kinematics of the event and is roughly equal to the positron beam energy.

In DIS ρ^0 and QED-Compton events the energy of the scattered positrons can be derived from constraints on the final state particles.

- Improvement of the position measurement and identification of charged particles within the SRTD acceptance. The SRTD achieves a position resolution better than $5\mathrm{mm}$ in x and y.
- Based on the timing information at the first trigger level, rejection of upstream proton beam-gas interactions is done. The SRTD provides a very accurate timing measurement with a timing resolution of 0.6 ns. Particles resulting from an upstream beam-gas interaction will arrive the SRTD simultaneously with the proton beam and leave a signal in the SRTD. Particles coming from the interaction point will need more time as the proton beam needs to travel to the interaction point and the product particles back to the STRD. The time delay of particles coming from the nominal ep interaction vertex in comparison to the particles coming from beam-gas interactions is ~ 5 ns.

The SRTD detector is installed directly in front of the RCAL at a position $z = -147.95$ cm. It consists of polystyrene scintillator strips ($5\mathrm{mm} \times 9.8\mathrm{mm} \times 240/440\mathrm{mm}$), arranged in two planes of four 24 cm $\times$ 44 cm quadrants each as shown in figure 3.10. The strips are read out by photomultiplier tubes. The angle range covered by the SRTD is $162^\circ < \vartheta < 178^\circ$. The strips are $9.8 \pm 0.05\mathrm{mm}$ wide and yield a position resolution of approximately $3\mathrm{mm}$. The position of SRTD within the ZEUS detector is shown schematically in figure 3.11

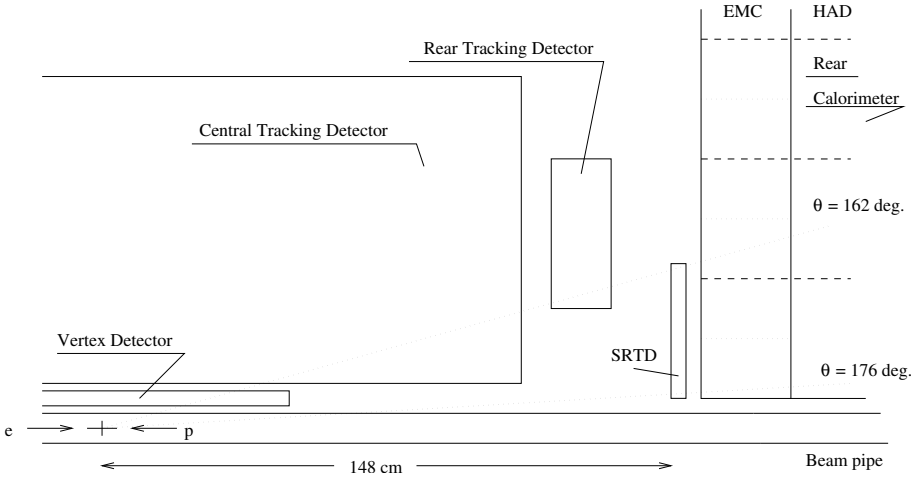

Figure 3.11 - Positioning of the SRTD inside the ZEUS detector in the zy plane. The distances are not to scale. The SRTD covers the gap between the Rear Tracking Detector (RTD) and the beam pipe.

Before the SRTD was installed, the response of each channel to minimum ionizing particles was measured using a ruthenium ($^{106}\mathrm{Ru}$) source. After installation the SRTD was calibrated with ep data. There is a 10% uncertainty on the SRTD absolute energy scale. Since the SRTD is used to make energy corrections of the order of 10%, this uncertainty results in a total 1% uncertainty of the electron energy.

3.5 The Luminosity Monitor

The precise determination of the luminosity is essential for an absolute cross section measurement. At ZEUS, the luminosity is measured from the Bethe-Heitler process $ep \to e'\gamma p$ [Be34]. The electron is scattered elastically off the proton and together with the photon leaves the interaction point through very small angles with respect to the beam axis. The rate of hard bremsstrahlung photons is measured and the well-known (up to an accuracy of 0.5%) theoretical cross section σ of this process allows to determine the ep luminosity. In a particular range of the energies, the rate $\dot{N}$ of the events is counted The integrated luminosity L is then: $L = \dot{N}/\sigma$.

Photons emitted under small angles leave the beampipe through a berillium-copper window at 82 m from the interaction point in the negative Z direction and are detected in the LUMIγ detector [An92] situated at -107 m. The LUMIγ detector is a lead-scintillator calorimeter of 22 X_0 depth. The energy resolution of the LUMIγ detector is measured under test-beam conditions to be $18\%/\sqrt{E}$. The carbon/lead filter placed in front of the detector to shield it against synchrotron radiation reduces the resolution to $23\%/\sqrt{E}$. Layers of scintillator fingers are installed within the LUMIγ detector for reconstructing the photon impact point with a resolution of 2 mm in both vertical and horizontal directions. In figure 3.12 is shown the ZEUS luminosity system and the different magnets in the negative Z direction. The electrons e' and the photons γ from the Bethe-Heitler process are also schematically shown together with the detector used for tagging the photons (LUMIγ) and the one for tagging the electrons (LUMIE). The LUMIγ detector is also used to determine the electron beam tilt and measure photons from initial state radiation (ISR). The LUMIE calorimeter has a resolution of $18\%/\sqrt{E}$ and is used to tag events in a limited kinematic range of $Q^2 < 0.01$ GeV^2 (photoproduction). The LUMIE detector is not used in this analysis.

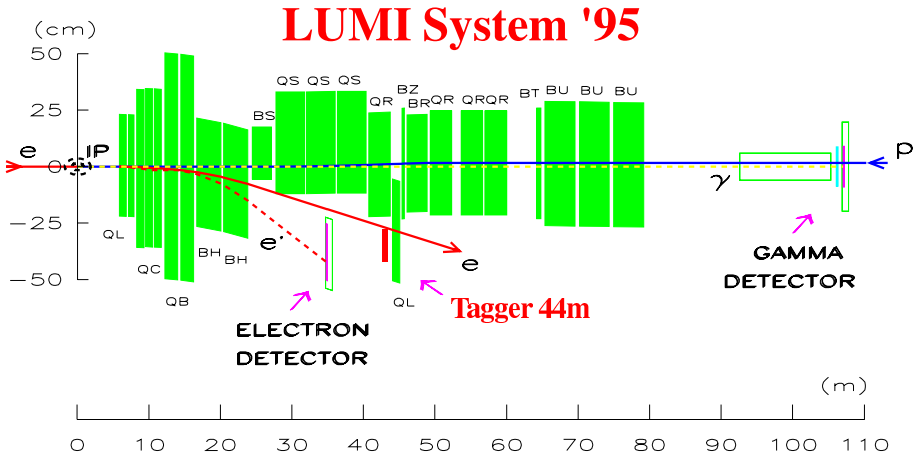

Figure 3.12 - The ZEUS luminosity system and different magnets in the negative Z direction. The bending magnets are marked with B and the quadrupole magnets with Q.

3.6 The Beam Pipe Calorimeter

The Beam Pipe Calorimeter (BPC) is a small calorimeter installed in ZEUS (spring 1995) in order to significantly enhance the phase space coverage of the ZEUS detector for very low x and low Q^2 neutral current events.

The BPC consists of two segmented tungsten-scintillator calorimeters (modules) situated at the position $Z = -293.7$ cm immediately adjactent to the beam pipe. The

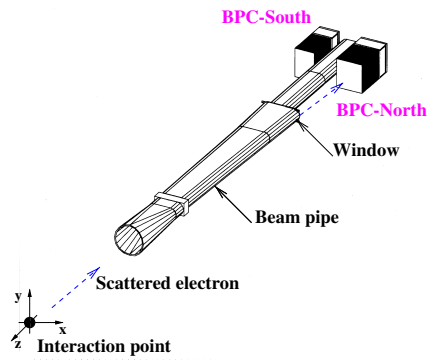

Figure 3.13 - The BPC modules and ther location with respect to the beam pipe. The position of the modified beam pipe window is also shown.

position of the BPC and BPT [4] inside the ZEUS detector is shown in figure 3.3. The two modules are labelled BPC-North (BPCN) and BPC-South (BPCS) by virtue of their position within ZEUS. A schematic of the two BPC modules and their position with respect to the beam pipe is shown in figure 3.13. The beam pipe has been modified on each side to include two exit windows for each module. The windows have a $Z = -249.8$. The exit windows consist of low-mass aluminium for allowing the electrons to reach the two BPC modules after transversing a minimal amount (0.0016 radiation length) of inactive material. The size of the two windows determines the fiducial region of the modules. The fiducial region on the BPCS is substantially smaller than the one on the BPCN.

Each of the modules consists of 26 tungsten plates of 3.55 mm thickness. The absorber tungsten plates alternate with active layers of scintillator strips of 2.6 mm width. The thin tungsten and scintillator plates ensure frequent sampling and a good energy resolution. The scintillator strips are also called scintillator fingers. The orientation of the scintillator fingers alternate from layer to layer in the horizontal and vertical direction. Each scintillator finger is finely polished and wrapped in aluminium foil, that decouples it from the neighbouring fingers and increases the light yield. Each scintillator finger is read out from one end with wave length shifter bars (WLS), that are coupled to to photomultiplier tubes. Each WLS bar is coupled to all the strips with the same X or Y. A CAD drawing of the two BPC modules with the layers of tungsten and scintillator including the wavelengthshifters and the PMT housings is shown in figure 3.14.

The BPC has (in the fiducial region) a position resolution of better than 1 mm. and an energy resolution of 15 %/$\sqrt{E}$, where the energy E is in GeV.

[4] The BPT - beam pipe tracker is a small silicon tracker on the BPC surface. It will not be described here as it is not used in the analysis.

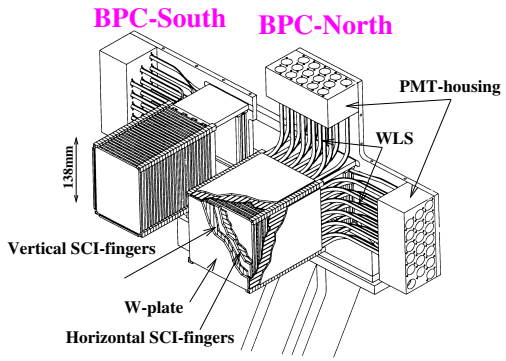

Figure 3.14 - CAD drawing of the BPC modules with details of their construction.

3.7 The ZEUS Trigger

The HERA beams cross every 96 ns corresponding to a rate of approximately 10 MHz. The total interaction rate is 10-100 kHz and is dominated by interactions of the proton beam with the beam gas. For the roughly 250000 readout channels of the ZEUS detector, the size of each event is about 0.5 MB. The writing speed of the ZEUS Data Acquisition System (DAQ) to tape is limited so only a few events per second (less than 10 Hz) can be accepted by the DAQ. It is therefore essential to reduce the rate of events by selecting the interesting physics events already at the early stages of data taking. The ZEUS three level system trigger has the task to reduce the rate to acceptable levels for the DAQ. This system has been designed to select good physics ep events and reject unwanted background events. Apart from the interactions of the proton beam with the residual gas in the beam pipe, other background sources are halo beam interactions, electron beam gas interactions, cosmic ray events, etc.

The trigger levels are the first level (FLT), second level (SLT), and third level trigger (TLT). A schematic diagram of the ZEUS trigger system and data acquisition system is given in figure 3.15. In each stage the trigger decides whether to keep or reject the event. A short description of the three trigger stages is given below.

- **FLT** - At this stage the rate is reduced to less than 1 kHz. The FLT is a hardware based trigger. Each ZEUS component has its own FLT. Every 96ns the readout of the components and their FLT systems is pipelined. The information of the component FLTs is transferred to the global first level trigger (GFLT) approximately 2 μs after the beam crossing occurred. The GFLT itself decides to pass the event to the SLT or discard it within 5 μs after each beam crossing. The GFLT decision is based on logical combinations of the component FLTs.

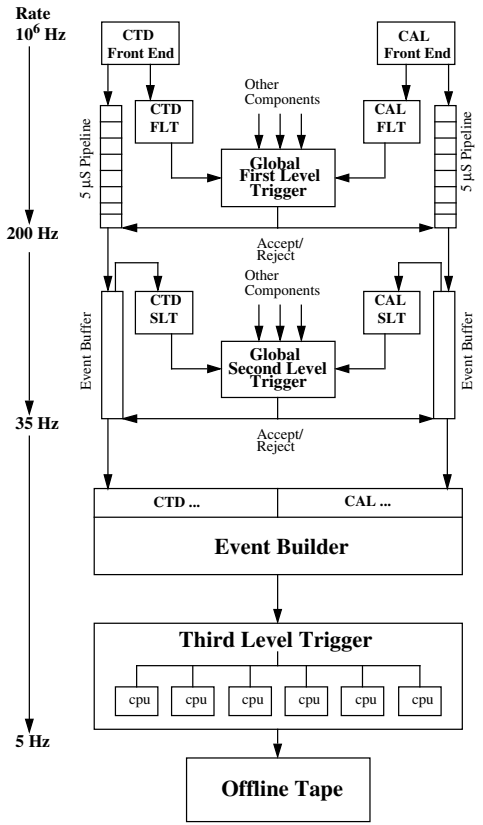

Figure 3.15 - The ZEUS trigger and data acquisition system.

The pipelining of the events to avoid dead time. If an event is accepted by the GFLT, the data stored in the pipeline is transferred to the SLT.

- **SLT** - The SLT is designed to reduce the rate to less than 100 Hz. Similarly to the FLT, each component has its own SLT, which is softare based and runs on a network of programmable transputers. The information of the component SLTs is stored in memory buffers. More sophisticated algorithms than those of the FLT are run at this level. If the event is accepted by the GSLT, the information from the components is passed to the event builder, that reconstructs the data accessible to the TLT. The event builder has access to the full event data taken by all components. It provides a picture that can be understood in terms of four

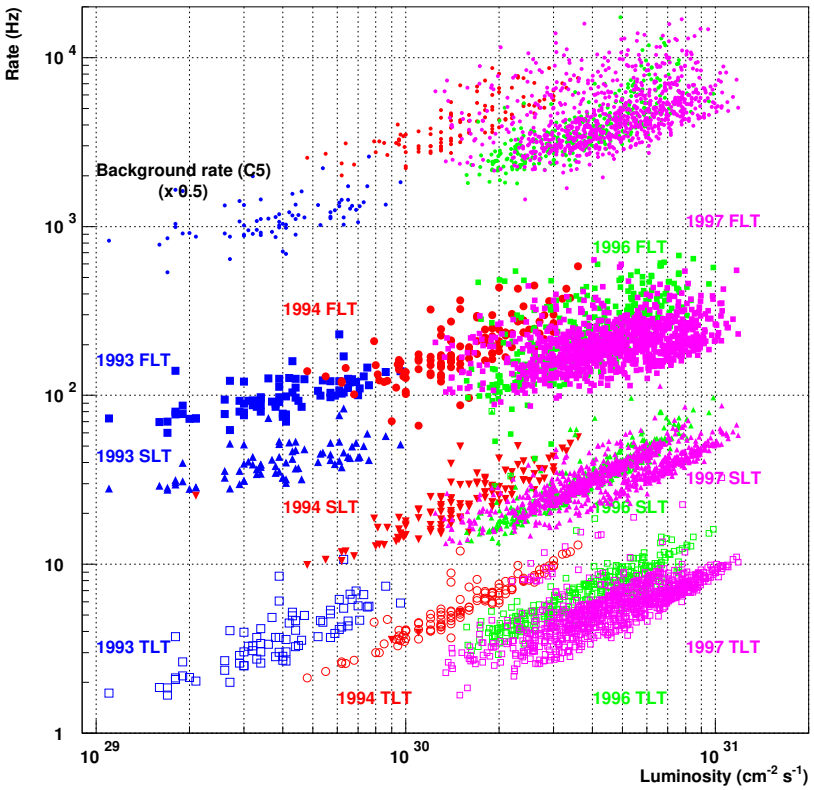

Figure 3.16 - Trigger rates of FLT, SLT, and TLT as a function of luminosity and data taking period for the years 1993-1997.

momenta of the particles.

- **TLT** The TLT has the task to reduce its input rate to an output rate of 3-5 Hz. It runs a version of the full offline analysis code on a processor farm of Silicon Graphics (SGI) workstations. Events accepted by the TLT are written to tape.

The trigger rates for the of FLT, SLT, and TLT as a function of luminosity and data taking period for the years 1993-1997 are shown in figure 3.16. As the luminosity has increased, changes have been made to the trigger system in order to keep the rate at the acceptable level of few Hz.

A complete and final reconstruction of the data is performed offline. Reconstruction and calibration routines are used offline which cannot be run at the TLT level because of the time restrictions.

Chapter 4

Jets

4.1 Jets in QCD

In high-energy-physics reactions partons (quarks and gluons) are produced in the first step as a result of the hard underlying process. Because of colour confinement it is not possible to observe quarks and gluons as final state particles of the reactions. The partons will radiate other partons (parton shower) and will finally recombine to form colour singlet states which are called hadrons. This last process is called hadronization.

The radiated partons and the subsequently created hadrons will form a collimated "stream" of particles around the direction of the original parton. This collimation of the final state particles around the direction of the initial partons has to do with the fact that the QCD radiations are of energies of the order of 1 GeV (or less) while the hard scatterings are of the order of several GeV. These collimated flows of particles are called *jets*. Jets will be correlated to the primary partons but one should not think that by measuring jets we are measuring a primary parton. The jet is merely an event property that is largely determined by the primary parton [Se95].

During a reaction, low transverse momentum particles are also generated from the extra hadronic activity in the event (not directly related to the hard scattering) and form the *soft underlying event*. The soft underlying event overlaps with the jet formed by the hard scattering. This is one of the difficulties in assigning final state jets to original partons. The hadronization effects are generally theoretically not understood and are estimated using Monte-Carlo models.

4.2 Jet Finders

A jet algorithm assigns partons or hadrons to jets and calculates the physical quantities (transverse energy, pseudorapidity, etc.) related to these new objects (jets). There are many different ways of defining jets. A jet should be well defined and easy to measure from the hadronic final state, easy to calculate order-by-order in pQCD, and be composed of objects which have a close correspondence to the initial partons. For quantitative measurements, jets are defined using jet finding algorithms which are based on the supposition that the final state particles belonging to a jet are close to each other in phase space. Different jet finding algorithms are implemented in the different jet-finders used for determining the jets.

There are two main types of jet-finders (algorithms) commonly used: the cone algorithms, used mainly in $\mathrm{p\bar{p}}$ experiments, and the clustering algorithms, used mainly in e^+e^- experiments. The cone algorithms define a direction that maximizes the energy flowing into a cone drawn around it. The clustering algorithms are based, as the name implies, on iterative clustering procedures in which particles are merged together in pseudoparticles, which are the output jets.

From the theoretical and from the experimental point of view, a jet finding algorithms should fulfil the following two requirements:

1. **collinear safe** - the jet finding should treat a collinear pair of particles identically to a single particle with their combined momentum. From the theoretical point of view this means that the jet finding is independent of a parton splitting into two parallel travelling partons. Such a dependence would cause divergencies in the theoretical calculations, which are called *collinear divergencies*. In fact these divergencies are avoided by integrating over the contributions of both.

   From the experimental point of view, such a property means that the jet finding is largely independent of the granularity of the detector. Particles which go in the same detector cell cannot be resolved anyway.

2. **infrared safe** - the jet finding should be insensitive to the emission of low energy particles. Theoretically, this property avoids the soft divergencies in perturbative calculations. Experimentally, low energy deposits are cut out from cuts to suppress the detector noise and the jet finding should be independent of this.

A schematic diagram of an analysis using jets is shown in 4.1. The jet finding can be done on: 1. detector objects (for example cells), 2. hadrons, 3. partons. The comparison with the theory should be done at parton level but, since the hadronization corrections are difficult to calculate and model dependent, the comparison in this analysis will be done at the hadron level.

4.2.1 The Snowmass Convention

Jet finding algorithms are applied to objects in the final state. These can be calorimeter cells or hadrons (partons) in the final state of Monte Carlo events. Below it is explained how one would assign these objects to a jet according to the standard convention used at present. After the jets are defined, one can calculate the transverse energy and the coordinates (angles) of the jet using the energies and coordinates (angles) of the objects which form that jet. For the jet algorithms used in this thesis quantities are calculated using the *Snowmass Convention* [Ab92]:

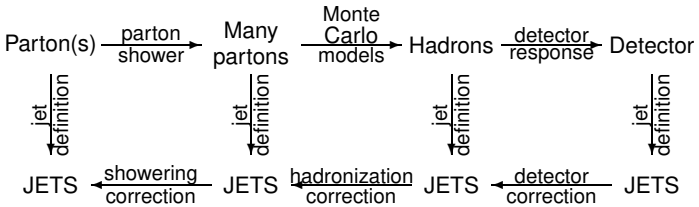

Figure 4.1 - Schematic diagram of a typical analysis using jets [Se95]. In the upper line the partons are produced from the hard scattering process and then they radiate other partons (parton shower). Colour singlet states (hadrons) are produced through the process of hadronization. The hadrons deposit energy in the detector. At each one of these stages on can do the jet finding. From the measured data in the detector one can correct backwards in principle down to the parton level.

$$\begin{aligned} E_T^{jet} &= \sum_i E_T^i \\ \eta^{jet} &= \frac{1}{E_T^{jet}} \sum_i E_T^i \cdot \eta^i \\ \phi^{jet} &= \frac{1}{E_T^{jet}} \sum_i E_T^i \cdot \phi^i \end{aligned} \tag{4.1}$$

where E_T is the transverse energy (transverse to the axis of the incoming protons), η is the pseudorapidity, related to the polar angle θ: $\eta = -\ln\left[\tan\left(\frac{\theta}{2}\right)\right]$, and ϕ is the azimuthal angle. The sums in the above expressions run over all the objects assigned to the jet.

4.2.2 Cone Algorithm

There are different cone algorithms generally used. They all associate hadrons within a cone of radius R in the $\eta - \phi$ space to the same jet. Here we discuss shortly the cone algorithm used in this analysis (EUCELL) [El92].

At the beginning clusters are determined using a grid in the $\eta - \phi$ space. All the objects with transverse energy larger than a certain value (at ZEUS this is 300 MeV) are selected as "cells" for beginning the jet finding.

A cone of radius R is then placed around the seed with highest transverse energy and all objects within this cone, that is all objects fullfilling the condition:

$$(\phi_{object} - \phi_{seed})^2 + (\eta_{object} - \eta_{seed})^2 < R^2 \tag{4.2}$$

are assigned to a jet and this jet (the objects belonging to it) is removed from further

jetfinding. This procedure is repeated until no seeds above the threshold are found. Typical values for the cone radius are $R = 1$ and $R = 0.7$.

In another version of the cone algorithm (PUCELL) the cells are not removed but other jets are found and all the found jet-centers are used as seeds until after a new iteration all objects are still assigned to the same jets.

Such an algorithm can be run with an upper pseudorapidity (η) cut on the found jets, so that very little, if any, proton remnant is included in the jets found. Cone algorithms are collinear safe but not infrared safe. Low energy radiation between the two cone jets could lead to the change of the seed position in $\eta - \phi$ and the found jets can be completely different.

The cone algorithms are usually faster to implement than clustering algorithms (for this reason, they are used at the TLT trigger stage). The main problem of cone algorithms is the overlapping problem, they are not able to clearly separate between jets which overlap. Apart from this, there is a bias coming from the choice of seeds.

4.2.3 Clustering Algorithms

The clustering jet finding algorithms have some advantages in comparison to the cone algorithms. The clustering algorithms have no overlapping problem, they unambiguously assign every object to a single jet, that is there is no seed choice dependence. In addition, for theoretical calculations the clustering algorithms are collinear and infrared safe.

Here we describe shortly the longitudinally invariant k_T - cluster algorithm [Ct93]. The k_T algorithm is applied in the following steps:

1. for every object i its distance to the beam is calculated as $d_i = E_{T_i}^2$
2. for every pair of objects the distance between them is calculated in the following way: $d_{ij} = min\left[E_{T_i}^2, E_{T_j}^2\right] \cdot \left((\eta_i - \eta_j)^2 + (\phi_i - \phi_j)^2\right)$
3. If the smallest of all the d_i and d_{ij} quantities is a d_{ij}, the objects i and j are recombined in a new object k following the p_T recombination scheme:

$$\begin{aligned} E_{T_k} &= E_{T_i} + E_{T_j} \\ \eta_k &= \frac{E_{T_i} \cdot \eta_i + E_{T_j} \cdot \eta_j}{E_{T_i} + E_{T_j}} \\ \phi_k &= \frac{E_{T_i} \cdot \phi_i + E_{T_j} \cdot \phi_j}{E_{T_i} + E_{T_j}} \end{aligned}$$

4. If the smallest of all d_i and d_{ij} quantities is a d_i the object i is defined as a protojet and is no longer merged. This protojet is removed from the further clustering.
5. the procedure is repeated for the remaining particles until none is left.

Jets are all the protojets with the transverse energy above a certain analysis defined E_T^{cut}.

4.3 Jets at HERA

At HERA, in identifying jets from the hard subprocess, it is preferable to have as little contamination as possible from remnants. The jet finders must have some feature which reduces this contamination. Another characteristic of HERA is the boost coming from the asymmetry of the momenta of the incoming particles (the proton has a much larger momentum than the photon, which gives rise to this asymmetry).

Furthermore, at higher Q^2 in the laboratory frame, the transverse energy of the jet system balances that of the scattered electron. Therefore, the jet transverse energy is not always related to the hard scale of the subprocess.

In order to avoid this the jet search in this analysis was performed with the k_T algorithm over all the calorimeter energy depositions boosted in the photon-proton hadronic center of mass frame (see section 4.3.1 below). Hence, a "decoupling" of the transverse energy and the photon virtuality is achieved. The energy depositions related to the identified scattered electron were excluded from the jet search. Obviously, the jet finding at the hadron level was also done in this frame.

4.3.1 Photon-Proton Hadronic Center of Mass Frame

For a particle (or system of particles) with four-momentum $\mathbf{p} = (\varepsilon, \vec{\mathbf{p}})$ when going from a Lorenz frame K to a new one K' the formulas of the Lorenz transformation can be written [Ha64]:

$$\begin{aligned} \vec{p}' &= \vec{p} + \vec{\beta}\gamma \left(\frac{\gamma}{\gamma + 1} \vec{\beta} \cdot \vec{p} - \varepsilon \right) \\ \varepsilon' &= \gamma(\varepsilon - \vec{\beta} \cdot \vec{p}) \end{aligned} \tag{4.3}$$

where $\mathbf{p}' = (\varepsilon', \vec{\mathbf{p}}')$ is the four vector of the particle in the new frame K'. The quantities $\vec{\beta}$ and γ can be calculated using an auxiliary particle with the boost four-vector $\mathbf{B} = (\mathbf{E}, \vec{\mathbf{P}})$:

$$\begin{aligned} \vec{\beta} &= \frac{\vec{B}}{E} \\ \gamma &= \frac{E}{M} \end{aligned} \tag{4.4}$$

where M is the mass which is obtained using the relation $M^2 = \mathbf{B}^2$. Another useful relation is:

$$\gamma = \frac{1}{\sqrt{1 - \vec{\beta}^2}} \tag{4.5}$$

The four vector $\mathbf{B}$ has to be chosen such that the new frame K' is its rest system, i.e. $\vec{B}' = 0$.

In our case the four momenta of the particles have to be boosted from the laboratory frame to the center of mass frame (rest frame) of the photon-proton (γ^*-proton) system. Therefore the boost four vector will be the four vector of the photon-proton system in the laboratory frame, which is the sum of the four vectors of the photon and the proton. The incoming proton has in the ZEUS reference frame four vector:

$$\begin{aligned} \mathbf{P} &= (E_P, \vec{P}) \\ \vec{P} &= (0, 0, E_P) \\ E_P &= 820\text{GeV} \end{aligned} \tag{4.6}$$

and the incoming electron:

$$\begin{aligned} \boldsymbol{e} &= (E_e, \vec{e}) \\ \vec{e} &= (0, 0, -E_e) \\ E_e &= 27.5\text{GeV} \end{aligned} \tag{4.7}$$

If we denote by $\boldsymbol{e}_{\mathbf{scatt}}$ the four momentum of the scattered electron, then the searched boost four momentum can be written:

$$\mathbf{B}_{\gamma^* \mathbf{p}} = -\boldsymbol{e}_{\mathbf{scatt}} + \boldsymbol{e} + \mathbf{P} \tag{4.8}$$

In order to do the boost it is obvious that one has to tag the scattered electron, i.e. measure its energy and angle for calculating its four vector (in fact, one can calculate the boost also using the JB variables, but this will be discussed later).

4.3.2 Effect of the boost on the jets

For the case of photoproduction at HERA ($Q^2 \simeq 0.$), the boost in the $\gamma^* p$ center of mass frame is simply a boost in the z-direction. This boost does not affect the transverse energy and the angle ϕ, while the pseudorapidity η changes by a constant. So in the case of photoproduction at HERA the E_T distribution in the $\eta - \phi$ space is the same in the γ^*-proton c.m. frame and in the laboratory frame. However, as the photon virtuality Q^2 increases, this nice boost-invariance changes since the photon has initial transverse momentum with respect to the z axis. In this case it is more advisable not to use the laboratory frame but the $\gamma^* p$ c.m. frame for doing the jet finding (like we do).

A typical plot for the "shift" in the pseudorapidity of the jets when the hadrons are boosted in the γ^*-proton c.m. frame is shown in figure 4.2. The plot is done for the photon virtuality range $0.1 < Q^2 < 0.55$ GeV^2 for different regions of the energy of the scattered electron. The higher the energy of the scattered electron, the more the jets are boosted in the forward direction. For the values of Q^2 in this interval the transverse energy of the jets is still not affected from the boost as the boost is still almost only longitudinal. For higher values of Q^2 also the transverse energy of the jets is affected from the boost.

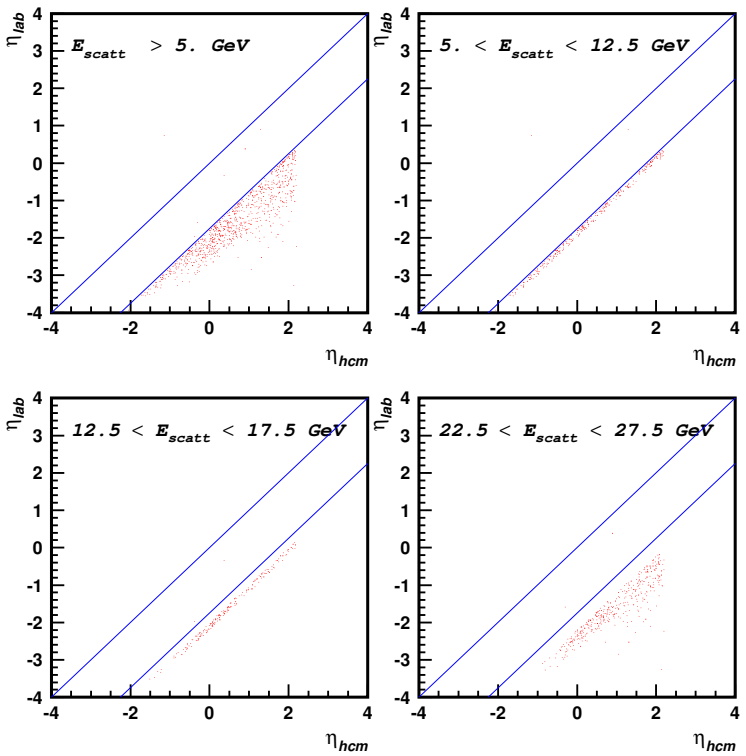

Figure 4.2 - The pseudorapidity of the jets in the lab (η_{lab}) versus the pseudorapidity of the jets in the photon-proton hadronic center of mass frame (η_{hcm}) is plotted. In the upper plot left the scattered electron energy is larger than 5 GeV, while in the other plots different intervals of the scattered electron energy are chosen. The straight lines are drawn to help see the boost and the difference in boost between the different plots. The photon virtuality region for this plot is $0.1 < Q^2 < 0.55$ GeV^2. In this region the effect of the boost on the transverse energy of the jets is negligible.

Chapter 5

Data Selection

In this chapter the selection criteria for the dijet samples are presented. The data used for the present analysis were collected with the ZEUS detector during the 1996-1997 data runs and correspond to an integrated luminosity of 38.2 pb^{-1}. During this period the experimental apparatus and the beam conditions were stable. Three dijet samples were collected by applying both online and offline cuts:

- The photoproduction sample corresponding to $Q^2 \simeq 0.$ GeV^2.
- The intermediate Q^2 sample corresponding to $0.1 < Q^2 < .55$ GeV^2.
- The deep-inelastic-scattering (DIS) sample corresponding to $1.5 < Q^2 < 10^4$ GeV^2.

The details of the selection procedure and cuts are presented in the following sections of this chapter.

5.1 Online Event Selection - Trigger Logic

The dijet samples were selected online with the ZEUS three level trigger system.

The cuts applied by the first, second and third level trigger constitute the first (online) selection. The particular trigger algorithms used here select events with at least two high transverse energy jets in the final state.

5.1.1 First Level Trigger

The First Level Trigger requires a certain minimum amount of energy to be detected in the main calorimeter (CAL) since the analysis is based heavily on usage of this calorimeter. At least one of the following conditions must be fulfilled for the event to pass the first level trigger:

- The total energy deposited in the calorimeter, excluding the three innermost rings of the the forward calorimeter (FCAL) and the innermost ring of the rear calorimeter (RCAL), should be greater than 15.0 GeV [1].
- The total calorimeter energy deposited in the EMC cells, excluding the three innermost rings of the the forward calorimeter (FCAL) and the innermost ring of the rear calorimeter (RCAL), should be greater than 10.1 GeV.
- The energy deposited in the EMC cells of the barrel calorimeter should be greater than 3.4 GeV.
- The energy deposited in the EMC cells of the RCAL, excluding its innermost ring, should be greater than 2.0 GeV.

The first level trigger uses also additional information from the C5-counter, from the SRTD, and from the Veto Wall in order to reject beam gas interactions or beam halo muons. The beam-gas interactions are rejected using the C5 counter timing if their timing is inconsistent with that of an ep interaction. This is done as follows. The signal coming from an ep interaction arrives the C5-counter after about 3 ns. If the arrival time of particles is outside a 6 ns window around this time, the event is rejected as beam gas interaction ("beam gas event"). Similarly, a cut with a $18\mathrm{ns}$ window is applied to the SRTD timing. The proton bunch will cross the Veto Wall approximately 25 ns before the nominal interaction time. Events with such a time configuration are rejected as beam-gas or beam halo muons.

5.1.2 Second Level Trigger

The Second Level Trigger has a larger latency than the first level trigger and has access to the entire calorimeter event information (pulse times of the photomultipliers or a preliminary vertex from the central tracking detector CTD). Therefore more precise selection algorithms are applied at this stage.

The following conditions have to be fulfilled for the event to be accepted by the SLT:

- At least 8 GeV of transverse energy in the calorimeter (excluding the innermost FCAL ring) are required.
- $\sum_{\mathrm{cal\ cells}} (\mathrm{E}-\mathrm{p_z})_{\mathrm{cell}} > 8.$ GeV. A z-vertex of zero is assumed for this calculation. The sum runs over all calorimeter cells. Beam gas events typically deposit energy mainly in the forward direction and will have a very low $\sum(\mathrm{E}-\mathrm{p_z})$ since the angle is very small [2].

[1] The energy measured at the trigger level is not the same as the final energy calculated offline, so these cuts are chosen as loose as possible. Of course, the trigger rates must also be within reasonable limits.

[2] At the energies we consider, the mass of the particles is much smaller than their energy. In this approximation, one can write $\mathrm{E}-\mathrm{p_z} = \mathrm{E}\cdot(1-\cos\theta)$, where θ is the azimuthal angle of the particle. For small θ $\cos\theta \simeq 1$ and $\mathrm{E}-\mathrm{p_z} \simeq 0$.

- $|z_{\mathrm{vertex}}| < 60$ cm. This cut reduces the fraction of beam gas event in the data. If no information on the CTD vertex exists, the vertex is set to zero (all three coordinates).

All the readout systems of the ZEUS sub-components are synchronized to the HERA clock. The calibration of them is such that an ep collision occuring at the ZEUS nominal interaction point results in a measured event time equal to zero. An interaction occurring outside the interaction region will produce time shifts in one direction or the other direction. Cuts are put on the times measured by different components in order to reject events coming from outside the expected interaction region. The second level trigger will reject more precisely beam-gas events and other backgrounds:

- $|\mathrm{t_{RCAL}}| < 8$ ns. The particles from a beam gas event occurring upstream (positive z-position) will reach the RCAL approximately 10 ns before a good ep event from the nominal vertex. The above requirement rejects this upstream beam gas background.
- $\mathrm{t_{FCAL}} - \mathrm{t_{RCAL}} < 8$ ns. An event coming from the nominal vertex will have a signal which will arrive approximately simultaneously to the FCAL and the RCAL. Beam gas events from upstream are rejected
- $\mathrm{t_{BCAL\ top}} - \mathrm{t_{BCAL\ bottom}} > -10$ ns. Cosmic muons leaving energy in the calorimeter and moving from top to bottom will be rejected.

5.1.3 Third Level Trigger

The time available to the third level trigger for making a decision is about $100\mathrm{ms}$. This is much longer than the respective times at the first level trigger, $5\mu\mathrm{s}$, and the second level trigger, $20\mathrm{ms}$. The full event information from the different components of the ZEUS detector is available at the third level, allowing more stringent and finer cuts to be applied. At this level a complete tracking reconstruction is performed. In comparison to the offline level the tracking is not as refined due to time limits.

A full calorimeter reconstruction is performed, bad calorimeter channels are considered, cells below certain energy threshholds (EMC: $60MeV$, HAC: $110MeV$) are set to zero.

A dijet requirement is applied at the third level trigger. Jet finding is based on a modified EUCELL jet-finding algorithm (see section 4.2.2). Events with two or more jets are selected with jet transverse energy larger than 4 GeV and pseudorapidity less than 2.5.

Additional cuts for removing the backgrounds are applied also at the third level trigger. They are based on timing requirements and on refined selection cuts:

- Beam gas interaction contaminations are further reduced by requiring the following conditions: $|\mathrm{t_{RCAL}}| < 6$ ns, $\mathrm{t_{FCAL}} - \mathrm{t_{RCAL}} < 8$ ns, $\mathrm{t_{global}} < 8$ ns. The event times are calculated using energy weighted means of calorimeter channels above the threshhold of $200MeV$.

- Cosmic muon events in FCAL and the electron-gas interactions in the beam pipe are removed by applying the cut: $t_{FCAL} < 8$ ns.
- An algorithm based on correlations between the time and the position of the energy deposits in the calorimeter is used for further cutting out the cosmic muons and beam halo muons.
- The same vertex cut is applied again ($|z_{vertex}| < 60$ cm). Since there is more tracking information than at the second level trigger, the condition is more stringent than there.
- The number of bad tracks is required to be less than 6. The bad tracks are the ones which are consistent with beam-gas interactions. They are defined as tracks which point into the forward direction but have an extrapolated vertex with coordinate: $z < -75$ cm.
- The total $E - p_z$ of the event must be less than 75 GeV : $\sum_{cal\ cells} (E - p_z)_{cell} < 75$ GeV.
  The quantity $E - p_z$ is conserved. Because of the way the ZEUS coordinate system is defined ($+z$ is the direction of the incoming protons) before the interaction this quantity will be twice the incoming electron energy: $\simeq 55$ GeV.
  Events above the cut are assumed to be overlays of two or more events.

The combination of the online selection cuts results to a loose sample of dijet events.

5.2 Offline Event Selection

Detailed calibration of the detectors, noise studies, and the full reconstruction can only be made offline and not during data taking. Therefore, the offline selection cuts are more accurate than the ones at the trigger level and will increase the purity of the sample.

Some of the offline selection cuts are specific to the samples for the different Q^2. They will be described in the section on the general selection. In the next sections details of the three different sets of selections are given.

5.2.1 General Selection

The general selection consists in cuts for selecting dijet events and for a further rejection of non ep events. The timing and vertex cuts are explained at the beginning then the different corrections and the jet selection.

- $|t_{FCAL} - t_{RCAL}| < 6$ ns: the average difference between the times of the energy depositions in the forward and rear calorimeters should be smaller than the above limit for events coming from the interaction region.

- $t_{RCAL} > -6$ ns: additional timing cut.
- $|z_{vertex}| < 40$ cm. Events should occur in the part of the central tracking detector which is well understood.

Corrections for noise and energy scale:

- Each calorimeter cell is read out by two photomultipliers (PMTs). Some calorimeter cells have photomultipliers which during the data taking were noisy. The energy of the cell is the sum of the energies measured by each of the two PMTs and the imbalance is defined as the (absolute value) of the difference of the two energies. Both pmts should, in an ideal case, measure the same energy and the imbalance would be zero. Whereas for a deposition related to noise an imbalance between the two pmts will be observed.
  An algorithm is used which selects “hot” or “noisy” cells according to the energies in the HAC and EMC sections and the imbalance value. Different criteria are then used for deciding to correct the energy of the cell or completely remove it as described in [Sa98]. This algorithm has been developed and improved using MC studies and is coded in the noise96 routine.
- Discrepancies between the absolute energy scale of the calorimeter and the simulation have been observed. These come from the not-perfect simulation of the inactive material in the simulation.
  The discrepancies are corrected by the Calcorr routine. The energies of BCAL and RCAL cells in the data are multiplied respectively by a constant factor of 1.06 and 1.025. The FCAL absolute scale energy is believed to be simulated correctly and is not corrected. More in [Re96].

The Jacquet-Blondel variable y_{JB} is calculated as:

$$y_{JB} = \frac{\sum_{hadrons} (E - p_z)}{2 \cdot E_e} , \tag{5.1}$$

where E_e is the energy of the incoming electron. y_{JB} is an estimator of the inelasticity y. In our case, the numerator is a sum over the hadronic energy depositions in the calorimeter cells (but not the cells which belong to the scattered electron, that are removed from the above sum).

Events are accepted with:

$$0.15 < y_{JB} < 0.45 \tag{5.2}$$

The lower cut $y_{JB} > 0.15$ removes beam-gas events since they have a lot of energy in the forward direction and, therefore, small y_{JB}. The upper cut $y_{JB} < 0.45$ is imposed from acceptance in the case of the intermediate Q^2 and is kept for consistency also in the other regions of photon virtuality. Due to energy losses of the particles

in the inactive material in front of the main calorimeter, the cut on the inelasticity corresponding to the above cut on the Jacquet-Blondel y_{JB} is:

$$0.2 < y < 0.55 \tag{5.3}$$

Jets are found using the k_T jet finding algorithm. For the photoproduction region the jet finding is done in the laboratory frame, whereas for the two other regions the jet finding is done in the γ^*P hadronic center-of-mass[3] frame (see section 4.3.1). Jet quantities in the γ^*P HCM frame are denoted with a $*$: E_T^*, η^*.

Events with two or more jets in the final state were selected. The found jets were ordered according to their transverse energy. The jet selection is then done in the following way:

- in the laboratory frame:
  - $-1 < \eta^{jet1,2} < 2$
  - $E_T^{jet1} > 7.5$ GeV
  - $E_T^{jet2} > 6.5$ GeV
- in the γ^*P h.c.m frame the corresponing cuts are:
  - $-3 < \eta^{*\,jet1,2} < 0$
  - $E_T^{*\,jet1} > 7.5$ GeV
  - $E_T^{*\,jet2} > 6.5$ GeV

As described in 4.3.1, the pseudorapidity of a particle in the γ^*P HCM frame is shifted with regards to its pseudorapidity in the laboratory frame. That is why the pseudorapidity cut in the γ^*P HCM frame is different from the one in the laboratory frame.

The E_T cut is needed because at lower transverse energies the resolution of jets in the detector becomes poor. The cut on the pseudorapidity is needed for selecting a region of the detector which is understood best. For high values of the pseudorapidity, its resolution becomes very poor. The cells become very large in η and the correlation between the hadron level jets and the measured ones is lost.

An asymmetric cut has been chosen for the transverse energy of the jets in order to avoid regions of the phase space where the NLO (next-to-leading-order) QCD theoretical calculations are not reliable due to infrared sensitivity [Pö99]. The available phase space in the case of a symmetric cut $E_T > 6.5$ GeV is shown in figure 5.1 in the plane of the transverse energies of the two highest E_T jets. The allowed space is the one between the two solid lines defined by $E_{T1} = E_{T2}$ and $E_{T2} > 6.5$ GeV. This type of cut is infrared sensitive due to the point $E_{T1} = E_{T2} = 6.5$ GeV. Near this point, due to limited phase space no third body (gluon) can be generated. In the NLO theoretical calculations the three-body contribution is positive and is suppressed. On the other hand, the two body (virtual) contributions are not suppressed (there

[3]Often the short notation HCM will be used instead of hadronic center of mass.

is no need to generate a final state gluon) and they are negative. This imbalance is the reason that the NLO calculations fail to describe the data in that region of phase space. As one can also see in the plot, this region of phase space can be avoided by introducing a difference δ between the two transverse energies. In our case $\delta = 1$ GeV.

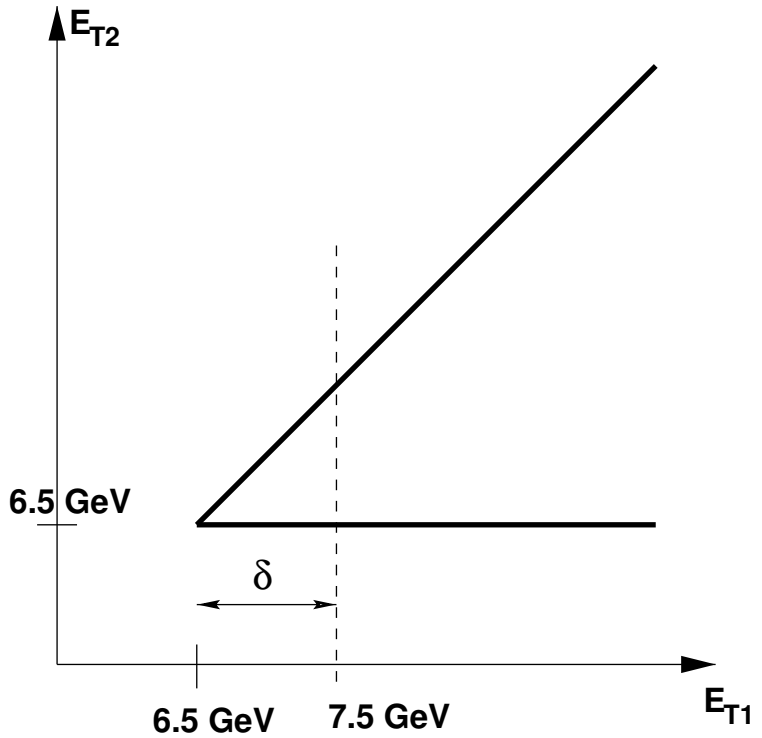

Figure 5.1 - The available phase space for the two highest transverse energy jets. Adding a difference δ between them helps to avoid the region of phase space where the NLO theoretical calculations are infrared sensitive. (hep-ph/9911221)

The transverse energy of the jets found in the main calorimeter has to be corrected for the losses in the inactive material. The correction procedure used is explained in the appendix A. The losses in energy do not affect the pseudorapidity of the jets so no correction is needed for it.

5.2.2 Photoproduction

The sample consists of events which have a very small photon virtuality Q^2. The method used in this analysis for selecting photoproduction events is the absence of

the electron in the detector, asking for the electron not to be detected in the main calorimeter. So the electron was "lost" down the (rear) beam pipe hole.

The limit on the photon virtuality set by the condition of not detecting it in the main calorimeter is $Q^2 < 1.$ GeV^2. But, because of the steep fall of the Q^2 - distribution with increasing Q^2 most of the events will have much lower photon virtualities $Q^2 \simeq 0.$. Using events generated with the MC simulation, the median[4] of the photon virtuality is evaluated to be about 10^{-5} GeV^2. The Q^2 distribution for simulated events is shown in figure 5.2. As one can see, most of the events are at photon virtualities much smaller than 1 GeV^2.

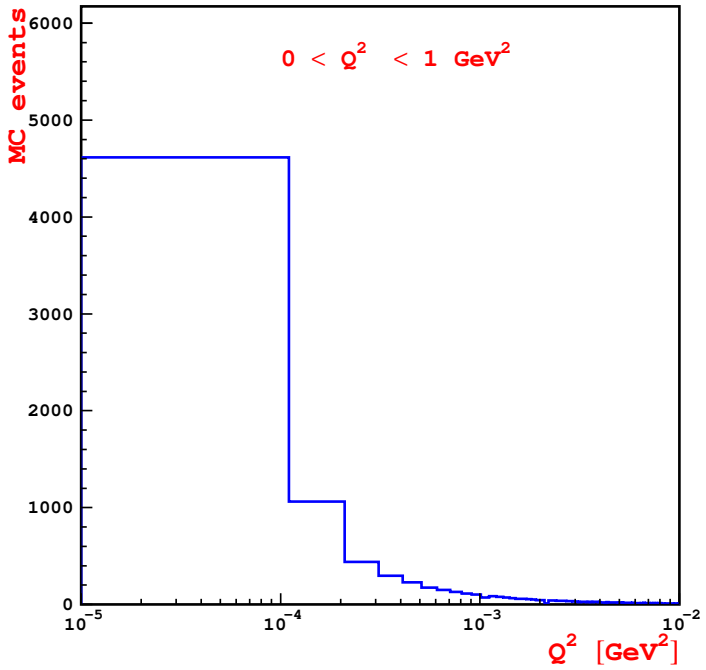

Figure 5.2 - The Q^2 distribution of the simulation events for the case of untagged sample. The requirement applied is $Q^2 < 1$ GeV^2. But, as one can see from the plot, most of the events are concentrated at very low values of the photon virtuality: $Q^2 \ll 1$ GeV^2.

In the section 5.2.4 below the detection of the electron in the main calorimeter is explained in more detail.

[4]For a certain probability distribution $f(x)$, the cumulative distribution function is $F(a) = \int_{-\infty}^{a} f(x)dx$ and the median x_{median} is the value of the variable x where: $F(x_{median}) = 0.5$. A randomly chosen value of x will have the same probability of being smaller or larger of x_{median}.

Events passing PHP cuts (3 pb^{-1})	
Cut	events passing
Online + remove calorimeter electron	391047
Jet cuts	47086
$\|z_{vertex}\| < 40$ cm	44797
y_{JB}-cut	22872

Table 5.1 - Numbers of events passing the cuts for the photoproduction (PHP) sample. The total luminosity for this region is 3 pb^{-1} and the analysis is done in the laboratory frame.

5.2.3 Intermediate Q^2

In the intermediate Q^2 region the electrons are tagged in the beam pipe calorimeter (BPC). The photon virtuality is: $0.1 < Q^2 < 0.55$ GeV^2. Only electrons detected in the north BPC module are used for the analysis. On the inner (north) side of the beam pipe there exists a window in order to allow for electrons to reach the BPC north module without preshowering. A similar window on the south side is smaller. Therefore the BPC south module is not used in the analysis. For a more detailed description of BPC see section 3.6.

In order to select well contained electrons in the BPC north, the following selection criteria were used:

- The BPC time is required to be within 3 ns of the mean BPC timing in the run to which the events belongs. For each run the timing of the electron is reconstructed in the BPC as the energy weighted time of all the channels.
- The reconstructed impact position on the BPC surface was constrained to be within the fiducial region of the BPC. The acceptance of the fiducial region extends in x over 6 vertical BPC strips and in y over 8 horizontal strips. The x position of the scattered electron at the BPC surface must fulfil the condition: $5.37 < x_{e/BPC} < 9.57$ cm and in y: $-2.62 < y_{e/BPC} < 2.98$ cm. Also the following two conditions must be satisfied: $y_{e/BPC} < 11.35$ cm$-x_{e/BPC}$, $y_{e/BPC} > -10.99$cm$+ x_{e/BPC}$.

  In figure 5.3 a schematic picture of BPC is shown together with the BPC fiducial volume drawn on it. The BPC vertical and horizontal fingers have also been schematically drawn and they form the "grid" on the BPC surface. The coordinates in the plot are in the ZEUS coordinate system and are given in cm. Data taken in the 1996-1997 running periods are shown on the plot as dots. These data have already passed the filter cuts and the dijet selection cuts as well as a (pre)-cut on the BPC energy of 3 GeV. One can see that most of the events are towards low $x_{e/BPC}$ position on the first vertical BPC finger. The

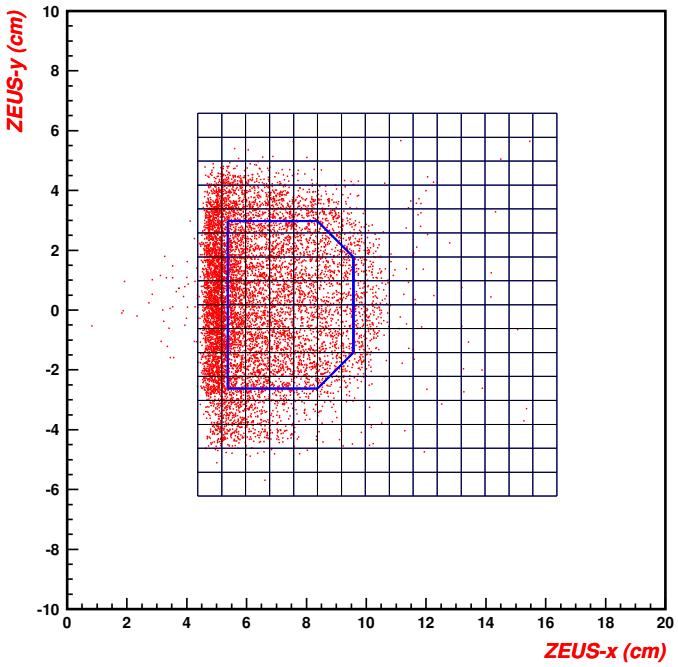

Figure 5.3 - BPC fiducial volume. The BPC is schematically shown with the vertical and horizontal strips and the fiducial volume is drawn. BPC data events passing the trigger selection and the jet cuts are shown as dots.

shape of the fiducial volume region is determined by the shape of the beam pipe window with less inactive material. In fact it is a "projection" of that window on the BPC surface.

- A shower cut width is applied. Let us denote by σ_x and σ_y the widths of the shower caused in the BPC by a particle respectively in the x and y directions. Hadronic showers are wider than electromagnetic showers. So a cut on the shower width in both directions is applied: $\sigma_x < 0.7$ cm, $\sigma_y < 0.7$ cm in order to select electromagnetic showers.

- The electron energy reconstructed in the BPC is required to be: $E_{e/BPC} > 12.5$ GeV. This cut is related to the cut: $y_{JB} < 0.45$. This cut also reduces the contamination of the sample from events with initial state radiation, hadronic showers, and pre-showered electrons. These processes decrease as the energy of the electron increases.

Similarly to the photoproduction case, DIS events are removed and the cut on the inelasticity calculated with the electron method, y_e, is also applied.

Events passing BPC cuts (38.2 **pb**$^{-1}$)	
Cut	events passing
Online + BPC energy > 3 GeV	75393
Jet cuts	9853
BPC fiducial region	4155
BPC shower width	3863
BPC energy > 12.5 GeV	2357
$\|z_{vertex}\| < 40$ cm	2299
y_{JB}-cut	2024

Table 5.2 - Numbers of events passing the cuts for the BPC sample. The total luminosity for this region is $38.2\ \mathrm{pb}^{-1}$.

5.2.4 DIS

The signature of (neutral current) events is the presence of the scattered electron in the final state. DIS (high Q^2) events are characterized by the presence of the scattered electron in the main calorimeter.

Positron or electron candidates are identified in the main uranium calorimeter using the Sinistra95 electron finder [Ab95]. Sinistra analyses clusters ("islands" of $3x3$ calorimeter cells around the highest energy cell) of energy depositions in the calorimeter and information such as the ratio of energy deposited in the electromagnetic part to the total energy deposited, the shower profile, tracking information. A neural network is used to optimize the electron identification.

Sinistra option number 5 is used. According to this option Sinistra will find the electron with the highest probability and will search for a CTD track pointing towards the vertex if this is possible. The Sinistra probability for the found electron candidate has to be larger than 0.9 and the energy of the found candidate has to be larger than 10 GeV. The cut on the electron energy is connected to the cut on the inelasticity: $y > 0.55$. The quantity y_{JB} is used here as well for estimating the inelasticity y. This is done for consistency with the other regions of photon virtuality.

The search for the CTD track is only possible if the electron is inside the CTD acceptance. Asking for a charged track in the CTD is used to avoid photons which are identified as electrons from Sinistra since they have a similar signature to them.

An additional cut is applied to the Sinistra electron in order to decide whether this is the scattered electron or not. The electron is identified as the scattered one using a cut on the inelasticity calculated with the electron method:

$$y_e = 1 - \frac{E'_e \cdot (1 - \cos\theta'_e)}{2 \cdot E_e} \tag{5.4}$$

where E'_e and θ'_e are the energy and the angle of the electron. If the electron found from Sinistra is not the scattered electron,it will generally be soft (of low energy). Therefore, scattered electrons are considered to be only the ones with $y_e < 0.7$. Events where Sinistra found an electron but do not fulfil this condition are not considered to be DIS events.

A box cut around the beam pipe on the position of the electron identified with Sinistra is applied: $|x_{e/\mathrm{Sinistra}}| < 14$ cm, $|y_{e/\mathrm{Sinistra}}| < 9$ cm. This cut makes sure that the electron is well contained inside the calorimeter and that there is no energy leak at the edge of the calorimeter. This cut removes a lot of events especially in the lower photon virtualities of the DIS region. The region of photon virtuality selected in the DIS subsample is $Q^2 > 1.5$ GeV^2.

Events passing DIS cuts (38.2 **pb**$^{-1}$)	
Cut	events passing
Online + Sinistra electron + box cut	836073
Jet cuts	72291
$\|z_{\mathrm{vertex}}\| < 40$ cm	68343
y_{JB}-cut	40889

Table 5.3 - Numbers of events passing the cuts for the DIS sample. The total luminosity for this region is $38.2\,\mathrm{pb}^{-1}$.

Chapter 6

Event and Detector Simulation

The experimental measurements in a High-Energy-Physics result from the convolution of underlying physical processes with various detector effects. This gives rise to complex final states. Therefore, the relation of the measurements with the physical quantities is not trivial because of two main reasons: first, we do not always understand completely the physics of the physical processes; second, the detector effects cannot be described analytically. In order to extract the physical observables from the measured quantities one has to correct for all detector related effects. This is usually done using Monte Carlo methods.

Monte Carlo methods are an essential tool in experimental High Energy Physics. They are used to simulate complete event samples. The simulation is divided in the *physics simulation* and the *detector simulation*. The generated events (MC events) can be used to correct the data for detector effects (acceptance, smearing, kinematic cuts) and for the extraction of physical quantities from the measurements. Generally, this can be done under the condition that the simulated final state quantities model well the measured ones in the High-Energy-Physics experiment. Under this condition one can assume that both the detector and the underlying physics are simulated correctly.

The physics simulation for jet production at HERA is usually divided in separate steps:

- **Hard Scattering**: perturbative QCD methods are used for calculating the cross section of the hard scattering at leading order (LO) or higher orders.
- **Parton Showering**: simulation of the initial and final QCD radiation from the partons.
- **Hadronization**: confinement in QCD does not allow partons (quarks and gluons) to be observed. Instead the partons fragment to colour neutral hadrons. This process is called hadronization. Hadronization is a non-perturbative process and different models are used for simulating it.

The output (the hadrons) of the physics simulation in form of the four-vectors of all particles, is fed into the detector simulation, which is based on the GEANT package [Br87]. Detailed simulation of the geometry and materials of the detector is

performed at this stage. In addition the three level trigger selection is simulated. The program used for the detector simulation is refined to give the best possible reproduction of the response of the detector. The full GEANT simulation of the ZEUS detector is done using the program MOZART (Monte Carlo for Zeus Analysis, Reconstruction and Trigger). MOZART simulates for every particle its interaction with the detector material, possible decays, the signals produced in the different components (tracking, calorimeters) and the digitisation of the signals, including the various sources of noise. Finally, the information from the detector and trigger simulation of the events is written to tape in an identical format to the real data. This allows to pass the Monte Carlo events through the same reconstruction chain and selection as the data and to make a direct comparison with them.

The stage after the parton showering is called *parton level*, the one after the hadronization *hadron level* and the final one *detector level*.

In this chapter the following matters will be treated:

- The Monte Carlo models used for correcting the data are described and filters used for preselecting the MC events are explained.
- The mixing of Monte Carlo events coming from the two main processes (resolved and direct) and the x_γ^{OBS} reweighting procedure are described.
- Multi Parton Interactions are introduced.
- A short description of a package used for generating hadron level simulation events is presented.
- Comparisons between data and MC are given in order to show the description of the data from the simulation.

6.1 Monte Carlo Models

6.1.1 Herwig

In this analysis the HERWIG[1] Monte Carlo package is used for correcting the data (Herwig5.9 [Ma92] and Herwig6.2 [Co00]). HERWIG is a general-purpose Monte Carlo generator, which includes the simulation of hard lepton-lepton, lepton-hadron and hadron-hadron scattering and soft hadron hadron interactions.

Direct and resolved photon events are generated separately using Herwig. The flux of photons from the positron beam is calculated using the Weizsäcker Williams Approximation (see also section 2.4.3). While for the direct photon events the exact matrix elements are used, Leading Order (LO) QCD diagrams are used for simulating the hard parton-parton scattering.

A parton-shower approach is used for initial- and final-state QCD radiation, including colour coherence effects and azimuthal correlations both within and between jets.

[1] HERWIG = an event generator for **H**adron **E**mission **R**eactions **W**ith **I**nterfering **G**luons. (including supersymmetric processes)

The parton emissions are continued until the transverse momentum squared of the partons becomes too small so that a transition into a non-perturbative region occurs.

After the hard scattering, the emitted partons are converted into outgoing hadrons. The hadronization is performed using the non-perturbative phenomenological cluster fragmentation model. In this model, all the gluons from the perturbative parton shower are first split in $q\bar{q}$ pairs and then all quarks are combined into colour singlet clusters. Light clusters are taken to be hadrons and heavier clusters are allowed to decay into lighter hadrons. In the ep collision, there are clusters containing the spectators from the incoming hadron (partons which do not take part into the hard interaction). The "underlying soft event" is related to the presence of the spectator partons and is dealed with using again the cluster fragmentation model.

A cut on the minimum transverse momentum which the hard process for the parton scattering produces is applied: $\hat{p}_T > \hat{p}_T^{min} = 2.5$ GeV. Two main reasons exist for doing this. First, this cross section diverges as $\hat{p}_T$ tends to zero so its theoretical calculation becomes difficult. Second, $\hat{p}_T^{min}$ is chosen small enough so that no events generated below it would pass the final cuts of the analysis. In fact, using this $\hat{p}_T^{min}$ value would allow for an unbiased sample of events with minimum transverse energy of the jets down to 5 GeV.

The parton distribution functions (pdfs) used are for the proton MRSA [Ma94] and for the resolved photon GRV LO [Gl92].

6.1.2 Pythia

This second Monte Carlo is used in order to verify the results obtained using HERWIG for correcting the data. Systematic effects on the measurement originating from the hadronization model were studied using Pythia. The Pythia sample generated contains multi parton interactions. They are simulated in Pythia very similarly to Herwig (the multi parton interactions were turned off in the Herwig sample).

Pythia is a popular Monte Carlo model in HEP [Sj00]. The emphasis is on multiparticle production in collisions between elementary particles, particularly in e^+e^-, pp and ep colliders[2].

Pythia uses the Weizsäcker Williams Approximation (Equivalent Photon Approximation) for calculating the flux of photons from the positron and Leading Order Diagrams are used for calculating the hard parton scattering.

The main difference between the two Monte Carlos is in the hadronization model. Pythia uses the *string fragmentation model* (also called the *Lund Model*) as implemented in JETSET [Sj94]. In this model, a colour string is stretched between each colour singlet $q\bar{q}$ pair moving apart. As the two partons move apart, the length of the string increases and so does the potential energy. When the string breaks up in two colour singlet strings a new $q\bar{q}$ is generated.

The parton distribution functions used for Pythia are MRSA for the proton and SAS1D for the photon [Sj95].

[2] The new Pythia6.1 used here is a merger of the previous programs Pythia5, Jetset7 and SPythia.

6.2 Multiple Parton Interactions

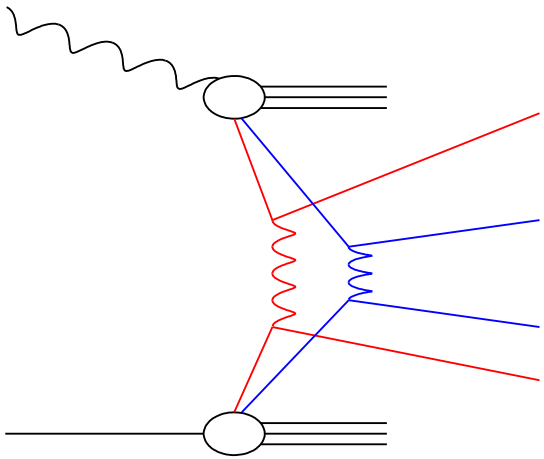

Figure 6.1 - Schematic representation of multiple parton scattering in the case of γp collisions. More than one had partonic scattering occurs in a single collision.

At HERA, the regions of small momentum fractions (x) of the incoming particles are explored. In this regime the density of partons is high. Therefore, probability for more than one hard partonic scattering occurring in a single γp collision becomes non-negligible. This effect is called *multiple parton scattering*, or *multiple interactions* (shortly MI). A schematic illustration of multiple parton scattering is shown in figure 6.1. The extra interaction in resolved processes occurs between a parton from the photon and a parton from the proton.

The multiple parton scattering affects the jet production in two ways:

1. The average number of jets per event increases when partons from secondary hard scatters have enough transverse momentum to produce their own jets.
2. The secondary scatters with low transverse momentum produce extra transverse energy which contributes to the pedestal energy underneath the other jets in the event.

Therefore, in general, the multiple parton scattering will lead to an increase in the jet cross sections for jets above a certain transverse energy cut (E_T^{cut}). The theory of multiple interactions is not well understood. Phenomenological models are used with several assumptions and parameters. They indicate that the effect of multiple

interactions can be significant at HERA energies. These models are usually called "eikonal" models [Bu96]. The inclusion of multiple scattering leads to significant changes in inclusive and dijet cross sections which should be understood before attempting to unfold parton distribution functions. As multiple interactions are generated by the density of partons in the photon, they are expected to be absent in the direct process, where the photon parton distributions play no part.

In order to allow for generation of events with multi parton interactions, the Herwig Monte Carlo is interfaced to the JIMMY library, written to generate these events with HERWIG [Bu96].

6.2.1 Hadron Level Theoretical Predictions - the HzTool Package

In this thesis an extensive use has been made of the HzTool utility package [Ca00]. This stand-alone package has been developed by the H1 and ZEUS collaborations and consists of a set of generic routines to easily produce various distributions using Monte Carlo generators. The events are generated at the hadron (or parton) level without the need of detector simulation. Routines have been written for the different Monte Carlos used for producing many of the theory curves shown throughout this thesis.

6.3 Filters applied to Simulated Events

The process of detector simulation is very time consuming. One should avoid generating events that would pass neither the detector level cuts nor the hadron level cuts. Therefore, prefilters were applied to the events at the hadron level before they are sent to the detector simulation. Before applying such filters, studies have been made to make sure that the final measurements will not be biased by them. There are two main filters applied to the simulated events: the *Jet Filter* and the *BPC Filter*. The jets filter is applied to the simulated events used for all the different data samples (photoproduction, BPC, DIS) while the BPC filter is (obviously) applied only to the simulated events used for correcting the BPC data sample.

6.3.1 The Jet Filter

The jet filter required that two jets were found at hadron level using the k_T or the Eucell jet-finder with transverse energy larger than 3 GeV and a pseudorapidity less than 3 (units of rapidity). Both these cut are chosen to be loose enough so they do not bias the final measurement. Only events satisfying these cuts were simulated further for detector effects.

For each event that is passed to the detector simulation the jet filter rejected between 2 to 3.5 events depending on the Q^2 and the type of process generated (resolved / direct). On the other hand, the events rejected by the trigger which would have

passed the cuts of the analysis are less than 0.2% of the total number of simulated events.

6.3.2 The BPC Filter

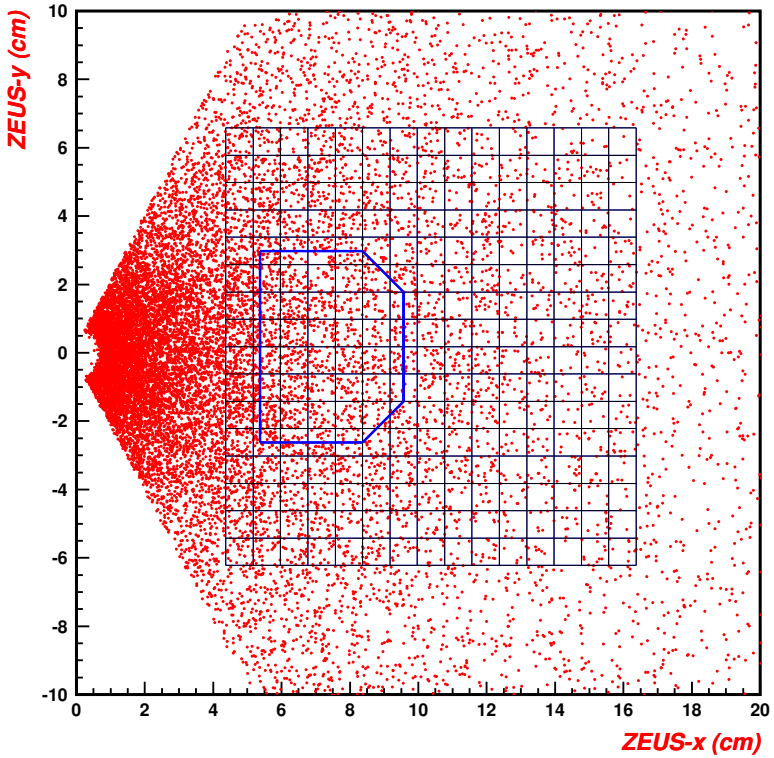

Figure 6.2 - The BPC filter for simulated events at hadron level. In the $x-y$ plane the BPC surface is shown and the electron position extrapolated at this surface for Monte Carlo events which pass the filter is plotted as a scatter plot. The φ angle of all the events is contained between the lines passing through the $(0,0)$ point and through $(3.4\text{ cm}, -6.7\text{ cm})$ and $(3.4\text{ cm}, 6.8\text{ cm})$. The angle between the lines is $\Delta\varphi_e = 2.20835$ rad. The geometrical reduction factor is: $2\pi/\Delta\varphi = 2.84519$.

For the intermediate Q^2 region, where the electron in the data is detected in the

Beam Pipe Calorimeter (BPC) an additional filter is applied. In this filter the scattered electron of the simulated event was required to be in a region "near" the Beam Pipe Calorimeter. More concretely, the filter cuts on the azimuthal angle φ_e of the scattered electron. This is done since electrons being outside a certain φ_e range cannot pass the calorimeter cuts who require the electron to hit the BPC. Because physical processes are symmetric in the azimuthal angle, no non-uniformities in the phase space are caused by this cut.

The effect of the filter can be seen in figure 6.2. In this figure the BPC surface is depicted (together with the BPC fiducial volume) in the $x-y$ plane. The position of the scattered electron in Monte Carlo events extrapolated at the BPC surface ($z = -293.8$ cm) and plotted as a scatter plot. Electrons passing the filter have a radial angle φ_e contained within two lines which pass through the $(0,0)$ point and through $(3.4\text{ cm}, -6.7\text{ cm})$ and $(3.4\text{ cm}, 6.8\text{ cm})$. The angle between the lines is $\Delta\varphi_e = 2.20835$ rad. The reduction factor resulting from such a filter is purely geometrical: $2\pi/\Delta\varphi = 2.84519$. That is, the filter accepts (approximately) only one out of three generated events. Near the point $(0,0)$ one observes a region where the events are also cut out (the circular limit near the origin of the scatter plot). This "cut" comes from the lower Q^2 limit ($Q^2 > 0.005$ GeV^2).

6.4 Mixing Direct and Resolved Processes

In generating Monte Carlo events the following procedure was used. Leading order direct photon events - LO-DIR[3] and leading order resolved photon events - LO-RES[4] were generated separately. Then they were mixed according to their theoretical cross section. Resolved photon events were generated not only in the photoproduction region, but also in the intermediate Q^2 region and in the DIS one. But by just mixing according to the cross section the description of the data was not good. In order to improve the description of the data by the simulation, an x_γ^{OBS}-*reweighting* is done. The normalisations of the LO resolved photon processes and LO direct photon processes were extracted from the data using a two-parameter fit to the uncorrected x_γ^{OBS} distributions. This procedure was applied separately for each Q^2 range. Since the photon parton distribution function used, GRV-LO, is intended for real photons, it does not take into account the suppression of the resolved photon component with increasing photon virtuality.

It is the mapping between the measured distributions and the generated ones which allows us to correct for detector effects and not the cross section which is calculated in the MC. As long as the relative resolved and direct cross sections are reweighted to match the data distributions in shape, the correction procedure is fine. Therefore, it makes sense to apply the x_γ^{OBS}-reweighting in order to improve the description of the data by the simulation.

Doing the above described x_γ^{OBS}-reweighting in each Q^2 bin separately introduces the photon suppression with virtuality also in the simulation the same way as in the data. The reweighting factors for the resolved and the direct Herwig5.9 Monte Carlo

[3] Process-id for direct photon events in Herwig is 9130.
[4] Process-id for resolved photon events in Herwig is 1500.

with GRV photon pdfs obtained from the x_γ^{OBS}-reweighting procedure are presented in the table 6.1. We observe that, as the photon virtuality increases, the change in the factors for the resolved MC is much larger ($2.037/0.047 \simeq 43$ times) than for the direct MC ($1.631/0.932 = 1.75$ - less than two). This is a reflection of the fact that we are taking the photon suppression from the data. In the case of the intermediate region of photon virtualities: $0.1 < Q^2 < 0.55$ GeV^2 the geometrical reduction factor described above (2.84159) has been taken out from the factors shown in the respective row of the table since this factor is related to the filter and not to the x_γ^{OBS}-reweighting. As we already stressed in the chapter on data selection, for the photoproduction region the reweighting (and the analysis) is done in the laboratory frame of reference. So, strictly speaking, the numbers in the first row are not directly comparable to the other numbers, extracted in the γ^*-proton c.m. frame of reference. But a change of frame in the case of photoproduction does not make a big difference.

x_γ^{OBS}-reweighting factors - Herwig5.9 (GRV-photon)		
Q^2 region (GeV^2)	resolved MC	direct MC
$Q^2 \simeq 0$	2.037	1.631
$0.1 < Q^2 < 0.55$	1.644	1.691
$1.5 < Q^2 < 4.5$	0.288	0.909
$4.5 < Q^2 < 10.5$	0.197	0.845
$10.5 < Q^2 < 49.0$	0.127	0.874
$49.0 < Q^2 < 10^4$	0.047	0.932

Table 6.1 - Factors to multiply the resolved and the direct MC obtained from the x_γ^{OBS}-reweighting procedure. With increasing photon virtuality the factors for resolved decrease faster than the ones for direct, because we are taking the photon suppression from the data as the Herwig5.9 with GRV photon pdfs does not have it.

The x_γ^{OBS} - distributions for the data and MC events in different Q^2 bins are shown in figure 6.3. The resolved and direct MC are mixed in the way we explained above and the x_γ^{OBS}-reweighting has been applied in each bin separately. The points are the ZEUS data and the solid line is the Herwig5.9 (resolved + direct). The shaded area is the direct only Monte Carlo. At higher Q^2 the resolved part is completely suppressed, as can be seen from the depletion of evens at low x_γ^{OBS} values.

6.5 Description of Data by the Simulation

In the following comparisons of the distributions of Monte Carlo generated samples with the ZEUS data at the detector level are shown. In general, the Monte Carlo should describe the data and if it significantly fails to do so, the correction for detector effects will be miscalculated. It will be shown that the MC describes the data well enough to keep the systematic uncertainties below the statistical errors of the

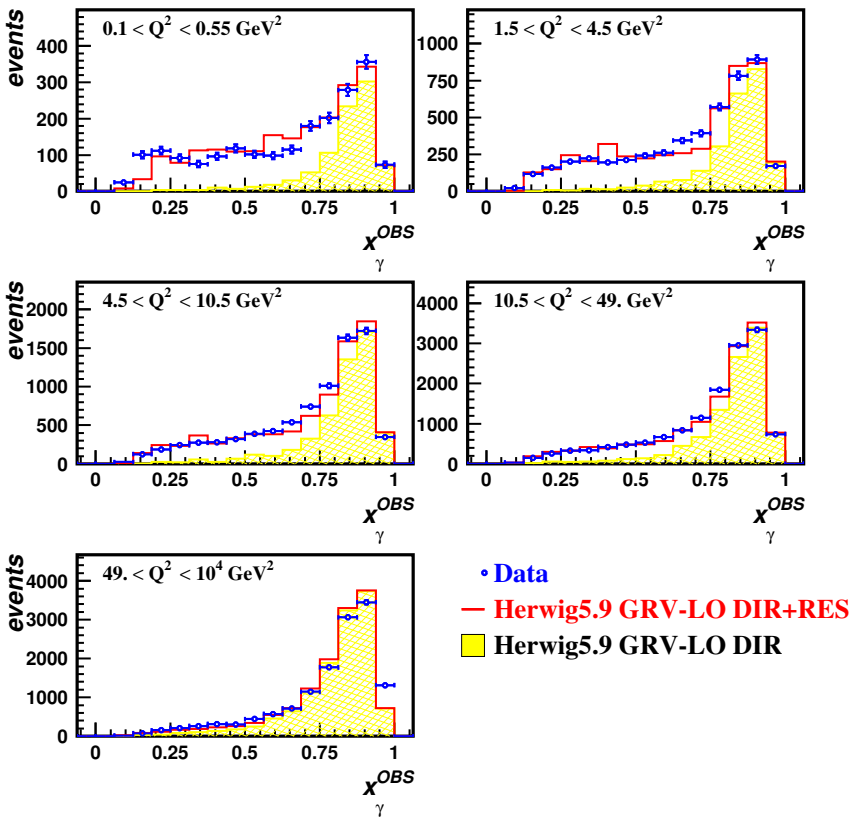

Figure 6.3 - x_γ^{OBS} - distributions for different Q^2 regions - intermediate Q^2 and DIS region. The points are the ZEUS data and the solid line is the Herwig5.9 Monte Carlo simulation with GRV as photon structure function parametrization. The shaded area is the Herwig direct events only. The x_γ^{OBS} reweighting is applied to the Monte Carlo. The description of the data by the Monte Carlo is generally good.

samples and allow for the bin-by-bin correction (which will be discussed in the next chapter).

Particularly important is the Monte Carlo description of the data for the quantities used in the event selection and for determining the kinematics. Therefore, emphasis in the comparisons is put on the jet quantities, on the electron quantities (used for

measuring the photon virtuality) and on the y_{JB} variable.

On each of the following plots, different quantities are compared with the simulation for the different bins of the photon virtuality. The points (filled circles) are the data measured with the ZEUS detector and the solid lines are the predictions of the Herwig5.9 (photon: GRV-LO) with x_γ^{OBS}-reweighting applied. In some plots the direct part only of the Herwig5.9 is shown as a shaded area. The jet energy correction has been applied (see appendix A).

A general comparison of the quantity x_γ^{OBS} is shown in figure 6.3 for the BPC and the DIS bins of Q^2. Cross sections versus x_γ^{OBS} and the ratio of the $x_\gamma^{OBS} < 0.75$ with the $x_\gamma^{OBS} > 0.75$ will be calculated so the description of x_γ^{OBS} is of particular importance. The description of the data by the MC is good in all the bins. For the photoproduction region, the description of the data by the MC is poorer (see 6.4 and discussion below).

Then according to the different regions:

- For the photoproduction region comparisons for y_{JB}, the transverse energies and pseudorapidities of the first two highest E_T jets and for the x_γ^{OBS} are shown in figure 6.4. The agreement is generally good. The excess of data at low transverse energies or high (forward) rapidities could be attributed to the multi parton interactions. Checks with MC with multi-parton interactions could not clearly conclude this.

  The disagreement in the description of x_γ^{OBS} comes mainly from the mismatch between data and MC in the y_{JB} variable. The simulation of the jet quantities is good.

- For the intermediate Q^2 region, the comparisons are shown in figure 6.5. The conclusions for the jet quantities here are similar to the photoproduction region. Specific to this region are the electron quantities, since the electron is measured here in the BPC. The electron energy and its angle measured in the BPC are shown in the two plots of the last row of 6.5. The simulation of these two quantities in the MC is good.

- The distributions for the DIS bins are shown in the figures 6.6, 6.7, 6.8, and 6.9. Now the electron is detected in the main calorimeter and its energy and angle (E_e, θ_e) are shown to be simulated correctly by the MC. These two quantities are important for the calculation of the photon virtuality. Both for the y_{JB} and the jet quantities the description by the simulation becomes better with increasing Q^2.

In general, we conclude that the for all the samples the agreement between data and MC is satisfactory for the hadrons as well as for the quantities measured from the electron. Mismatches of the simulation with the data will be taken into account in the systematic errors.

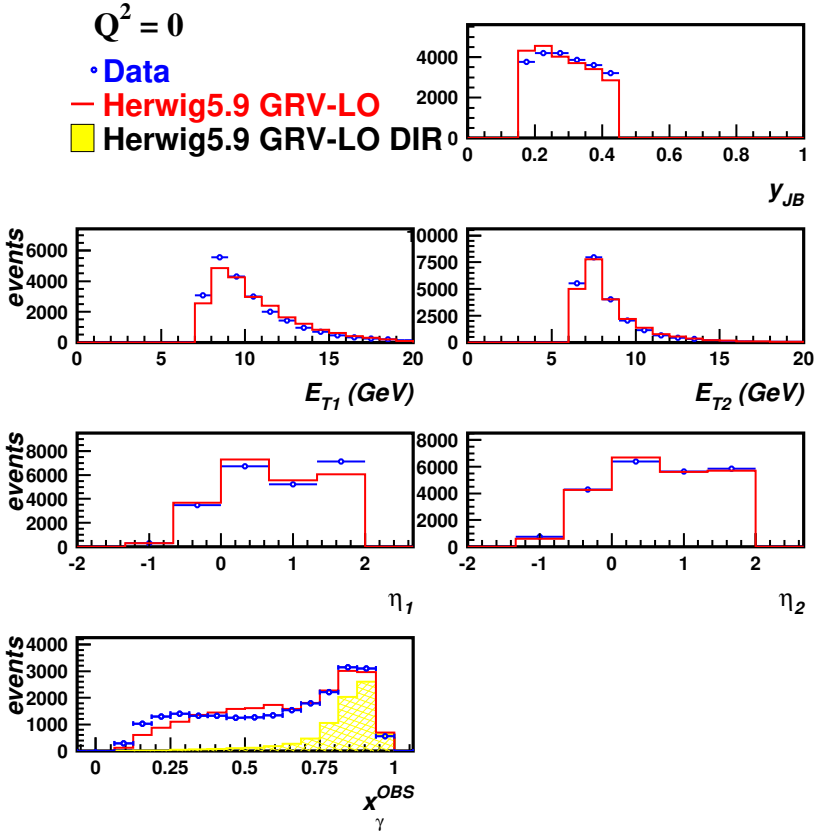

Figure 6.4 - Distributions of physical quantities for the photoproduction region. The points are the ZEUS data and the solid line the Herwig5.9 Monte Carlo. The shaded area is the Herwig direct events only. The agreement is generally good. For more details see text.

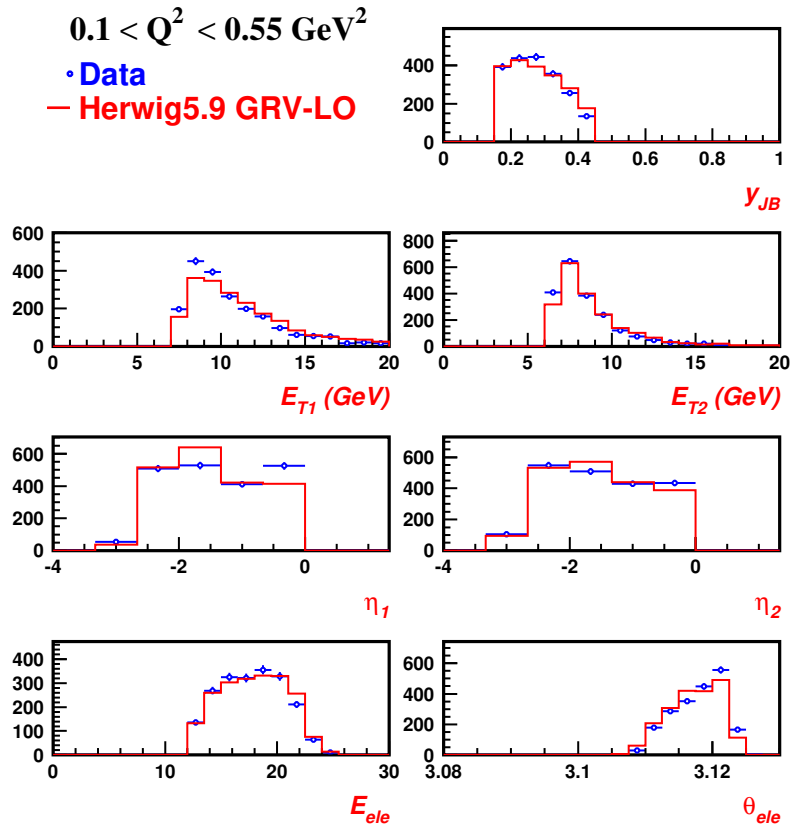

Figure 6.5 - Different distributions of important physical quantities used in the analysis. Comparison between the data (points) and the Herwig5.9 Monte Carlo simulation (solid line). The photon virtuality region is: $0.1 < Q^2 < 0.55$ GeV^2.

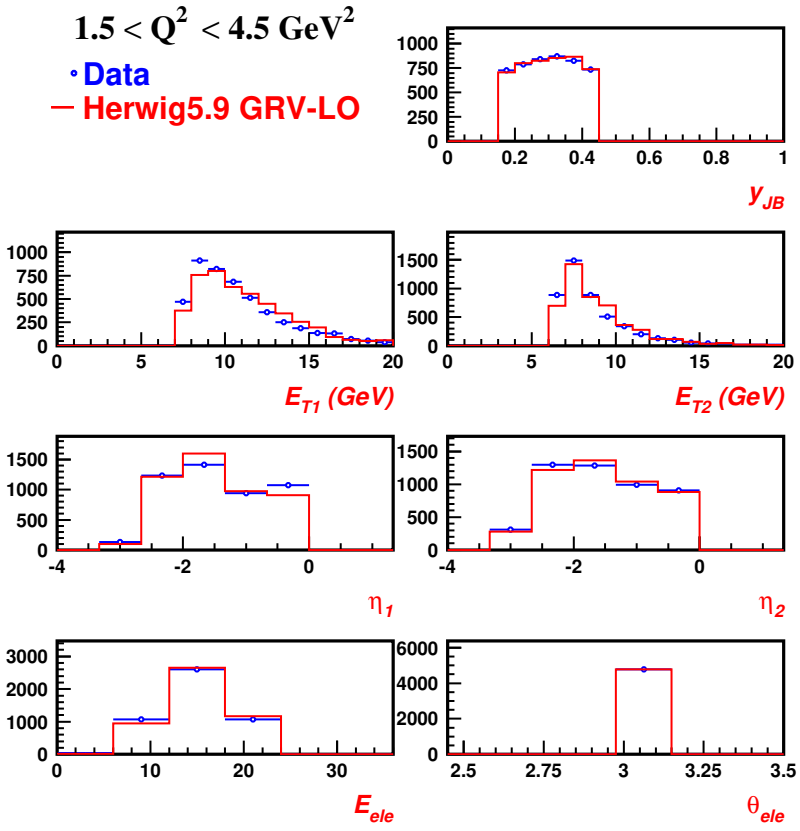

Figure 6.6 - Comparison between data and MC for the photon virtuality region $1.5 < Q^2 < 4.5$ GeV^2. Distributions of the y_{JB}, the jet quantities and the electron quantities. The points are the ZEUS data, the solid line the Herwig5.9 Monte Carlo.

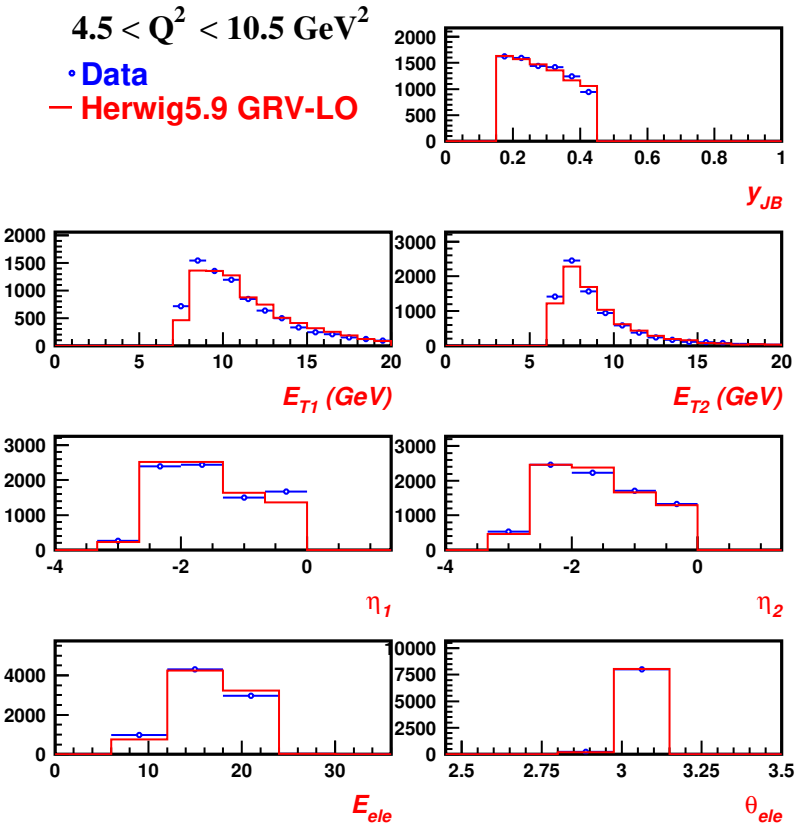

Figure 6.7 - Comparison between data and MC for the photon virtuality region $4.5 < Q^2 < 10.5$ GeV^2. Distributions of the y_{JB}, the jet quantities and the electron quantities. The points are the ZEUS data, the solid line the Herwig5.9 Monte Carlo.

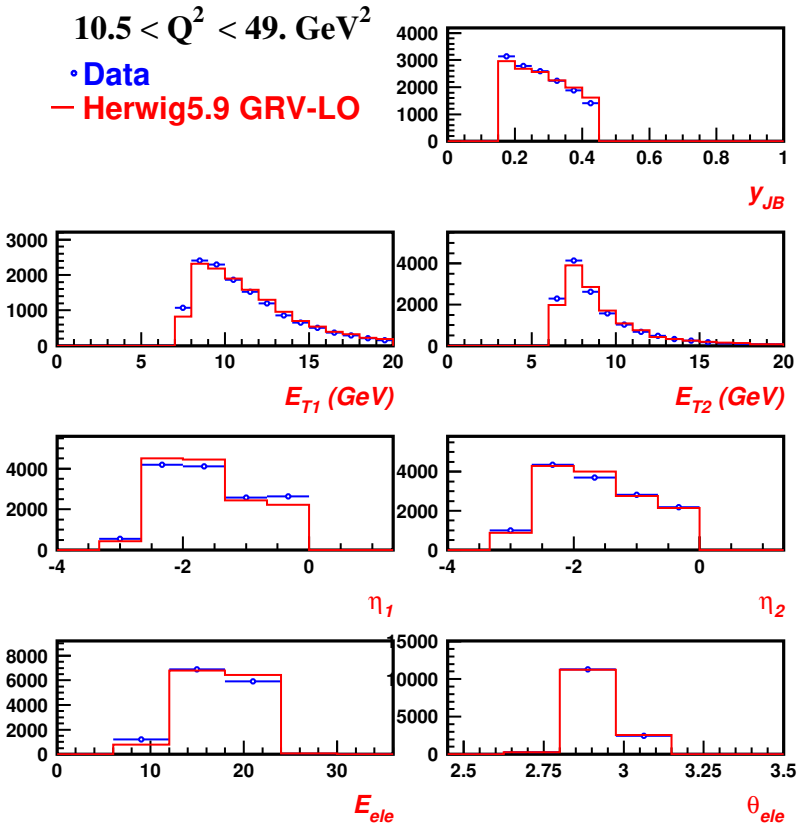

Figure 6.8 - Comparison between data and MC for the photon virtuality region $10.5 < Q^2 < 49.$ GeV^2. Distributions of the y_{JB}, the jet quantities and the electron quantities. The points are the ZEUS data, the solid line the Herwig5.9 Monte Carlo.

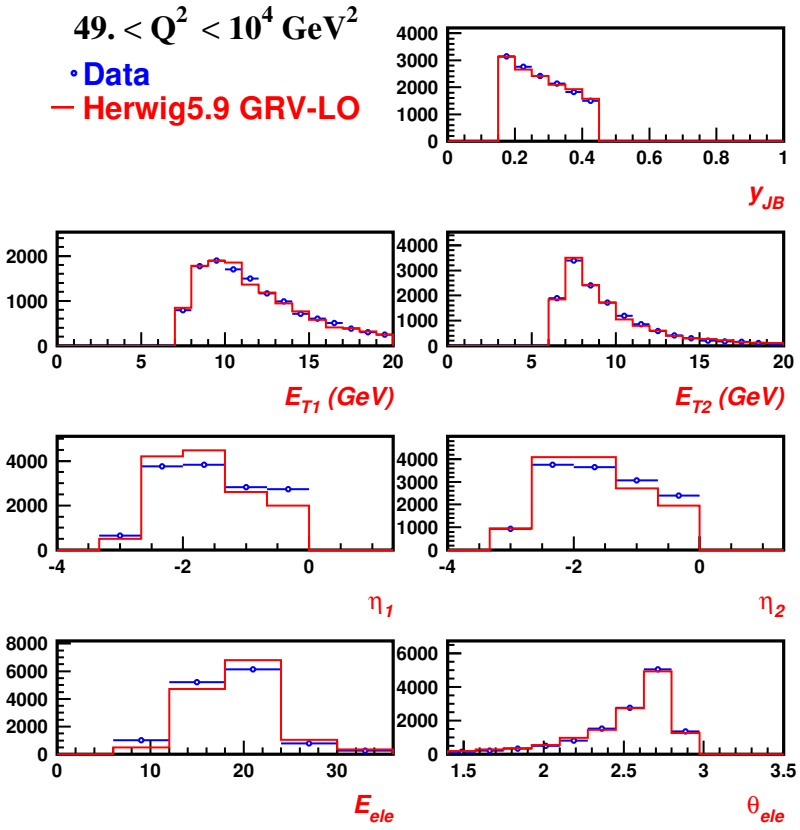

Figure 6.9 - Comparison between data and MC for the photon virtuality region $49. < Q^2 < 10^4\ \mathrm{GeV}^2$. Distributions of the y_{JB}, the jet quantities and the electron quantities. The points are the ZEUS data, the solid line the Herwig5.9 Monte Carlo.

Chapter 7

Analysis Method

7.1 Resolutions

The data measured in the ZEUS detector are a convolution of the physical quantities with the detector response. In general, if the true physical quantity has a certain value, the measured one will have a shift, called *bias*, and a spread around its value, called *resolution*. A good measurement will have both small bias and small resolution values. The evaluation of the systematic errors assigned to the corrected data depends on the resolution of the measurement. Also the size of the bins of a measured cross section are chosen such that they are (much) larger than the resolution in order to keep low the number of events that migrate outside the bin or from other bins into it.

The determination of the resolution and binning for a certain measured quantity X is done using a Monte Carlo simulation since for it both the desired quantity at the generator level (in our case: hadron level) and at the detector level is known. In the case of a dimensionful variable the resolution is defined as:

$$\delta_X = \frac{X^{\mathrm{GEN}} - X^{\mathrm{DET}}}{X^{\mathrm{GEN}}} \tag{7.1}$$

where GEN and DET stay for generator level and detector level respectively. The variable δ_X defined above has a certain distribution. Its mean value is the bias and the spread the resolution. Both the bias and the resolution here are in percent. For a dimensionless variable, the following definition is more appropriate:

$$\delta_X = X^{\mathrm{GEN}} - X^{\mathrm{DET}} \tag{7.2}$$

Here the bias and the resolution are in absolute values (not in percent). In each case, the resolution δ_X is a dimensionless variable. A discussion of the resolution for some measured quantities is discussed in the following.

The resolution plots of the photon virtuality for different regions of it are shown in figure 7.1. The bias is the mean value of the distribution μ and the resolution the spread σ. In the DIS samples ($Q^2 > 1.5$) the resolution improves with increasing Q^2.

In the BPC region the Q^2 resolution is better since here the electron is tagged in the BPC, and it has a better energy and position resolution than the main calorimeter[1]. For the photoproduction sample no Q^2 resolution can be measured since the Q^2 itself is not measured.

In figure 7.2 the resolution of the variable y_{JB} is shown for all the different samples. The resolution is not very dependent on the photon virtuality. In fact, y_{JB} depends largely on the resolution of the main calorimeter and this does not depend on Q^2.

Plots of the $\delta_{x_\gamma^{OBS}}$ for the different samples are shown in figure 7.3. The resolution of x_γ^{OBS} is related very much to the right identification of the scattered electron that affects both the y_{JB} and the jets (in the case of DIS the scattered electron cells are removed from jet finding). In the case of BPC, the electron identification is best and the x_γ^{OBS} resolution also. In the main calorimeter the resolution improves with Q^2 similarly to the photon virtuality case.

The resolutions of the transverse energies and of the pseudorapidities of the jets are studied in more detail in the appendix A. The pseudorapidities of the jets have very small bias. After applying the jet energy correction, also the transverse energies of the jets have small bias. The resolution of the pseudorapidity is $\delta_{\eta^{jet}} \simeq 0.08$ units of rapidity and the resolution of the transverse energy of the jets is $\delta_{E_T^{jet}} = 16\%$.

7.2 Data Correction

Dijet cross sections are measured from data (at the calorimeter) level and then the hadron level cross sections are calculated by correcting for the detector effects. The correction factors are calculated using the Monte Carlo simulation.

The method used in this analysis is the *bin-by-bin correction* method. In this method in each bin the number of data events is calculated (at the detector level) as well as the number of Monte Carlo events in that bin at the detector and at the hadron level. In each bin i the purity P_i is defined as:

$$P_i \equiv \frac{N_i^{GEN\&DET}}{N_i^{GEN}} \tag{7.3}$$

where N_i^{GEN} is the number of generated events in that bin (in our case hadron level) and $N_i^{GEN\&DET}$ is the number of events generated and reconstructed (detected, detector level) in that bin. The purity shows how many (in percent) of the generated events "remained" in the bin, that is were detected in that bin. Another important quantity for each bin i is the efficiency E_i that is defined:

$$E_i \equiv \frac{N_i^{GEN\&DET}}{N_i^{DET}} \tag{7.4}$$

N_i^{DET} is the number of Monte Carlo events detected (reconstructed) in bin i (at detector level). The efficiency shows how many (in percent) of the detected events were indeed generated in that bin.

For the intermediate photon virtuality region the purity is about 55% and almost flat in x_γ^{OBS}. The efficiency in this region increases with x_γ^{OBS} from 7% to 12%. The poor efficiency in this region is related to the small geometrical acceptance of the BPC detector. In the DIS bins the purity is about 50% and flat in x_γ^{OBS}. The efficiency

[1] The Q^2 resolution depends on the angular resolution and not on the position resolution. Since the BPC is positioned at very small angles, this resolution is the one which determines the Q^2 resolution.

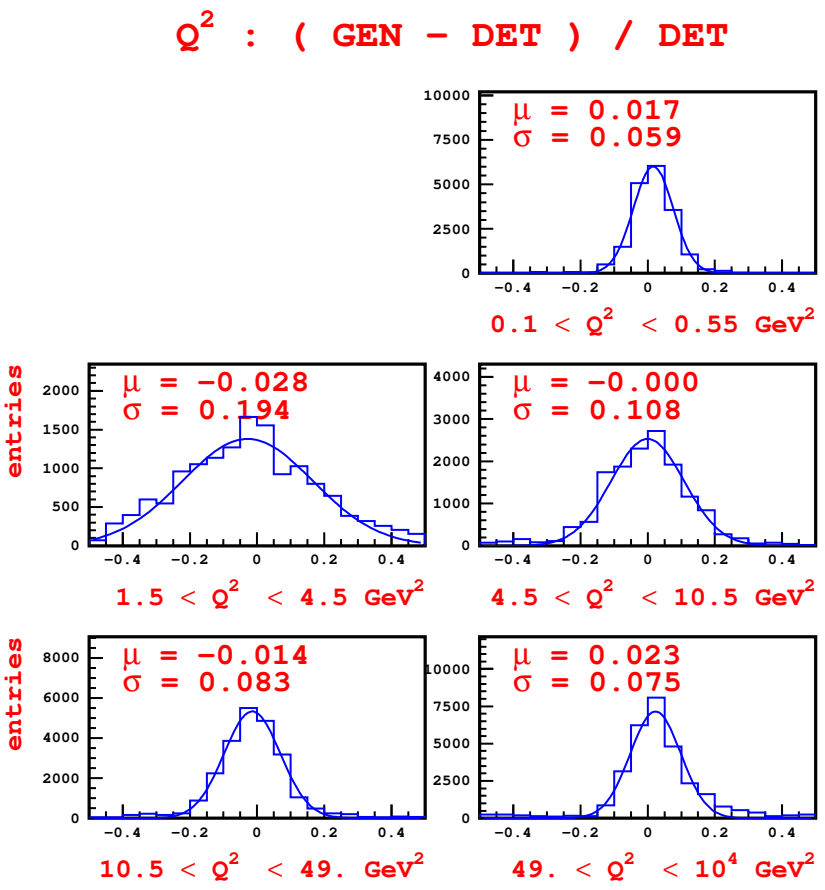

Figure 7.1 - Q^2 resolution in the different Q^2 bins. The resolution here is defined as $(Q^2(GEN)-Q^2(DET))/Q^2(DET)$, where GEN stays for generator level and DET for detector level. In the DIS bins ($Q^2 > 1.5$ GeV^2), the resolution gets better with increasing Q^2. The first bin has a better resolution because for that region of the photon virtuality the electron is detected in the Beam Pipe Calorimeter.

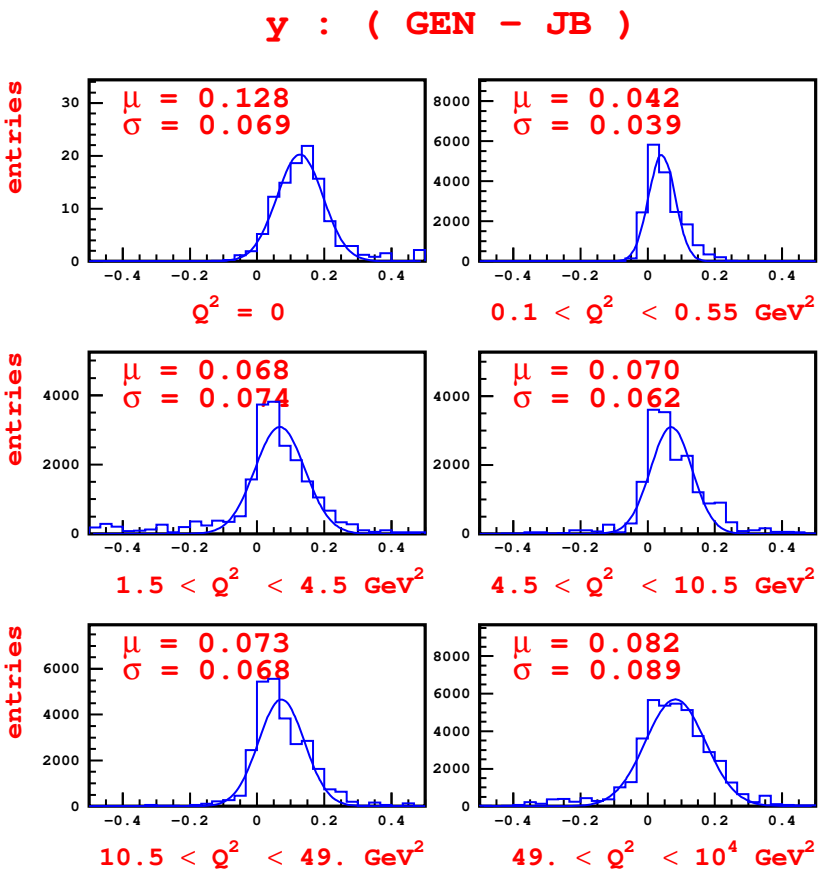

Figure 7.2 - y resolution in the different Q^2 bins. Here the resolution is defined as the difference of y(GEN) at the generator level with the y_{JB} at the detector level calculated with the Jacquet-Blondel method.

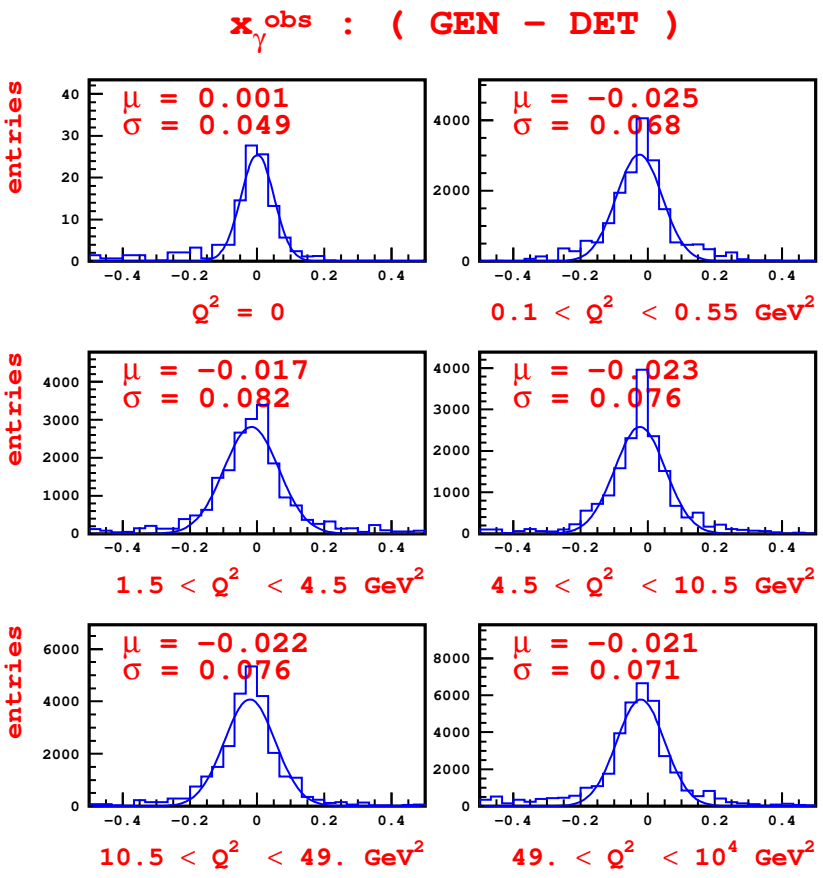

Figure 7.3 - x_γ^{OBS} resolution in the different Q^2 bins. The resolution here is the difference of x_γ^{OBS}(GEN) at the generator level with x_γ^{OBS}(DET) at the detector level.

is still flat in x_γ^{OBS} and has a value of about 40%. In the lowest photon virtuality bin $1.5 < Q^2 < 4.5$ GeV^2 the efficiency is again low and has a value of 12%. This is caused by the box cut around the beam pipe.

The number of data events N_i^{DAT} in bin i is corrected at the hadron level obtaining the corrected number of events N_i^{COR} by multiplying with a correction factor:

$$N_i^{COR} = N_i^{DAT} \cdot C_i^{MC} \tag{7.5}$$

where the correction factor is calculated from the MC as:

$$C_i^{MC} = \frac{P_i}{E_i} = \frac{N_i^{GEN}}{N_i^{DET}} \tag{7.6}$$

The cross section in each bin is calculated as the ratio of this number of events with the measured luminosity. The statistical error of the corrected number of events is calculated using error propagation. The data and the correction factor are independent of one another. The error of the data is calculated as the square root of the

number of events:

$$\left(\frac{\sigma_i^{COR}}{N_i^{COR}}\right)^2 = \left(\frac{\sqrt{(N_i^{DAT})}}{N_i^{DAT}}\right)^2 + \left(\frac{\sigma_{C_i^{MC}}}{C_i^{MC}}\right)^2 \tag{7.7}$$

It is not possible to calculate the error of the correction factor directly from the formula 7.6 because the number of generated N_i^{GEN} and reconstructed N_i^{DET} events are correlated and not independent[2]. For doing a correct error propagation the following numbers are defined for each bin:

$$\begin{aligned} A1 &= N(GEN \ \& \ DET) = N^{GEN\&DET} \\ A2 &= N(GEN \ \& \ \overline{DET}) \\ A3 &= N(\overline{GEN} \ \& \ DET) \end{aligned} \tag{7.8}$$

$\overline{DET}$ is the set of events not detected (reconstructed) in this bin at the detector level and $\overline{GEN}$ is the set of events not generated in this bin at hadron level. The three numbers above are independent of one another, their respective errors can be calculated using Poisson statistics, and the following relations:

$$\begin{aligned} N_i^{GEN} &= A1_i + A2_i \\ N_i^{DET} &= A2_i + A3_i \\ C_i^{MC} &= \frac{A1_i + A2_i}{A1_i + A3_i} \end{aligned} \tag{7.9}$$

At this point the error of the correction can be calculated using error propagation:

$$\left(\frac{\sigma_{C_i^{MC}}}{C_i^{MC}}\right)^2 = \left(\frac{\partial C_i^{MC}}{\partial A1_i} \cdot \frac{\sigma_{A1_i}}{A1_i}\right)^2 + \left(\frac{\partial C_i^{MC}}{\partial A2_i} \cdot \frac{\sigma_{A2_i}}{A2_i}\right)^2 + \left(\frac{\partial C_i^{MC}}{\partial A3_i} \cdot \frac{\sigma_{A3_i}}{A3_i}\right)^2 \tag{7.10}$$

The three differential derivatives and the three errors on the numbers $A1$, $A2$, and $A3$ are:

$$\begin{aligned} \frac{\partial C_i^{MC}}{\partial A1_i} &= \frac{A3_i - A2_i}{(A1_i + A3_i)^2} & \sigma_{A1_i} &= \sqrt{A1_i} \\ \frac{\partial C_i^{MC}}{\partial A2_i} &= \frac{1}{A1_i + A3_i} & \sigma_{A2_i} &= \sqrt{A2_i} \\ \frac{\partial C_i^{MC}}{\partial A3_i} &= -\frac{A1_i + A2_i}{(A1_i + A3_i)^2} & \sigma_{A3_i} &= \sqrt{A3_i} \end{aligned} \tag{7.11}$$

Using the relations (7.11), (7.10), (7.8), and (7.7) the error for the corrected number of events is calculated. The correction factors versus x_γ^{OBS} for the different Q^2 are

[2] In the case of an ideal detector, these two sets of events would be exactly the same.

shown in figure 7.4 together with their statistical errors. The correction factors for the BPC region ($0.1 < Q^2 < 0.55$ GeV^2) and the lowest DIS bin ($1.5 < Q^2 < 4.5$ GeV^2) are larger than the other ones. In the BPC region this comes because of the small geometrical acceptance of the BPC, whereas in the DIS low Q^2 this is caused from the box cut which removes a lot of electrons for these values of photon virtuality.

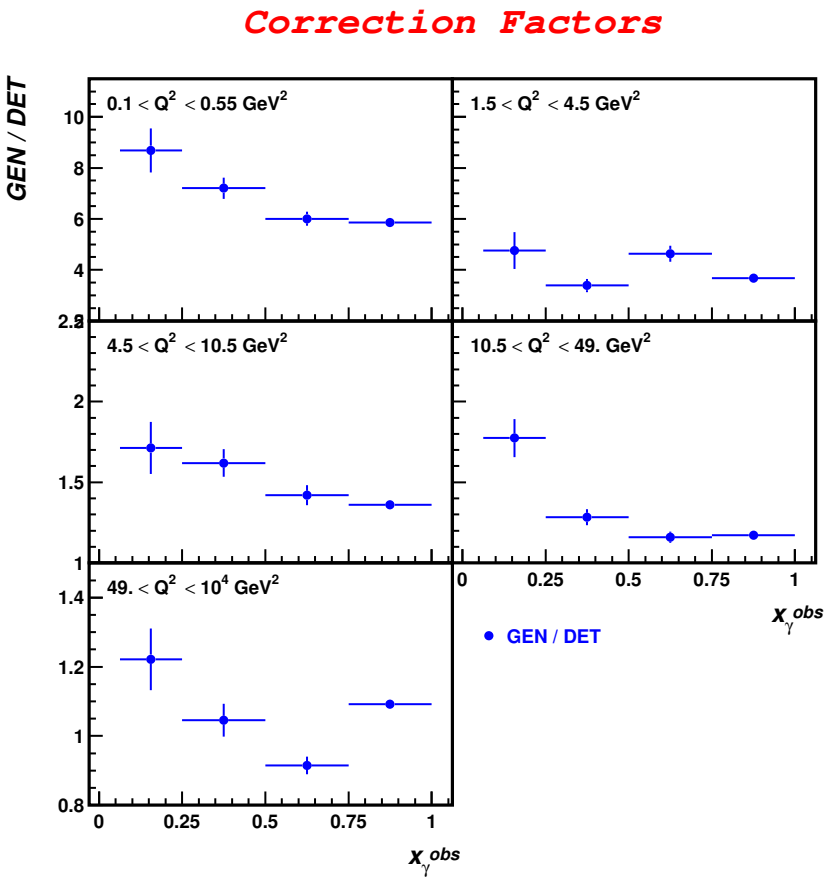

Figure 7.4 - Correction factors C_i^{MC} versus x_γ^{OBS} for the different Q^2 regions. The plotted errors are statistical. The correction factors for the two lowest Q^2 regions (BPC and low DIS) are larger than the other ones. For the BPC this reflects its small geometrical acceptance. For the lowest DIS Q^2 region this is an effect of the box cut.

The corrected number of events depends on the Monte Carlo used. If the Monte Carlo used does not describe the data, the bin-by-bin correction method becomes

model dependent. In our case we have already shown that the MC describes the data. To check the errors coming from a bad description of the data from the Monte Carlo and to study the use of another model, systematic studies have been performed which are described in the next session.

7.3 Systematic Studies

As was described in the previous sections, the cross section can be calculated and its statistical errors coming both from the data and from the simulation. The statistical errors coming from the simulation are in all the samples smaller (in some parts indeed negligible) in comparison with the statistical errors of the respective data samples. There is still another source of errors. It is possible that the measured quantity is systematically mismeasured. This mismeasurement comes from an imperfect understanding and simulation of detector effects in the Monte Carlo. Studies are done in order to estimate the systematic uncertainties. One source of uncertainties is the mismeasurement of the variables on which we cut at the detector level. Therefore, the cuts at the calorimeter level are varied by one standard deviation (of the response function) in both directions around the calorimeter level cut value by keeping the hadron level cut (the definition of the cross section) fixed. In the ideal case of the Monte Carlo describing perfectly the data, such a change of the cut would not affect at all the final result. But since this is not true, changes are observed in the cross section. With this method the following cuts are checked:

- cut on the transverse energy of the jets. The cut is changed by $\pm\sigma_{E_T^{jet}}$.
- cut on the pseudorapidity of the jets. $\pm\delta_{\eta^{jet}}$.
- cut on y_{JB} (both cuts). $\pm\delta_{y_{JB}}$.
- cut on electron energy. $\pm\delta_{E_e}$. Here different values of the resolution are used (also the cuts are different).
- BPC fiducial volume cut - BPC only - $\pm\delta_{x_{BPC}}$ The edges of the fiducial cut are shifted by the BPC resolution taken to be $\pm 1\,mm$.
- box cut - DIS only - the edges of the box cut around the beam pipe are shifted by $\pm 0.5\,cm$.

These are the sources of the largest systematic errors. Changes in other variables produce uncertainties which are much smaller than the ones above. The systematic errors discussed are uncorrelated and in evaluating the total systematic error are added in quadrature.

There are still three main sources of systematic errors:

- The energy scale of the calorimeter is known only within 5% uncertainty,
- The luminosity is measured with a 1.5% uncertainty.

- The description of the hadronization corrections in the simulation is model dependent.

These sources of systematic errors are correlated, since they affect all the measurements simultaneously. The uncertainty coming from the luminosity measurement is not shown in the following plots.

The correlated uncertainty coming from the energy scale of the calorimeter is studied by changing the energy of all the calorimeter cells up and down by $\pm 5\%$ and redoing the analysis. This uncertainty is shown in the following plots. This is the source of the largest correlated systematic uncertainties.

In order to evaluate the systematic uncertainty coming from a wrong modelling of the hadronization process, the correction with Pythia and with Herwig is compared since these two Monte Carlos use (as described in chapter 6) different models for this process. Plots of the correction factors versus x_γ^{OBS} using Herwig and Pythia are shown in the figure 7.5. A finer binning compared to the cross section one has been chosen in order to study any dependence of the correction factors versus x_γ^{OBS}. No such dependence is seen. Both correction factors are large in the first bin but the number of events in this bin is small. The ratio of the two correction factors versus x_γ^{OBS} is shown in figure 7.6. Again, the ratio has no x_γ^{OBS} dependence and its value is about 1.20. The uncertainty coming from the hadronization corrections is therefore evaluated to be 20%. This uncertainty is not shown in the following plots. The value of 20% is in agreement with previous studies of this uncertainty [ZEv].

In the plots which follow the systematic uncertainties in percent are shown for all the checks mentioned above in the different samples. In each plot both the systematic uncertainties that increase the cross section (positive uncertainties) and the ones that decrease it (negative uncertainties) are shown versus x_γ^{OBS}. The x_γ^{OBS} bins are the sames as the ones used (next chapter) for calculating the cross section so an immediate correspondence to the cross section points can be made. The points are connected with straight lines to simplify the comparison between them. A shaded band is also plotted at $\pm 10\%$ to allow a fast quantitative evaluation and to compare more easily between the different sources of uncertainties.

The BPC region is shown in figure 7.7. The correlated energy scale uncertainty causes a systematic uncertainty of the cross section of above 20%. This value is almost the same also in the other DIS regions. All the uncorrelated sources of uncertainty are below the 10% level. In the case of the DIS bins shown in figures 7.8, 7.9, 7.10, 7.11 the main sources of uncorrelated systematic uncertainties are the y_{JB} cut and the cut on the transverse energy of the jets. In some points the value of uncertainties go up and seem to take values up to 20%. But one has to bear in mind that these points are usually points with low statistics and therefore, the systematic error is low due to this rather than from a bad simulation. The box cut is important only at lower Q^2. As we go to higher photon virtualities the uncertainty from this cut becomes zero. This is related to the fact that this cut removes electrons only at small angles (small Q^2).

There exists another source of systematic uncertainties that is not studied here in detail. The incoming electron (positron) may radiate a photon before it undergoes the interaction with the proton. Such a process is called *initial state radiation*. Our

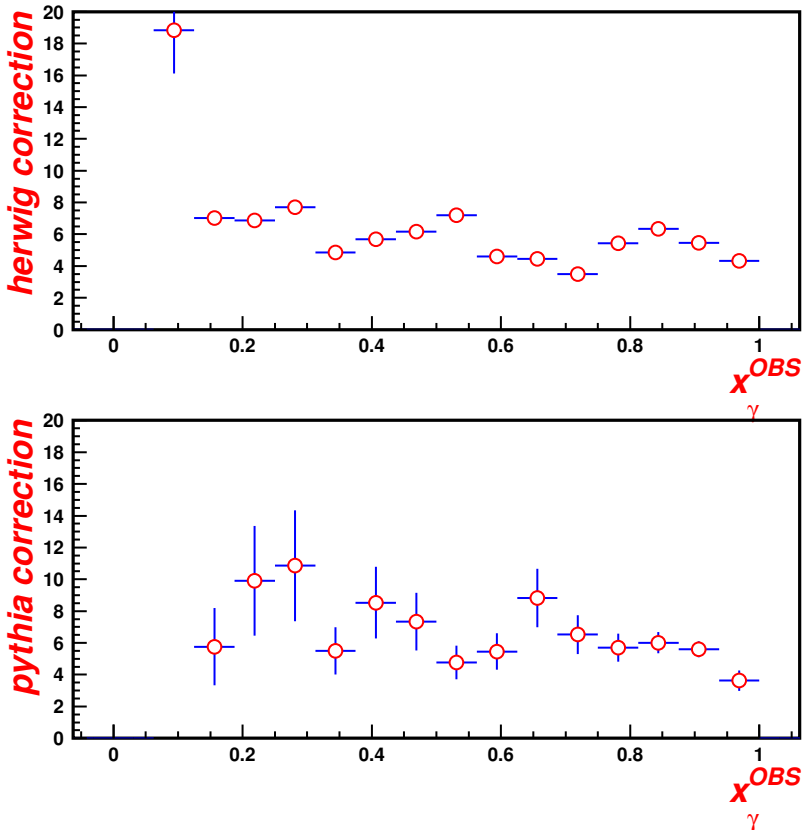

Figure 7.5 - Correction factors on x_γ^{OBS} for Herwig (upper plot), Pythia (lower plot) for the region $0.1 < Q^2 < 0.55$. No dependence of the correction versus x_γ^{OBS} is seen. In the first bin of x_γ^{OBS} the correction factors are large but the number of events in this bins is small.

Monte Carlo does not simulate such events as there is no Monte Carlo with radiative corrections for the resolved photon processes. Studies of this process have shown that the initial state radiation causes an effective overestimation of both Q^2 and y. The effect is comparable to the systematic checks computed above. A more detailed discussion can be found in [Ne99]. In absence of a rigourous treatment, this uncertainty is not included in the systematic error.

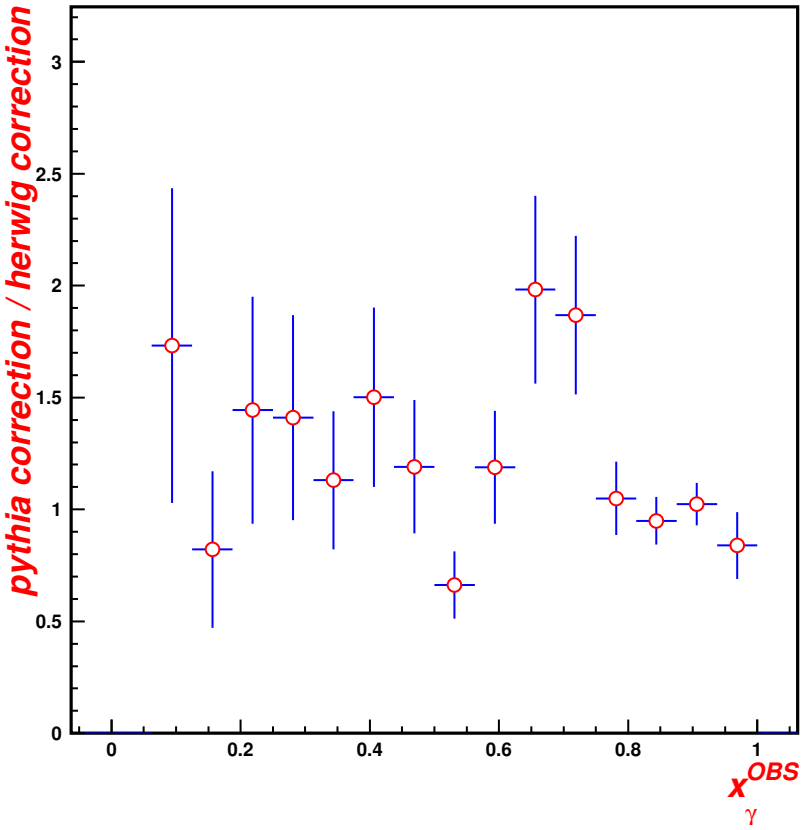

Figure 7.6 - The ratio of the correction factors for Herwig and Pythia versus x_γ^{OBS} for $0.1 < Q^2 < 0.55$. The ratio shows no x_γ^{OBS} dependence and has a value of about 1.2. Therefore, the unceratinty coming from the hadronization corrections is evaluated to be 20%.

7.4 Photoproduction Analysis

In the photoproduction analysis the electron is not tagged and no boost is possible in this case[3]. The ratio $R^{DATA-LAB} = \sigma^{LAB}(x_\gamma^{OBS} < 0.75)/\sigma^{LAB}(x_\gamma^{OBS} > 0.75)$ is calculated first in the laboratory system. By $R^{HRW-HCM}(\text{HCM cuts})$ is denoted the same

[3]In principle one could use the y_{JB} variable to calculate the electron energy and make the boost but its resolution its not good and this would lead to very big uncertainties in the boost.

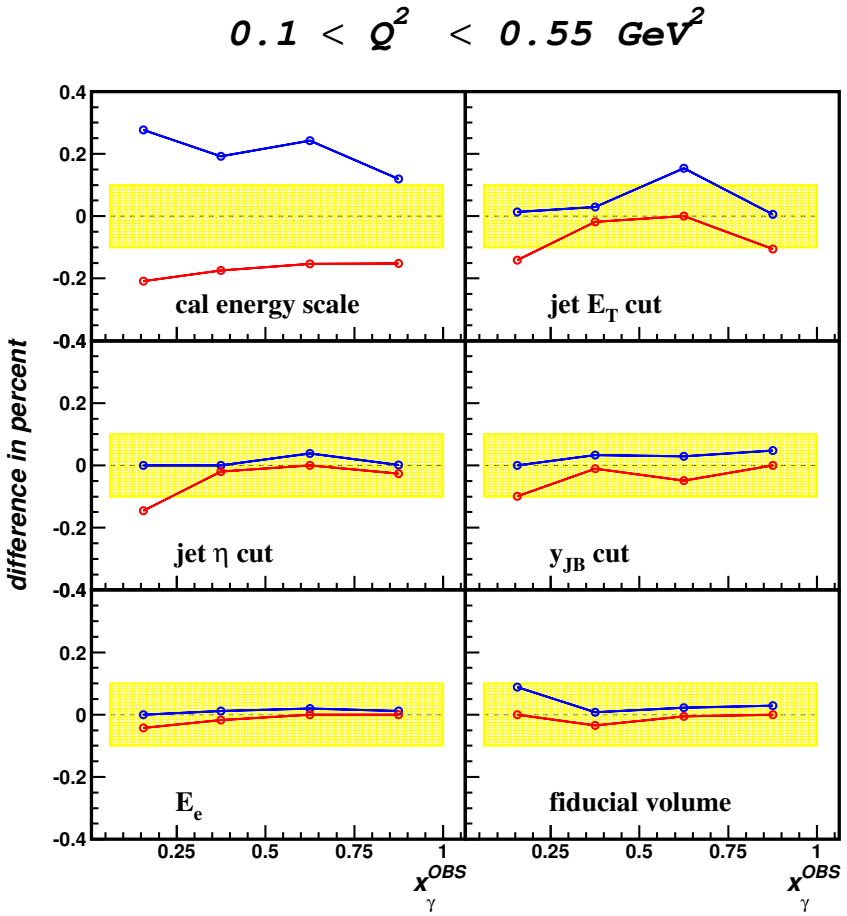

Figure 7.7 - Systematic studies in the virtuality region: $0.1 < Q^2 < 0.55$ GeV^2. All uncertainties are shown in percent and a shaded band of $\pm 10\%$ is plotted to facilitate the visual evaluation of them. The upper left plot shows the correlated energy scale uncertainty. The other plots show the different uncorrelated uncertainties. Specific for this region is the uncertainty on the fiducial volume cut of the BPC detector.

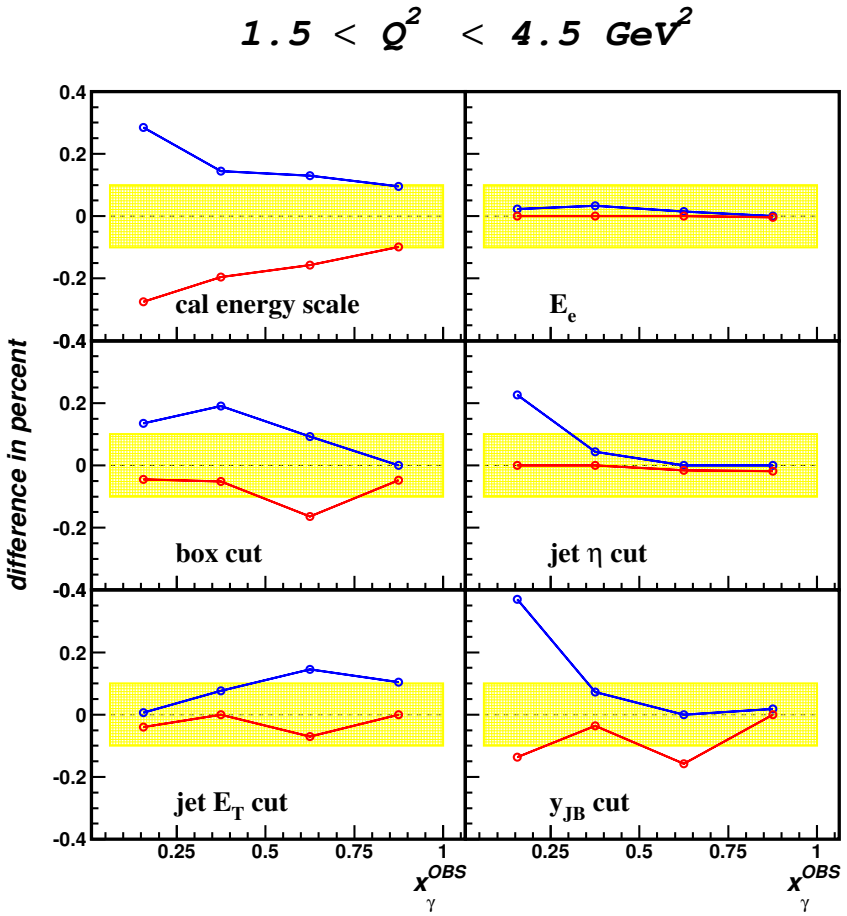

Figure 7.8 - Systematic studies in the virtuality region $1.5 < Q^2 < 4.5$ GeV^2. All uncertainties are shown in percent and a shaded band of $\pm 10\%$ is plotted to facilitate the visual evaluation of them. The box cut around the beam pipe on the position of the electron has a large uncorrelated systematic uncertainty at this lower Q^2.

ratio calculated at the hadron level in the γ^*-proton hadronic c.m. frame with the Herwig MC. For $R^{HRW-HCM}(\text{HCM cuts})$ the cuts applied are the ones at the hadron level for the HCM as described in the chapter 5. Similarly, $R^{HRW-LAB}(\text{LAB cuts})$ is the same ratio calculated with Herwig in the laboratory system with the respective cuts in the laboratory frame. The only formal difference between the two sets of

cuts in the lab and in the γ^*-proton frame is the pseudorapidity cut on the jets. The corrected data ratio in the γ^*-proton frame we calculate using the formula:

$$R^{DATA-HCM} = R^{DATA-LAB} \cdot \frac{R^{HRW-HCM}(\text{HCM cuts})}{R^{HRW-LAB}(\text{LAB cuts})} \qquad (7.12)$$

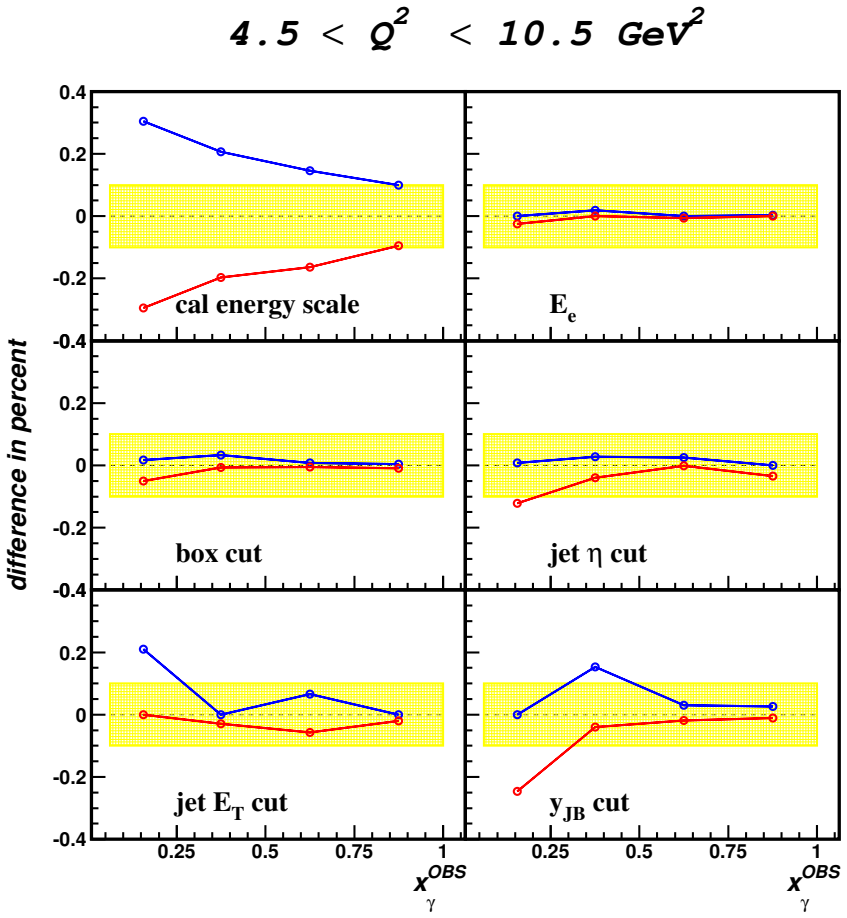

Figure 7.9 - Systematic studies in the virtuality region $4.5 < Q^2 < 10.5$ GeV^2. The ucertainty on the box cut becomes here small. The uncertainties on the y_{JB} and jet quantities cuts remain the main source of uncorrelated uncertainties.

The ratio in the laboratory frame has a value of

$$R^{DATA-LAB} = 1.41 \pm 0.05 \tag{7.13}$$

where the error is a statistical one. The value of the correction factor is for Herwig with the GRV pdfs for the photon:

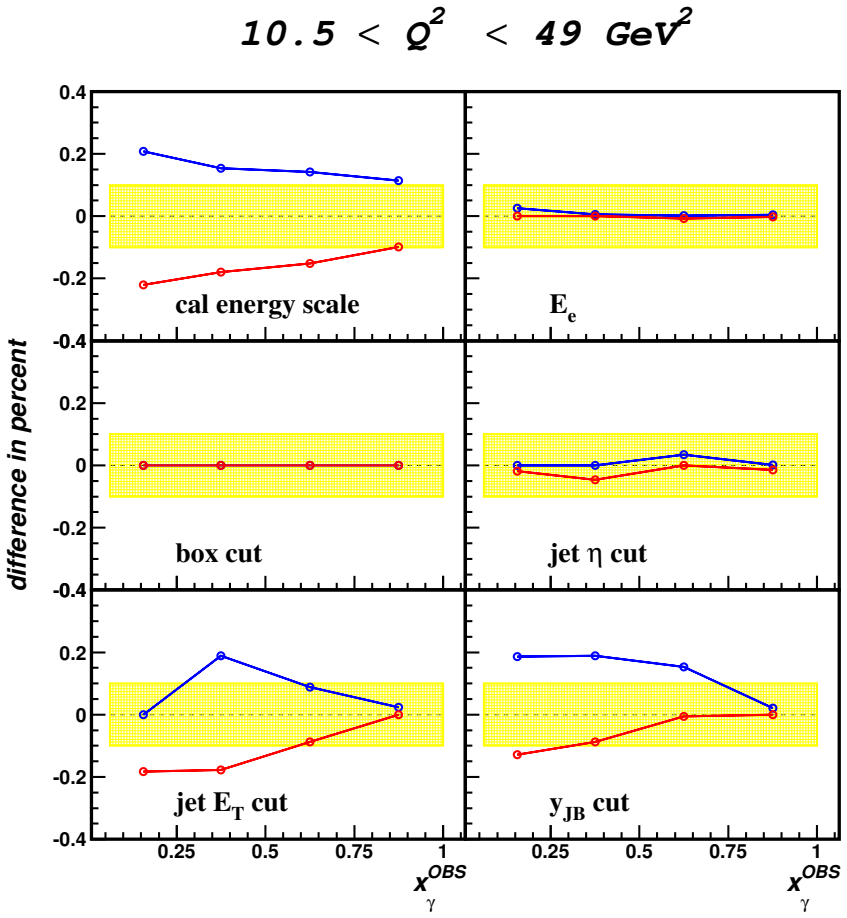

Figure 7.10 - Systematic studies in the virtuality region $10.5 < Q^2 < 49.0$ GeV^2.

$$\frac{R^{HRW-HCM}(\text{HCM cuts})}{R^{HRW-LAB}(\text{LAB cuts})} = \frac{1.493}{1.165} = 1.2815 \tag{7.14}$$

No statistical error is included here since it is smaller than the statistical error for the data[4].

In the case of photoproduction the same systematic checks for the cross section are

[4]The values for the correction factors are calculated using the HzTool package and a very large number of simulation events are generated.

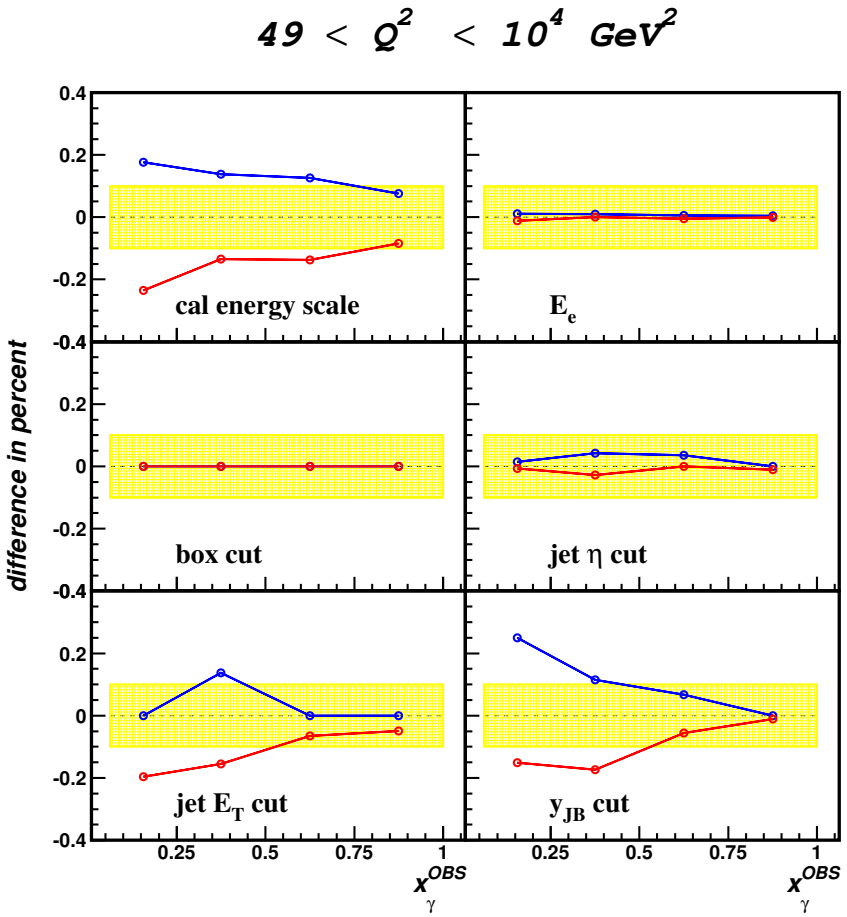

Figure 7.11 - Systematic studies in the virtuality region $4.0 < Q^2 < 10^4$ GeV^2.

done as in the previous section. Obviously, the check on the cut on the electron energy is not present here since the cut itself is missing. The correlated systematics coming from the energy scale is similar to the case of the BPC and DIS regions and has a (maximum) value of 15% From the uncorrelated systematic uncertainties the jet transverse energy cut and the y_{JB} cut uncertainties are the largest. Varying the E_T cut by its resolution results in an uncertainty between -10% and 15%.

Using the SaS photon pdfs instead of the GRV ones leads to a Monte Carlo correction factor of 1.201. This shows that, generally the dependence on the photon pdfs adds another systematic uncertainty of about 7%. This is not plotted and not

included in the numbers below.

The final ratio in the γ^*-proton c.m. frame including the statistical error and the evaluations of the uncorrelated systematic uncertainties is:

$$R^{DATA-HCM} = 1.81 \pm 0.06\ ^{+.26}_{-.19} \tag{7.15}$$

The correlated uncertainty of energy scale is for the ratio $^{+.0}_{-.15}$.

Chapter 8

Results / Discussion

In figure 8.1 are shown the measured dijet cross sections:

$$0.2 < y < 0.55$$

$$-3 < \eta^{*\,jet1,2} < 0$$

$$E_T^{*\,jet1} > 7.5 \text{ GeV}$$

$$E_T^{*\,jet2} > 6.5 \text{ GeV}$$

as a function of x_γ^{OBS} for five different regions of photon virtuality. The jets are found in the hadronic center of mass frame of the γ^*p system using the inclusive k_T - cluster algorithm.

The inner error bars are the statistical errors alone and the outer error bars are the statistical and uncorrelated systematic errors added in quadrature. The shaded band is the correlated systematic error coming from the energy scale uncertainty of the main calorimeter.

The shapes of the dijet cross sections change dramatically with increasing Q^2. This change is very visible in the transition region between the region $0.1 < Q^2 < 0.55$ GeV^2 and the DIS region. The cross section in the low x_γ^{OBS} region falls rapidly with Q^2.

The measured cross sections are compared to the predictions of the Herwig Monte Carlo at hadron level including both the LO direct and LO resolved components with the SaS1D photon pdfs. In the Q^2 range of these measurements, within the SaS description of the photon pdfs, it is mainly the perturbative (anomalous) resolved-photon component that contributes to the pdfs of the photon. In this picture, the resolved-photon component decreases as $\log(\mu^2/Q^2)$ as Q^2 increases. μ is the hard QCD scale of the process which, for jet production, is usually taken to be proportional to $(E_T^{jet})^2$. The logarithmic decrease of the photon pdfs essentially models higher-order terms in the perturbative expansion that are in principle calculable, but are not included in any of the available Monte Carlo programs simulating photoproduction processes. The measured cross sections are also compared to the predictions of Herwig using only the LO direct process. Here the dijet cross section

at low x_γ^{OBS} arises purely from parton-shower contributions to the LO direct process. In order to compare the shape of the measured cross sections with that of the Monte Carlo predictions, the latter have been normalized to the data cross section for $x_\gamma^{OBS} > 0.75$.

As seen in figure 8.1, the predictions of Herwig using the SaS1D pdfs describe well the shape of the measured cross sections in the DIS region. The LO resolved component is needed to describe the data up to $Q^2 = 49$ GeV^2. For higher photon virtualities, the Herwig predictions are mainly due to the direct component and describe well the measured cross sections. Hence, as predicted by pQCD, for $Q^2 > (E_T^{jet})^2$ only the direct component is needed to describe the data. In the lower Q^2 bin ($0.1 < Q^2 < 0.55$ GeV^2) the predictions fail to describe the shape of the measured cross sections.

The cross-section ratio $R^{DATA} = \sigma(x_\gamma^{OBS} < 0.75)/\sigma(x_\gamma^{OBS} > 0.75)$ as a function of Q^2 is shown in figure 8.2. The error bars and the systematic error representation are the same as in the cross sections plot. The cross section ratio falls steeply as a function of Q^2. The predictions of Herwig for the same ratio $R^{MC} = \sigma(x_\gamma^{OBS} < 0.75)/\sigma(x_\gamma^{OBS} > 0.75)$ for two different sets of photon pdfs as well as predictions of the Ariadne MC are also shown.

The prediction using the GRV set is flat, as expected for a photon pdf lacking a Q^2 dependence, while the prediction using the SaS1D prediction decreases with photon virtuality but lies below the data for the entire Q^2 region. As shown in the inset of figure 8.2, the double ratio R^{DATA}/R^{SaS} is independent of Q^2 and has a value of about 1.30. Therefore, the suppression of the virtual photon pdfs included in the SaS1D parametrization is in agreement with that observed in the data. However, the SaS1D model appears to underestimate the resolved component by $\sim 30\%$.

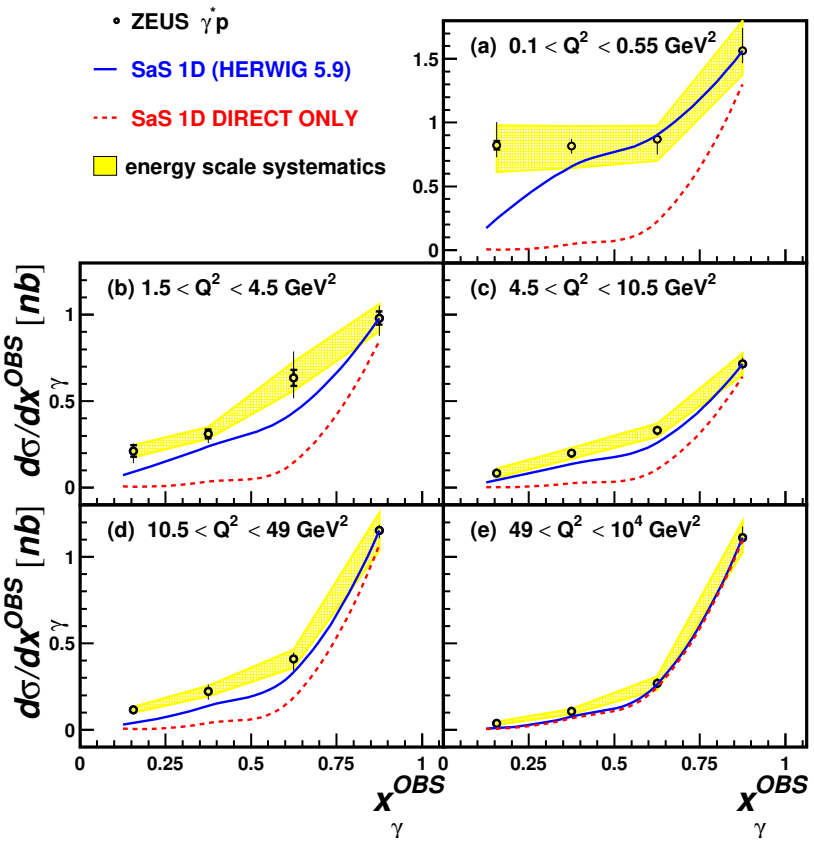

Figure 8.1 - Dijet cross section in the γ^*-proton hadronic c.m. frame for different regions of photon virtuality. The points are the data with the inner bars representing the statistical errors and the outer ones the statistical and the systematic errors added in quadrature. The shaded band shows the correlated systematic errors. The solid line is the hadron level prediction from Herwig using the SaS1D pdfs for the photon normalized to the highest x_γ^{OBS} bin in the data. The broken line is the prediction using the Herwig LO direct part only.

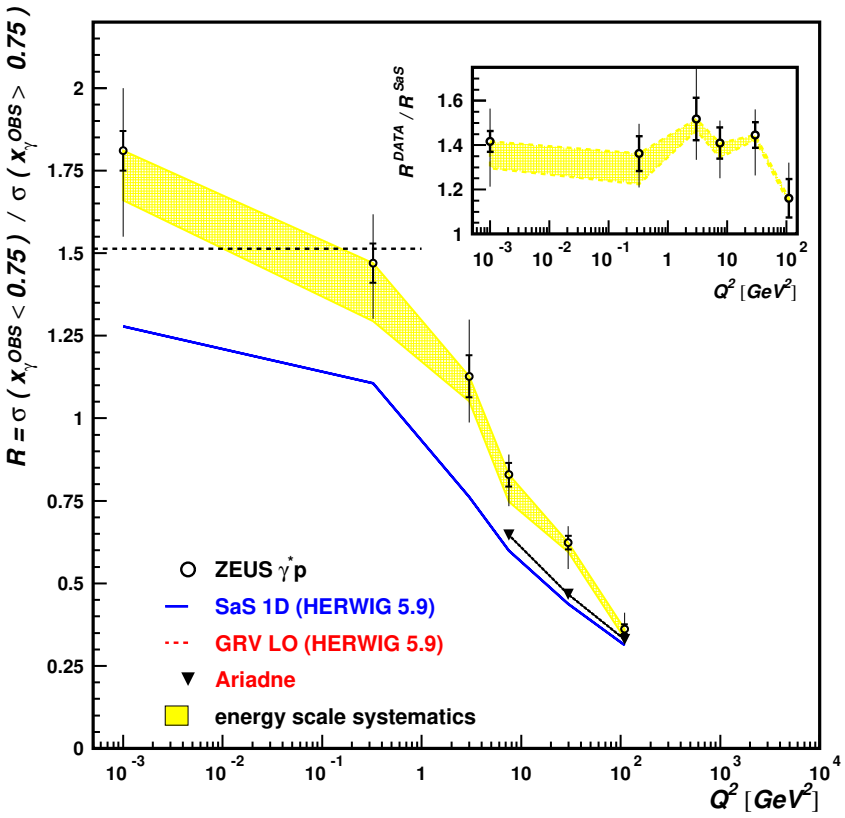

Figure 8.2 - Cross section ratio $R^{DATA} = \sigma(x_\gamma^{OBS} < 0.75)/\sigma(x_\gamma^{OBS} > 0.75)$ versus the photon virtuality. The points are the data with statistical errors represented from the inner error bars. The outer error bars represent the statistical and systematic errors added in quadrature. The solid line is the Herwig prediction using the SaS1D pdfs for the photon and the broken line is the prediction of Herwig using the GRV pdfs for the photon, while the inverted triangles connected by the dot-line show the prediction of Ariadne for the ratio. The data fall with increasing photon virtuality. The SaS1D prediction falls as well. The GRV prediction is flat as expected since it models real photons and lacks a photon suppresion with photon virtuality. The ratio of the data measurement with the SaS1D prediction is shown as an inset. This ratio R^{DATA}/R^{SaS} seems to be flat in Q^2. The SaS1D model appears to underestimate the resolved component by $\sim 30\%$.

Chapter 9

Conclusions

Dijet cross sections, $\frac{d\sigma}{dx_\gamma^{OBS}}$, have been measured using the longitudinally invariant k_T jet algorithm in the γ^*-proton center of mass reference frame for $10^{-1} < Q^2 < 10^4$ GeV^2. and $0.4 < y < 0.55$. The measured cross section are for jets with $-3 < \eta^{*\,jet1,2} < 0$ and $E_T^{*\,jet1} > 7.5$ GeV, $E_T^{*\,jet2} > 6.5$ GeV. The x_γ^{OBS} dependence of the measured dijet cross sections changes with increasing Q^2. The low x_γ^{OBS} cross section decreases rapidly as the photon virtuality increases.

The predictions of the Herwig Monte Carlo using the SaS1D photon pdfs describe the dijet cross section well in the region $1.5 < Q^2 < 10^4$ but fail to describe the data in the region $0.1 < Q^2 < 0.55$ GeV^2. The LO resolved-photon component is needed to describe the data up to $Q^2 = 49$ GeV^2, when the photon is probed at the scale $\mu^2 \sim 49$ GeV^2, which is comparable to the hard scattering scale, $(E_T^{jet})^2$ of these measurements.

The ratio $\sigma(x_\gamma^{OBS} < 0.75)/\sigma(x_\gamma^{OBS} > 0.75)$ for dijet cross sections decreases as Q^2 increases. However, the measured ratio lies about 30% above the predictions of Herwig using the SaS1D photon pdfs. The rate of suppresion of the $x_\gamma^{OBS} < 0.75$ region observed in the data is in agreement with the predictions of Herwig using the SaS1D photon pdfs. Hence the data may be interpreted in terms of a resolved photon component which is suppressed as the photon virtuality increases.

Chapter 10

Acknowledgments

I am deeply grateful to professor R.Klanner and E.Lohrmann for their continuous support and for giving me the opportunity to join the ZEUS experiment and to study interesting physics topics.

I express my special thanks to Costas Foudas for his guidance and organisation of the analysis.

I sincerely thank all of them for their valuable advice and suggestions, and reading and commenting on this manuscript.

Many thanks go to all the students of Hamburg University at DESY and to Monica Vazquez, Anna Lupi, Neil Macdonald, Sean Mattingly.

I want to acknowledge the financial support given to me by the DAAD[1] during my work at ZEUS / DESY between October 1997 and September 2000.

[1] DAAD - Deutscher Akademischer Austauschdienst - www.daad.de .

Appendix A

Jet Energy Correction

Jets measured in the calorimeter have different transverse energies from jets at the hadron level. There are two effects to be distinguished here. One is the smearing of the energy distribution because of detector resolution. The other effect is a shift between the jet transverse energy measured in the calorimeter and the jet transverse energy at the hadron level. The jets measured in the calorimeter have a smaller transverse energy $E_T^{jet-cal}$ than the "true" value $E_T^{jet-had}$ of the hadron jets. This is due to dead material in front of the calorimeter and particles which do not deposit energy in the main calorimeter such as muons and neutrinos. Differences are also seen for the pseudorapidity η^{jet} and the azimuthal angle ϕ^{jet} but there is no systematic bias here.

The transverse jet energy needs therefore to be corrected. By correcting the systematic shift an improvement of the purities and efficiencies is achieved. Another way of doing this would be to use different cuts on the jets at the hadron and calorimeter level. But that is not as elegant as this method and increases the probability of making errors. The Herwig5.9 Monte Carlo was used for calculating the correction factors. The cuts used on the jets are loser than the actual cuts used in the analysis:

$$E_T^{jet-cal} \geq 4.\text{GeV} \quad ; \quad -2. \leq \eta^{jet-cal} \leq 3. \tag{A.1}$$

A matching of the hadron and calorimeter jets was done. I.e. for each hadron jet the distance in the $\eta - \phi$ plane between that jet and each calorimeter jet is computed as:

$$d(had - cal) = \sqrt{(\eta^{jet-had} - \eta^{jet-cal})^2 + (\phi^{jet-had} - \phi^{jet-cal})^2} \quad . \tag{A.2}$$

The pairs with the minimum $d(had - cal)$ are taken, provided this distance itself is smaller than 1 unit. The jet variables for this hadron-calorimeter pair of jets are then considered in the calculations.

In figure A.1 resolution plots for the transverse energy, the pseudorapidity, and the azimuthal angle of the jets are shown. As can be seen from those plots, the resolution for the E_T^{jet} is about 17% and the systematic shift 12%. For the η^{jet} and ϕ^{jet} there is no systematic shift. The resolution for η^{jet} is about 0.07 units and for ϕ^{jet} 0.08 units (radians?).

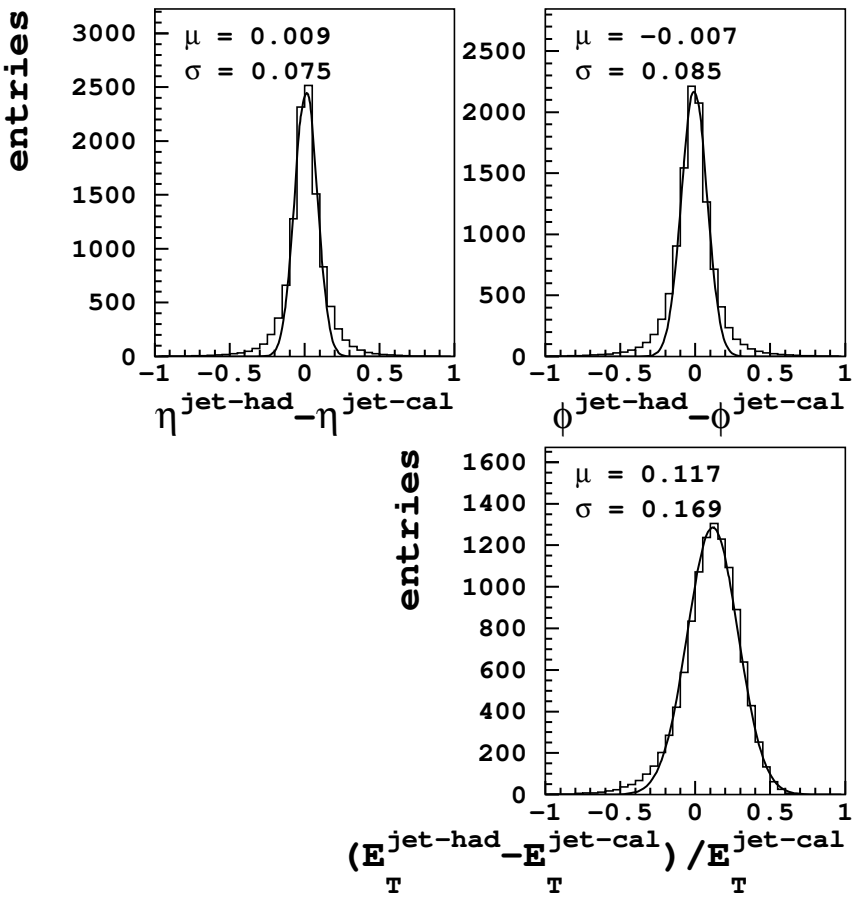

Figure A.1 - Resolution plots in the laboratory frame: $\eta^{jet-had} - \eta^{jet-cal}$, $\phi^{jet-had} - \phi^{jet-cal}$, and $(E_T^{jet-had} - E_T^{jet-cal})/E_T^{jet-cal}$. No systematic shift is observed for the pseudorapidity and the azimuthal angle. A shift of about 20% is observed for the transverse energy of the jets.

A correction factor is needed such that:

$$E_T^{jet-corrected} = C(E_T^{jet-cal}, \eta^{jet-cal}) \cdot E_T^{jet-cal} \quad . \tag{A.3}$$

In the figure A.2 the quantity $E_T^{jet-had}/E_T^{jet-cal}$ is shown for 5 different bins in $\eta^{jet-cal}$. In each bin of the jet transverse energy $E_T^{jet-cal}$ the mean value for this ratio has been calculated. As expected the measured energy approaches that of the hadron energy

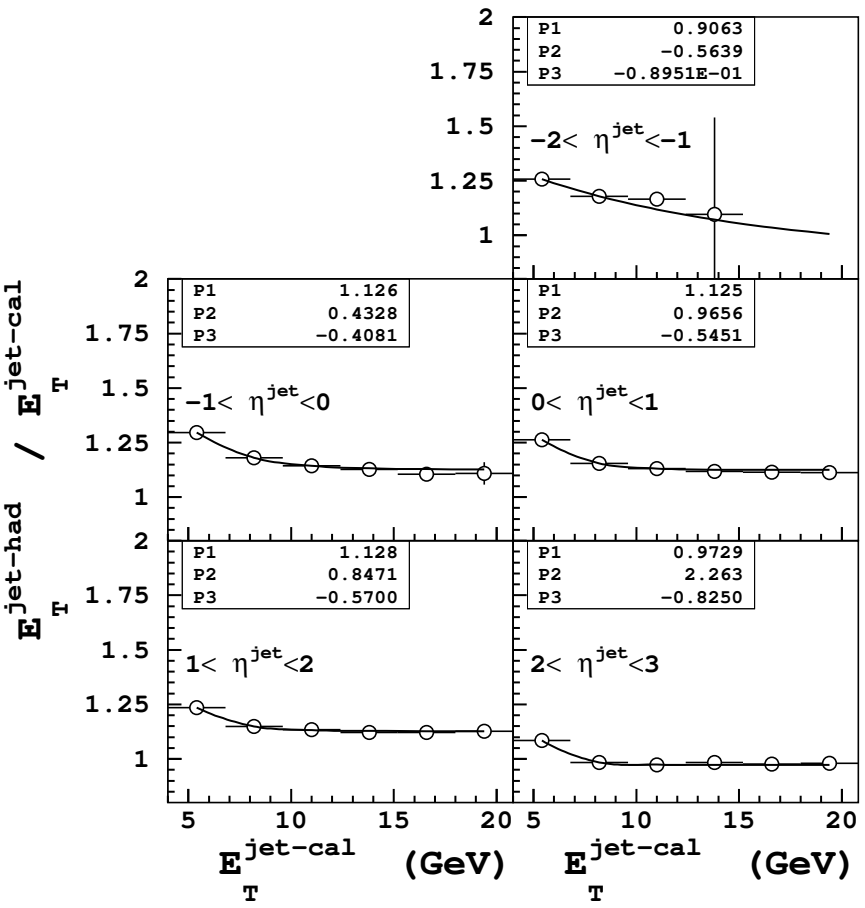

Figure A.2 - Jet corrections in the laboratory frame. $E_T^{jet-had}/E_T^{jet-cal}$ vs. $E_T^{jet-cal}$ in different η^{jet} bins. Also the fit with the function $P1 + \exp(P2 + P3 * E_T^{jet-cal})$ and the values of the parameters are shown.

as the E_T^{jet} increases. The correction factor was determined by a parametrization of this ratio using a fit of the form:

$$C(E_T^{jet-cal}, \eta^{jet-cal}) = P1 + \exp(P2 + P3 * E_T^{jet-cal}) \quad , \tag{A.4}$$

where the parameters $P1, P2, P3$ do not depend on $E_T^{jet-cal}$ but on $\eta^{jet-cal}$ (they change in different $\eta^{jet-cal}$ bins). As can be seen the least squares fit with the above function describes the required corrections reasonably well. The fact that the parameters depend on the $\eta^{jet-cal}$ has to do with the fact that the distribution of the dead material is dependent on the pseudorapidity η (or better, on the polar angle θ). This dependence of the correction factors on $\eta^{jet-cal}$ is seen also in figure A.3. There the ratio $E_T^{jet-had}/E_T^{jet-cal}$ is plotted versus $\phi^{jet-cal}$ (plot above) and $\eta^{jet-cal}$ (plot below). The two peaks (at $-1.$ and $1.$) in the plot versus $\eta^{jet-cal}$ are understood in terms of the increase of the dead material in front of the calorimeter in those two regions. The ratio versus the azimuthal angle $\phi^{jet-cal}$ is pretty much constant. Therefore, the above parametrization was only done in different bins of $\eta^{jet-cal}$ but not in different bins of $\phi^{jet-cal}$.

After applying the above correction to the jet transverse energy, no systematic shift is observed anymore between $E_T^{jet-had}$ and $E_T^{jet-cal}$. This can be seen in figure A.4

In a complete analogous way the corrections are calculated in the hadronic center-of-mass frame. tha ratio $E_T^{jet-had}/E_T^{jet-cal}$ vs. $E_T^{jet-cal}$ and the parametrized fit are shown in figure A.5 together with the fit parameters.

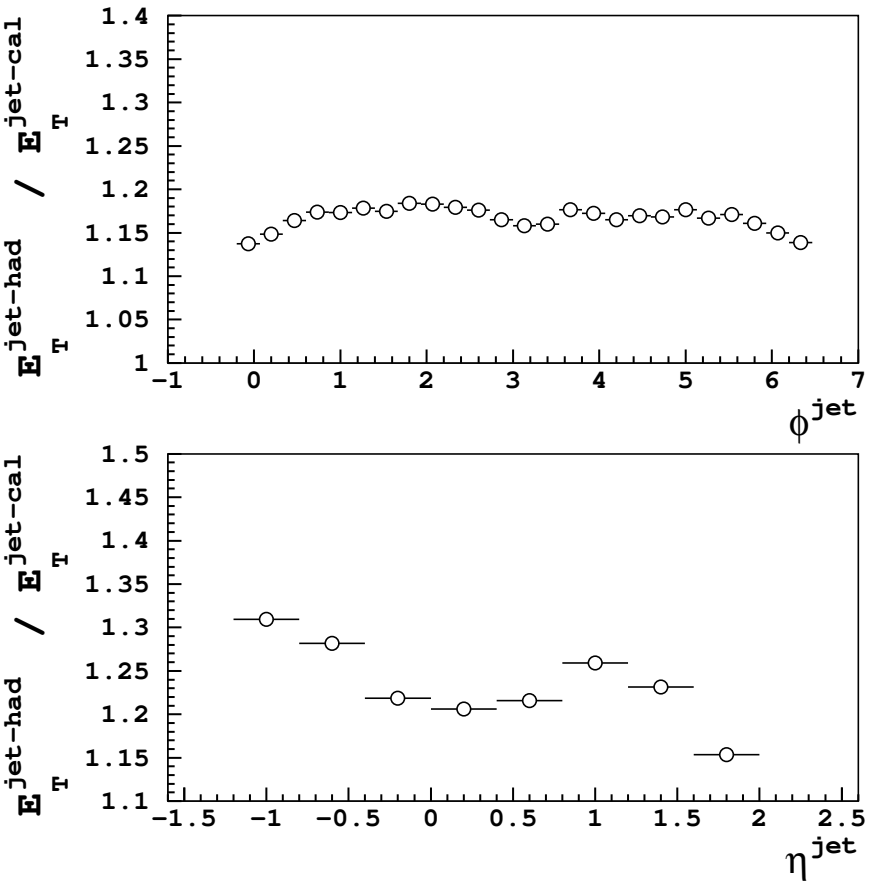

Figure A.3 - Jet corrections in the laboratory frame. $E_T^{jet-had}/E_T^{jet-cal}$ vs. $\phi^{jet-cal}$ (plot above) and $\eta^{jet-cal}$ (plot below) is shown. The correction is flat in $\phi^{jet-cal}$ as expected and shows a characteristic shape in $\eta^{jet-cal}$. This has to do with the distribution of the dead material in the detector as a function of the pseudorapidity (radial angle).

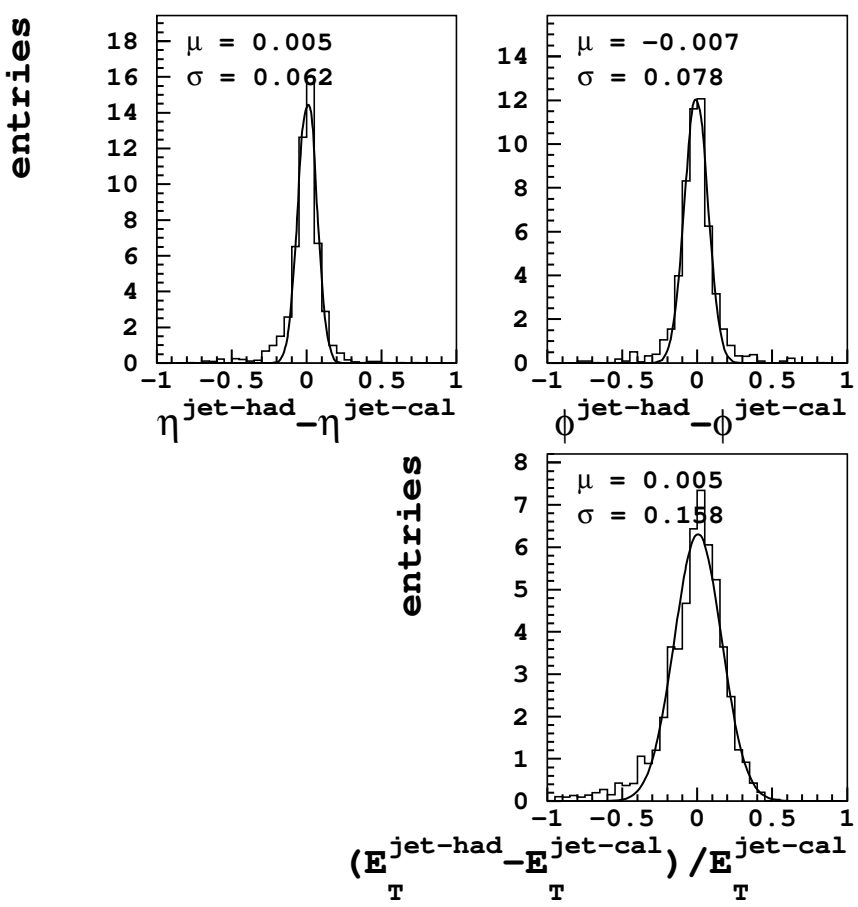

Figure A.4 - Resolution plots in the laboratory frame after applying the jet energy correction: $(E_T^{jet-had} - E_T^{jet-cal})/E_T^{jet-cal}$ For this plot, the analysis cuts are applied on the jets: $E_T^{jet1,2-had} \geq 7.5, 6.5$ GeV $-1. \leq \eta^{jet1,2-had} \leq 2.$ and same cuts on the calorimeter jets (here the corrections are applied on the calorimeter jet energy).

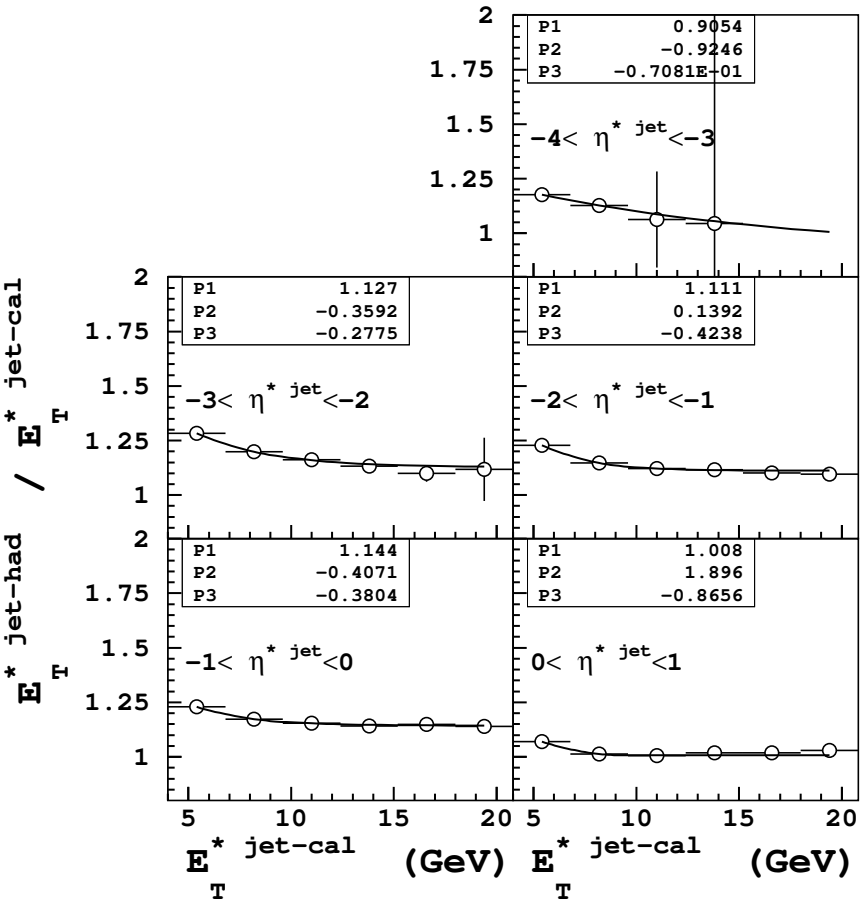

Figure A.5 - Jet corrections in the hadronic c.m. frame. $E_T^{*jet-had}/E_T^{*jet-cal}$ vs. $E_T^{*jet-cal}$ in different η^{*jet} bins. Also the fit with the function $P1 + \exp(P2 + P3 * E_T^{*jet-cal})$ and the values of the parameters are shown.

Appendix B

Triple Differential Cross Sections

In order to study the two scale problem for virtual photons, the dijet cross section is measured as a function of the photon virtuality Q^2 and the hard scale of the jets, that is evaluated by the mean of the transverse energy of the two leading jets:

$$\overline{E}_T = \frac{E_T^{jet,1} + E_T^{jet,2}}{2} \tag{B.1}$$

Dijet events are selected in the $\gamma^* p$ frame with $E_T^{jet,1} > 7.5$ GeV, $E_T^{jet,2} > 6.5$ GeV and $-3 < \eta^{jet} < 0$. The cross sections are measured in the phase space defined by $0.2 < y < 0.55$ and $0.1 < Q^2 < 0.55$, $1.5 < Q^2 < 4.5$, $4.5 < Q^2 < 10.5$, $10.5 < Q^2 < 49.0$ and $49.0 < Q^2 < 10^4$ GeV^2.

The measured triple differential dijet cross sections $d^3\sigma/(dx_\gamma^{OBS} dQ^2 d\overline{E}_T^2)$ are shown as a function of x_γ^{OBS} in figure B.1 in the different regions of Q^2 and $\overline{E}_T^2$. The points are the ZEUS data with the statistical (inner error bars) and systematic errors added in quadrature to them (outer error bars). The uncorrelated systematic coming from the uncertainty in the energy of the jets is shown as a band. The LO Herwig predictions using the SaS1D parametrization for the photon PDFs are also shown as a solid line. The LO-direct part only of the Herwig predictions is shown in B.1 as a dashed line. The Herwig predictions do not describe the absolute cross section of the data and are therefore normalized to the highest x_γ^{OBS} bin ($x_\gamma^{OBS} > 0.75$) in order to compare the shape of the data with that of the MC predictions.

For each $\overline{E}_T^2$ bin, the cross section in the low x_γ^{OBS} region falls faster with increasing Q^2 than the cross section in the high x_γ^{OBS} region. For the bins with $Q^2 > \overline{E}_T^2$ the data are well described by the Herwig predictions including only the LO-direct component. In the bins with $Q^2 < \overline{E}_T^2$ the LO-direct component is not enough to describe the data.

In the figure B.2 the measured cross sections are compared to Herwig using the two LO-resolved photon components of SaS1D. Both simulations are drawn as dotted lines and the upper one is the Herwig using the perturbative (anomalous) LO resolved component, while the lower one the Herwig using the non-perturbative (VDM) LO resolved component. From the simulation is seen that both resolved components are suppressed as the photon virtuality increases and that, within the SaS1D model, in the region of phase space that is being looked at most of the resolved component

is perturbative (anomalous).

In B.3 a comparison of the cross sections with the Lepto MC is shown. Lepto acts very similarly to the Herwig with the direct-only component in B.1. For $Q^2 > \overline{E}_T^2$ Lepto describes the data. Lepto is a DIS Monte Carlo and this region is indeed the one where Lepto is expected to be valid.

The ratio of cross sections $R = \sigma(x_\gamma^{OBS} < 0.75)/\sigma(x_\gamma^{OBS} > 0.75)$ as a function of Q^2 and for three ranges in $\overline{E}_T^2$ is shown in figure B.4. The ratio of the data falls with increasing Q^2 for each range of $\overline{E}_T^2$. These results show the suppression of the virtual photon structure with increasing photon virtuality. The Herwig prediction using SaS1D also falls with increasing Q^2 but underestimates the measured ratio.

B.1 Conclusions

The structure of virtual photons has been studied at HERA using dijet production. The use of the data from the virtual photon measurements will improve our understanding of the photon PDFs. More thorough studies can be done using the new measurements in this challenging phase space region.

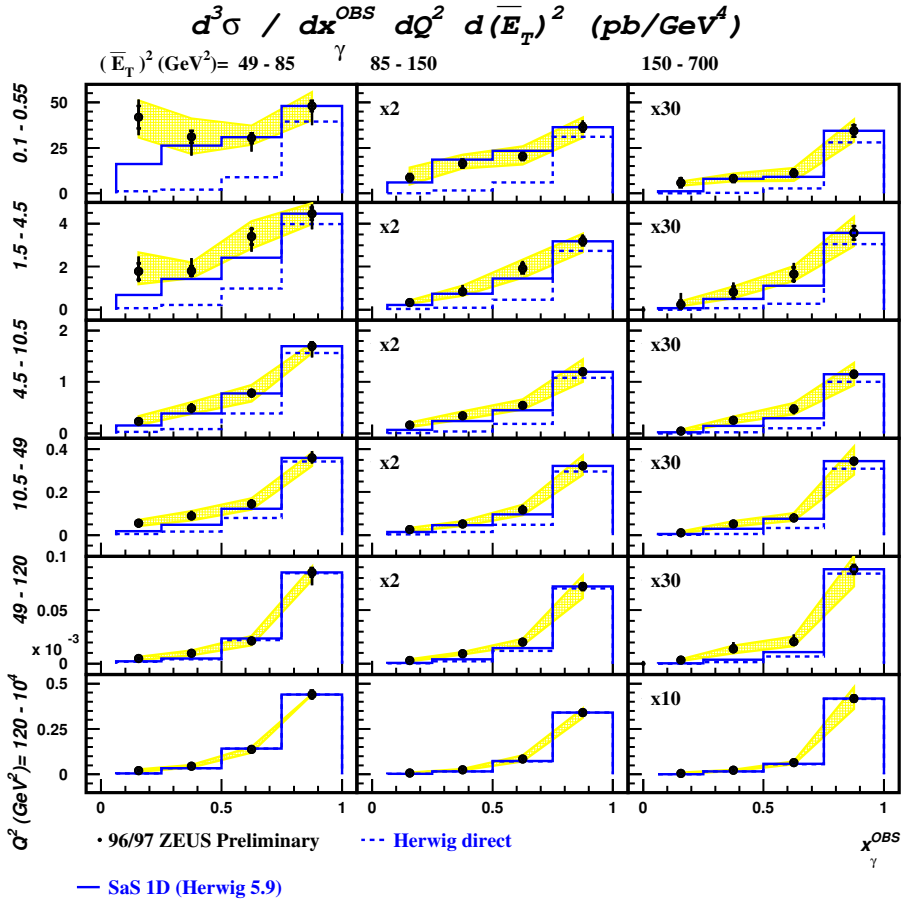

Figure B.1 - Triple differential cross section $d^3\sigma/(dx_\gamma^{OBS} dQ^2 d\overline{E}_T^2)$ as a function of x_γ^{OBS} for different regions in Q^2 and $\overline{E}_T^2$. The points represent the measured cross sections with statistical errors (inner error bars) and uncorrelated systematic errors added in quadrature to them (outer error bars). The shaded bands display the uncertainty in the plotted quantities due to that in the jet energy scale. The solid line is the Herwig MC using the SaS1D parametrization for the photon PDFs and the dashed line is the LO-direct part only from Herwig.

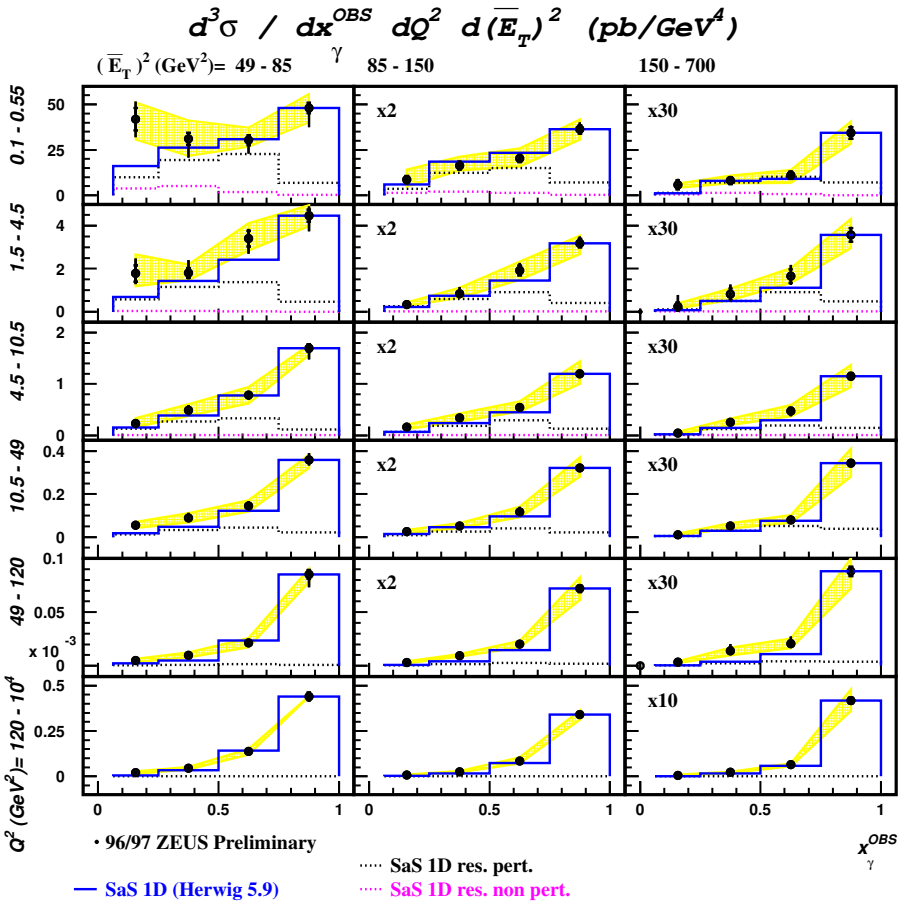

Figure B.2 - Comparison of the measured cross sections with the Herwig MC using the two resolved components from SaS1D: the perturbative (anomalous) component (upper dotted curve) and the non-perturbative (VDM) component (lower dotted curve). Herwig using the SaS1D total is also shown as a solid line.

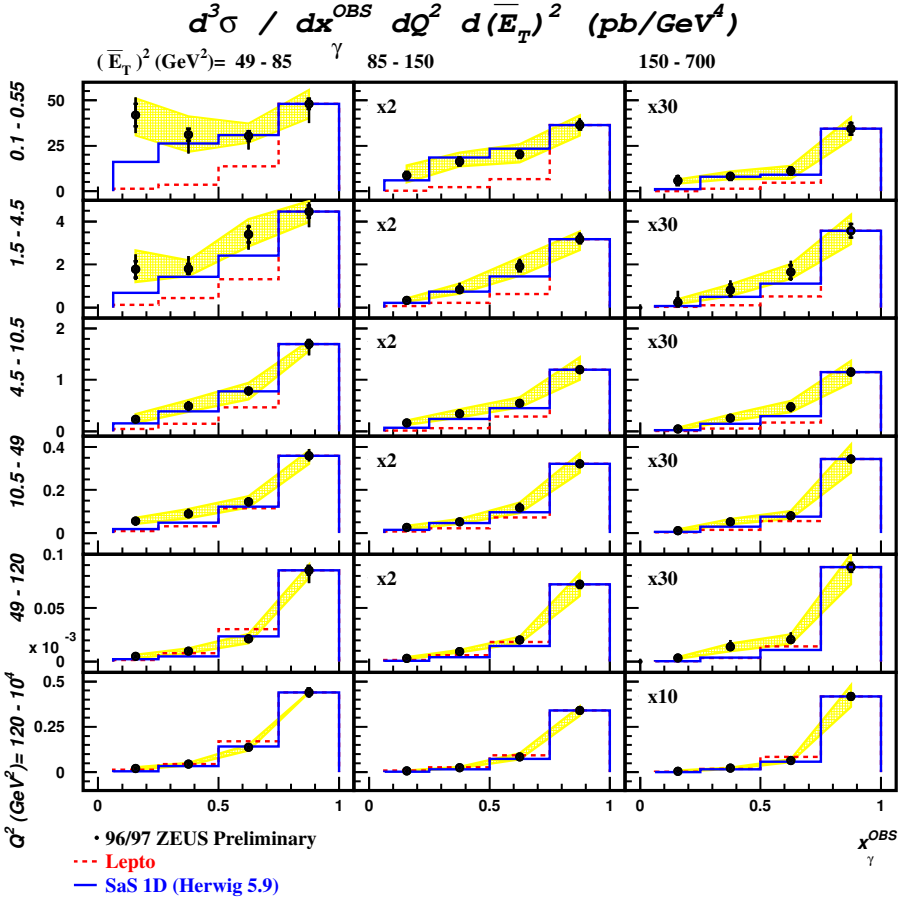

Figure B.3 - Comparison of the measured cross sections with the Lepto MC (dashed line). Herwig using the SaS1D total is also shown as a solid line. Lepto is seen to act very similarly the Herwig using the LO-direct component only.

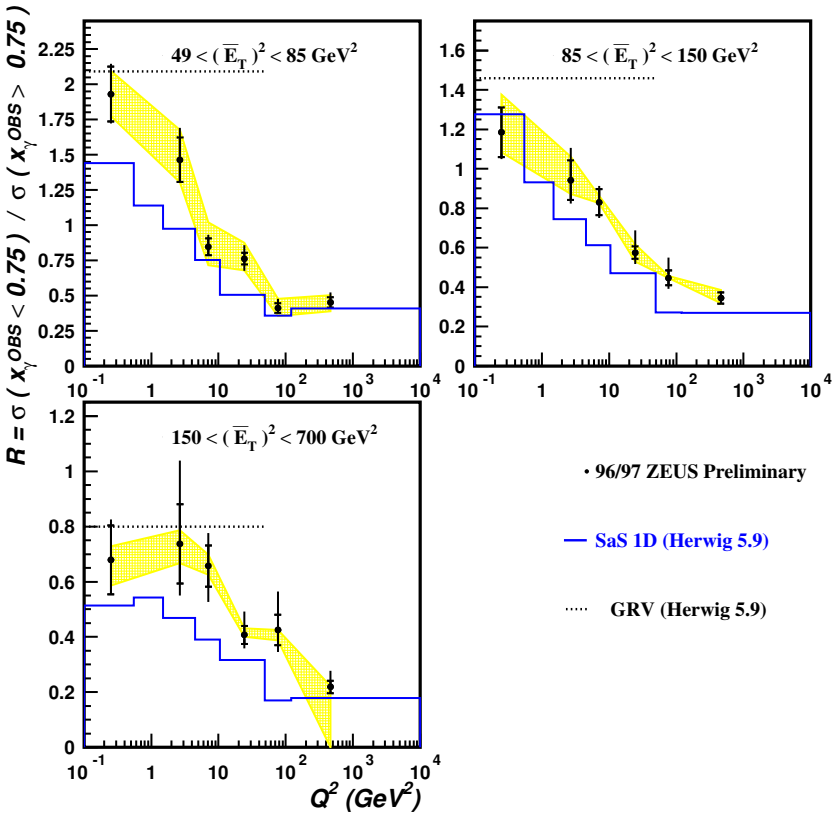

Figure B.4 - The ratio of cross sections $R = \sigma(x_\gamma^{OBS} < 0.75)/\sigma(x_\gamma^{OBS} > 0.75)$ as a function of Q^2 for different ranges in $\bar{E}_T^2$. The solid line is the Herwig MC using the SaS1D parametrization for the photon PDFs and the dotted horizontal line is the Herwig prediction using the GRV parametrization for the real photon PDFs.

Bibliography

[Ab92] F. Abe. *Phys. Rev.* **D45** 1448 (1992).

[Ab95] H. Abramowitz, A. Caldwell and R. Sinkus. *Neural Network based electron identification in the ZEUS Calorimeter* DESY 95-054 (1995).
R. Sinkus. *Nucl. Instrum. Methods* **A361** 290 (1995).

[Ab98] H. Abramowitz and A. Caldwell. *HERA Collider Physics DESY 98-192* (1998).

[Al77] G. Altarelli and G. Parisi. *Nucl. Phys.* **B126** 298 (1977).
V.N. Gribov and L.N. Lipatov. *Sov. J. Nucl Phys.* **15** 438 (1972).
L.N. Lipatov. *Sov. J. Nucl. Phys.* **20** 96 (1975).
Y.L. Dokshitzer. *Sov. Phys. JETP.* **46** 641 (1977).

[An92] J. Andruskow et al. *DESY 92-066* (1992).
K. Piotrzkowski. *DESY F35D-93-06* (1993).

[Ar95] N. Arteaga et al., *Phys. Rev.* **D52** 4920 (1995).

[Au94] P. Aurenche, M. Fontannaz and J.P. Guillet. *Z. Phys.* **C64** 621 (1994).

[Ba95] A. Bamberger et al. *ZEUS-Note 95-095* (1995).

[Ba97] A. Bamberger et al. *Nucl. Instr. and Methods* **A 401** 63-80 (1997).

[Ba96] R.M. Barnett et al. *Phys. Rev. / Particle Data Group* **D54** 1 (1996).

[Ba95] L.A.T. Bauerdick et al. *DESY-95-236* (1995).

[Be34] H. Bethe and W. Heitler. *Proc. Roy. Soc.* **A146** 83 (1934).

[Bl69] E.D. Bloom et al. *Phys. Rev. Lett.* **23** 930 (1969). W. Pankofski. *Proceedings of the International Conference in High Energy Physics* Vienne / Austria (1968).

[Bo99] I. Bohnet. *'Investigations on Uniformity, Radiation Resistance and Calibration of ZEUS Calorimeter Components at HERA'* PhD Thesis - University of Hamburg (1999).

[Bo96] I. Bohnet and B. Surrow. *'Studies on radiation damage effects in the Beam Pipe Calorimeter at ZEUS in 1995'* ZEUS-Note 98-026 (1998).

[Br87] R. Brun et al. *Geant3.13* CERN DD/EE/84-1 (1987).

[Br89] R. Brun et al. *GEANT3, CERN DD/EE/81-1* (1989).

[Bu95] J.M. Butterworth. *Photon Structure as Seen at HERA.* (1995). DESY 95-043.

[Bu96] J.M. Butterworth, J.R. Forshaw and M.H. Seymour. *Z. Phys.* C72 637-646 (1996).
J.M. Butterworth et al. *Multiple Hard Parton Interactions at HERA* hep-ph/9601322 (1996).

[Ca69] C.G. Callan and D. Gross. *Phys. Rev. Lett.* **22** 156 (1969).

[Ca93] A. Caldwell et al. *Nucl. Instr. and Meth.* **A321** 356 (1992).

[Ca95] A.C. Caldwell. *The Structure of the Photon and the Proton.* (1995). DESY 95-231.

[Ca00] T. Carli et al. *HZtool - A Package for Monte Carlo Generator - Data Comparisons at HERA* `http://www.desy.de/ h01rtc/hztool.html` (2000).

[Ct93] S. Catani et al. *Nucl. Phys.* **B406** 187 (1993).
S.D. Ellis and D.E. Soper. *Phys. Rev.* **D48** 3160 (1993).

[Co85] J.C.D. Collins, D.E. Soper and G. Sterman. *Nucl. Phys. B* **261** 104 (1985).

[Co00] G. Corcella, I.G. Knowles, G. Marchesini, S. Moretti, K. Odagiri, P. Richardson, M.H. Seymour and B.R. Webber. *HERWIG6.2* hep-ph/0011363 (2000).

[De91] M. Derrick et al. *Nucl. Instr. and Meth.* **A309** 77 (1991).
A. Andresen et al. *Nucl. Instr. and Meth.* **A309** 101 (1991).
B. Bernstein et al. *Nucl. Instr. and Meth.* **A336** 23 (1993).

[DE94] DESY. *Annual report* (1994).

[El92] S.D. Ellis, Z. Kunszt and D.E. Soper, *Phys. Rev. Lett.* **69** 3615 (1992).

[Fe69] R.P. Feynman. *Phys. Rev. Lett.* **23** 1415 (1969).

[Fi93] S.M. Frixione, M.L. Mangano, P. Nason and G. Rindolfi. *Phys. Lett.* **B319** 339 (1993).
Glück, E. Reya and M. Stratmann. *Phys. Rev.* **D54** 5515 (1996).
M. Klasen, G. Kramer and B. Potter. *Eur. Phys. J.* **C1** 261 (1998).

[Fo93] B. Foster et al. *Nucl. Instr. and Meth.* **A338** 254 (1993).

[Gl61] S.L. Glashow. *Nucl. Phys.* **22** 579 (1961).
A. Salam. *"Weak and Electromagnetic Interactions" - Proceedings of The Nobel Symposium / Lerum, Sweden* (1968).
S. Weinberg. *Phys. Rev. Lett.* **19** 1264 (1967).

[Gl92] M. Glück, E. Reya and A. Vogt. *Phys. Rev.* **D46** 1973 (1992).

[Ge64] M. Gell-Mann. *Phys. Lett.* **8** 214 (1964).
G. Zweig. *CERN-8192/TH 401* (1964).
G. Zweig. *CERN-8419/TH 402* (1964).

[Go92] L.E. Gordon and J.K. Storrow. *Nucl. Phys* **B489** 405 (1997).

[Gr89] M.G. Green. *RNBNC 89-01* (1989).

[Gr00] D.E. Groom et al., *The European Physical Journal* **C15** 1 (2000).

[H1r] H1 Collaboration, *Phys.Lett.* **B483** 36-48 (2000)

[H1v] H1 Collaboration, *Eur.Phys.J.* **C13** 397-414 (2000)

[Ha64] R. Hagedorn *Relativistic Kinematics* (W.A.Benjamin Inc. 1964).

[Ha84] F. Halzen and A.D. Martin. *Quarks and Leptons*.
(John Wiley Sons Inc., New York, 1984).

[HB94] HERA-B Collaboration. *Technical Design Report* DESY-PRC 95/01 (1995).

[HE93] HERMES Collaboration. *Technical Design Report* (1993).

[Ho53] R. Hofstadter et al. *Phys. Rev.* **91** 422 (1953).
R. Hofstadter and R.W. McAllister . *Phys. Rev.* **98** 217 (1955).
R. Hofstadter. *Ann. Rev. Nucl. Part. Sci.* **7** 458 (1957).

[Kr00] M.Krawczyk et al., *Survey of present data on photon structure functions and resolved photon processes*, hep-ph/0011083

[Ku76] E.A. Kuraev, L.N. Lipatov and V.S. Fadin. *Sov. Phys. JETP* **44** 443 (1976).
E.A. Kuraev, L.N. Lipatov and V.S. Fadin. *Sov. Phys. JETP* **45** 199 (1977).
Y.Y. Balitzki and L.N. Lipatov. *Sov. J. Nucl. Phys.* **28** 822 (1978).

[LE00] The LEP Higgs Working Group. *A Hint of the Standard Model Higgs Boson at LEP* (2000).

[Lo92] E. Lohrmann. *Hochenergiephysik* (1992).

[Ma92] G. Marchesini, B.R. Webber, G. Abbiendi, I.G. Knowles, M.H. Seymour and L. Stanco. *Computer Phys. Commun.* **67** 465 (1992).

[Me94] Metallwerk Plansee GmbH, *Technical information* Lechbruck, Austria (1994).

[Ne99] Neil S. Macdonald. *Structure of the Virtual Photon at HERA*. PhD Thesis - University of Glasgow (1999).

[Ma94] A. Martin et al. *Phys. Rev.* **D50** 6734 (1994).

[Se99] Sean E. K. Mattingly. *Virtual Photon Structure with ZEUS at HERA*. PhD Thesis - University of Wisconsin (1999).

[Mo98] T. Monteiro. *'Study of Exclusive Electroproduction of Mesons at Low Q^2 Using the ZEUS Beam Pipe Calorimeter at HERA'* PhD Thesis - University of Hamburg - DESY-THESIS-1998-027 (1998).

[Ne00] Neutrino 2000. *XIX International Conference on Neutrino Physics and Astrophysics - Sudbury/Canada June 16-21* (2000).
`http://nu2000.sno.laurentian.ca`

[Ni00] R.Nisius. *Nucl. Phys. B* **82** 3-13 (2000).

[PL84] PLUTO Collaboration, C. Berger et al. *Phys. Lett.* **B124** 119 (1984).

[Pö99] B. Pötter. *JetVip 2.1* hep-ph/9911221.
S. Frixione, G. Ridolfi. *Nucl. Phys.* **B507** 315 (1997).
M.Klasen, G. Kramer. *Phys. Lett.* **B366** 385 (1996).

[Re96] J. Repond. *Jet Energy Corrections* ZEUS-Note 96-133 (1996).
A. Caldwell, W. Liu, B. Straub. *BCAL Electron Studies Part I: MC and Test Beam Energy Studies* ZEUS 98-002 (1998).
A. Caldwell, W. Liu, B. Straub. *BCAL Electron Studies Part II: Energy Scale Calibration* ZEUS-Note 98-018 (1998).

[Sa69] J.J. Sakurai. *Phys. Rev. Lett.* **22** 981 (1969).

[Sa98] A. Savin. *Study of Calorimeter Noise in the 1996 Data ZEUS-Note 98-07* (1998).

[Sc93] G.A. Schuler and T. Sjöstrand. *Nucl. Phys.* **B407** *CERN TH 6976-93* 539 (1993).

[Se95] M.H.Seymour. *Jets in QCD* hep-ph/9506421, CERN-TH/95-176 (1995).

[Sj94] T. Sjöstrand. *Computer Phys. Commun.* **82** 74 (1994).

[Sj95] T. Sjöstrand and G.A. Schuler. *Z. Phys.* **C68** 607 (1995).
G.A. Schuler. Proceedings of Photon '95. (1995). World Scientific, Singapore (1995).

[Sj00] T. Sjöstrand et al. *High-Energy-Physics Event Generation with Pythia6.1* hep-ph/0010017 (2000).

[Su98] B. Surrow. *'Measurement of the Proton Structure Function F_2 at Low Q^2 and Very Low x with the ZEUS Beam Pipe Calorimeter at HERA'* PhD Thesis - University of Hamburg - DESY-THESIS-1998-004 (1998).

[Ui92] H. Uijterwaal. *'The Global Second Level Trigger for ZEUS'* PhD Thesis - University of Amsterdam (1992).

[Vo97] A. Vogt. The parton structure of real photons. *Photon 97* (1997). hep-ph/9709345.
T. Sjöstrand, J.K. Storrow and A. Vogt. Parton distribution functions of real and virtual photons - hep-ph/9601351 (1996).

[We34] C.F. von Weizsäcker. *Z. Phys.*, **88** 612 (1934).
E.J. Williams. Phys. Rev. **45** 729 (1934).
S. Frixione, M.L. Mangano, P. Nason, G. Rindolfi. *Phys. Lett.* **B319** (1993).

[Wi77] E. Witten, *Nucl. Phys.* **B120** 189 (1977).
W.A. Bardeen, A.J. Buras, *Phys. Rev.* **D20** 166 (1979).
W.A. Bardeen, A.J. Buras, *Phys. Rev.* **D21** 2041 (1980).

[ZE93] ZEUS Collaboration, *The ZEUS Detector* Status Report (1993).

[ZEr] ZEUS Collaboration, *The structure of the photon and the dynamics of resolved photon processes in dijet photoproduction at HERA* (2000).

[ZEv] ZEUS Collaboration, *The* Q^2 *Dependence of Dijet Cross Sections in* $\gamma\mathrm{p}$ *Interactions at HERA* hep-ex/0002010 (2000).